

AD-A074 908

WASHINGTON UNIV SEATTLE DEPT OF ATMOSPHERIC SCIENCES
THE OPTICAL PROPERTIES OF YOUNG SEA ICE (U)

F/G 8/12

UNCLASSIFIED

AUG 79 D K PEROVICH
SCIENTIFIC-17

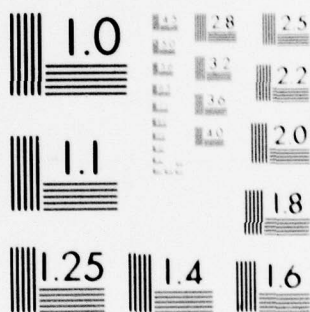
N00014-76-C-0234

NL

1 OF 2

AD
A074908





MICROCOPY RESOLUTION TEST CHART
NATIONAL BUREAU OF STANDARDS-1963-A

AD A074908

LEVEL

(12)

DEPARTMENT OF
ATMOSPHERIC SCIENCES
UNIVERSITY OF WASHINGTON

DDC
RECEIVED
OCT 10 1979
REGULATED
E

SCIENTIFIC REPORT NO. 17
OFFICE OF NAVAL RESEARCH
CONTRACT N00014-76-C-0234
NR 307-252

See 1473 in back.

THE OPTICAL PROPERTIES OF YOUNG SEA ICE

BY

DONALD KOLE PEROVICH

This document has been approved
for public release and sale; its
distribution is unlimited.

DISTRIBUTION UNLIMITED

AUGUST 1979

79 10 09 099

DDC FILE COPY

12

THE OPTICAL PROPERTIES OF YOUNG SEA ICE

BY

DONALD KOLE PEROVICH
GEOPHYSICS PROGRAM
UNIVERSITY OF WASHINGTON
SEATTLE, WASHINGTON 98195

REPRODUCTION IN WHOLE OR IN PART
IS PERMITTED FOR ANY PURPOSE OF THE
UNITED STATES GOVERNMENT

DISTRIBUTION UNLIMITED

University of Washington

Abstract

THE OPTICAL PROPERTIES OF YOUNG SEA ICE

By Donald Kole Perovich

Eight laboratory experiments were performed to determine the optical properties of young salt ice and to examine correlations between the optical properties and the state of the ice. Ice grown at different temperatures (-10 , -20 , -30 , and -37°C) and from water of different salinities (0 , 16 , and 31 ‰) was investigated. The experiments were conducted using a tank system which was designed to grow ice similar to that found in nature, allow an accurate determination of the state and structure of the ice, and permit in situ optical measurements to be made. Measurements of incident, reflected, and transmitted irradiances were used in conjunction with a modified Dunkle and Bevans photometric model to determine spectral albedos and extinction coefficients. The thin cold ice of these experiments had albedos which were comparable to the values for the thicker warmer ice examined by previous researchers; however, extinction coefficients were 1.5 to 15 times greater. Qualitative relationships between the optical properties and the physical state of the ice were observed. As the ice temperature decreased (and the brine volume increased) both albedo and extinction coefficient increased; when the ice temperature dropped below the eutectic point the increase was drastic. The dependence of albedo and extinction coefficient on the brine content of the ice was found to be complex with both the brine volume and its vertical distribution being significant. Variations in

ice salinity over the range 4 ‰ to 14 ‰ did not influence the optical properties. Increases in albedo and extinction coefficient were primarily a result of changes in the ice structure which enhanced scattering.

A four stream discrete ordinates photometric model was developed to treat the case of a floating ice slab. The model included both anisotropic scattering and refraction at the boundaries. The effects on albedo and transmittance of variations in such model parameters as the single scattering albedo and the phase function were investigated. Using one and two layer models, theoretical albedos and transmittances were compared to experimental values. The four stream model was further applied to investigate such topics as the depth dependence of irradiance, cases of direct beam incident radiation, the spectral dependence of albedo and transmittance, and the effects of surface layers. It was suggested that future laboratory research be oriented towards determination of single scattering albedos and phase functions for an extensive range of ice types.

TABLE OF CONTENTS

List of Figures	iv
List of Tables	viii
List of Symbols	ix
Acknowledgments	xi
Chapter One: Background	1
1.1 Introduction	1
1.2 Previous Experimental Research	3
1.2.1 Albedos	3
1.2.2 Extinction Coefficients	5
1.2.3 Correlation of Optical Properties and the Physical State of the Ice	6
Chapter Two: Radiative Transfer Models	8
2.1 Introduction	8
2.2 Dunkle and Bevans Model	8
2.3 Discrete Ordinates Method (DOM)	13
2.3.1 Background	13
2.3.2 Determination of Boundary Conditions	20
Case of No Refraction	20
Considering Refraction	22
Chapter Three: Experimental Apparatus and Techniques	31
3.1 Apparatus and Procedures	31
3.2 Data Reduction	38
3.2.1 Optical Measurements	38
3.2.2 Physical Measurements	41
3.3 Error Analysis	43
3.3.1 Optical Measurements	43
3.3.2 Physical Measurements	45
Chapter Four: Experimental Results	48
4.1 Introduction	48
4.2 Selected Results	48
4.2.1 Fresh Ice Results	48
4.2.2 Salt Ice Results: Experiment 5	55
4.2.3 Thermal Determination of Extinction Coefficients	66
4.3 Correlation of Optical Properties and Physical Parameters	68
4.3.1 Overview	68
4.3.2 The Effects of Ice Thickness	71
4.3.3 The Effects of Air Temperature During Freezing and Growth Rate	75
4.3.4 The Effects of Temperature, Salinity, and Brine Volume	83
4.3.5 Discussion	94

Accession For	
NTIS GRA&I	<input checked="" type="checkbox"/>
DOC TAB	<input type="checkbox"/>
Unannounced	<input type="checkbox"/>
Justification	<input type="checkbox"/>
By	
Distribution/	
Availability Codes	
Dist	Avail and/or special
A	

	Page
Chapter Five: Four Stream Modeling	102
5.1 Introduction	102
5.2 Parameter Study	103
5.2.1 Parameters of the Discrete Ordinates Method	103
5.2.2 Sensitivity of Albedo and Transmittance to the DOM Parameters	108
The Phase Function	108
Thickness and Single Scattering Albedo	108
The Effects of Refraction	112
5.3 Comparison of Theoretical and Experimental Albedos and Transmittances at 650 nm	112
5.3.1 One Layer Model	112
5.3.2 Two Layer Model	116
5.4 Further Applications of the Four Stream Model	118
5.4.1 Depth Dependence of Irradiance	118
5.4.2 Direct Beam Incident Radiation	121
5.4.3 Spectral Albedos and Transmittances	123
Chapter Six: Summary and Suggestions for Future Research	131
Bibliography	135
Appendix A: Additional Optical Results	141

LIST OF FIGURES

Figure	Page
1.1. Review of spectral extinction coefficients	7
2.1. Geometry of Dunkle and Bevans model	10
2.2. Geometry of four stream model	15
2.3. Reflection and refraction at an interface	23
2.4. Effects of refraction for a floating ice slab	24
2.5. The angular distribution of isotropic incident radiation undergoing refraction	26
3.1. The tank system	32
3.2. Experimental apparatus; the sun and the coupling box	34
3.3. Flow chart of data reduction and analysis	39
3.4. Normalized incident radiation for clear and cloudy skies	42
3.5. Range of uncertainty in albedo due to instrumental noise	44
3.6. Effects of deconvolution on albedo	46
3.7. Thermistor uncertainty	47
4.1. Spectral albedos for fresh ice	52
4.2. Photographs of scattering by cylindrical bubbles in fresh ice	54
4.3. Temperature profiles for Experiment 5	56
4.4. Salinity profiles for Experiment 5	57
4.5. Ice growth data for Experiment 5	59
4.6. Ice slab from Experiment 5 photographed in transmitted light	60
4.7. Ice slab from Experiment 5 photographed through crossed polaroids	61
4.8. Spectral albedos for Experiment 5	62
4.9. Spectral transmission profiles from Experiment 5 for ice 23.9 cm thick	64

Figure	Page
4.10. Extinction coefficients from Experiment 5 for ice 23.9 cm thick.	65
4.11. Temperature and salinity profiles used in thermal calculations of extinction coefficient	69
4.12. Profile of heat absorbed during a 200 minute period of illumination	70
4.13. Isopleths of albedo as a function of wavelength and thickness	72
4.14. Bulk albedo as a function of ice thickness	73
4.15. Isopleths of bulk albedo as a function of air temperature during freezing and ice thickness	76
4.16. Isopleths of bulk albedo as a function of growth rate and ice thickness	77
4.17. Spectral albedo comparisons for sea ice grown at different air temperatures	79
4.18. Comparison of spectral extinction coefficients for ice grown at different air temperatures	80
4.19. Comparison of spectral albedos for ice of similar temperature profiles, but grown at different air temperatures	81
4.20. Comparison of spectral extinction coefficients for ice of similar temperature profiles, but grown at different air temperatures	82
4.21. Isopleths of brine volume as a function of temperature and salinity	84
4.22. Temperature profiles for the warming phase of Experiment 6	86
4.23. Spectral albedos for the warming phase of Experiment 6	87
4.24. Spectral extinction coefficients for the warming phase of Experiment 6	88
4.25. Brine volume versus bulk albedo for measurements taken during the warming phase of Experiments 3, 5, and 6	89
4.26. Salinity profiles for ice grown from water of different salinities	91
4.27. Spectral albedos for ice grown from water of different salinities	92

Figure	Page
4.28. Spectral extinction coefficients for ice grown at an air temperature of -20°C from water of 16 ‰ and 30 ‰	93
4.29. Microphotographs of horizontal thin sections at temperatures of -27°C , -7°C , -4°C , and -1°C .	97
5.1. Interrelationship between single scattering albedo, optical thickness, and physical thickness	104
5.2. Isotropic and Henyey-Greenstein ($g = .5$ and $.75$) phase functions	106
5.3. Phase function determination from preliminary results of scattering experiments	107
5.4. Effect of asymmetry parameter (g) on albedo and transmittance	109
5.5. Isopleths of albedo as a function of $\bar{\omega}_0$ and ice thickness	110
5.6. Isopleths of transmittance as a function of $\bar{\omega}_0$ and ice thickness	111
5.7. Normalized downwelling irradiance at 650 nm as a function of depth	119
5.8. Normalized net irradiance at 650 nm as a function of depth	120
5.9. Albedo and transmittance at 650 nm as a function of solar zenith angle	122
5.10. Comparison of experimental and theoretical spectral albedos at 650 nm for ice 21 cm thick	125
5.11. Spectral albedos calculated for ice ranging in thickness from 2.5 to 25 cm	127
5.12. Spectral transmittances calculated for ice ranging in thickness from 2.5 to 25 cm	128
5.13. Effect of surface layer on albedo	129
A.1. Spectral albedos for growth phase of Experiment 3	143
A.2. Spectral albedos for warming phase of Experiment 3	144
A.3. Spectral extinction coefficients for warming phase of Experiment 3	145
A.4. Spectral albedos for growth phase of Experiment 4	146

Figure	Page
A.5. Spectral albedos for warming phase of Experiment 4	147
A.6. Spectral extinction coefficients for warming phase of Experiment 4	148
A.7. Spectral albedos for warming phase of Experiment 5	149
A.8. Spectral extinction coefficients for warming phase of Experiment 5	150
A.9. Spectral albedos for growth phase of Experiment 6	151

LIST OF TABLES

Table	Page
1.1. Review of wavelength integrated albedos	4
3.1. Experimental procedures	37
4.1. Summary of tank experiments	49
4.2. Ice thickness and air temperatures for experimental sites	50
4.3. Ratio of $\alpha_{500}/\alpha_{600}$ as a function of ice thickness	63
4.4. Influence of growth rate on α_{600} and κ_{600}	83
5.1. Effect of refraction on albedo and transmittance	113
5.2. One layer, four stream modeling of experimental results	115
5.3. Two layer, four stream modeling of cold ice	117
5.4. Absorption coefficients of ice	124
A.1. Summary of sites displayed in Appendix A	142

LIST OF SYMBOLS

a	platelet width
a_j 's	Gaussian weighting functions
c_s	specific heat
c_t	coefficient of thermal conductivity
E_0	direct beam solar radiance
E'_0	refracted direct beam solar radiance
F_{net}	net irradiance
F_0	incident downwelling irradiance
$F_{\downarrow}(z, \lambda)$	downwelling spectral irradiance
$F_{\uparrow}(z, \lambda)$	upwelling spectral irradiance
f	growth rate
g	asymmetry factor
H	ice thickness
I	radiance
I_R	reflected radiance
I_0	incident radiance
I'_0	transmitted radiance
k_{λ}	spectral absorption coefficients
k_j 's	eigenvalues in the discrete ordinates method
L_f	latent heat of fusion
n	index of refraction
$p(\mu, \mu')$	phase function
$P_{\ell}(X)$	Legendre polynomials
ΔQ	heat absorbed or lost

R_0	specular reflection from the air-ice interface
r_λ	specular volume reflectance coefficient
S	salinity (‰)
S_n	interprobe scaling factors
S	source function
T	temperature (°C)
T_a	air temperature
T_f	freezing temperature
$T(z,\lambda)$	spectral transmittance
t	time
z	depth within the ice
α_B	bulk albedo
$\alpha(\lambda)$	spectral albedo
θ	inclination to the vertical
κ	extinction coefficient
λ	wavelength
μ	$\cos \theta$
μ_0	cosine of solar zenith angle
v_B	brine volume
π	3.14
ρ_{ice}	density of ice
σ	scattering coefficient
τ	optical depth
τ_N	optical thickness
$\tilde{\omega}_0$	single scattering albedo

ACKNOWLEDGMENTS

During the course of this research I have benefited from the generous assistance of many people. This work has been greatly influenced by the guidance of Dr. Thomas Grenfell. I would like to express my deepest gratitude for the many suggestions, patient explanations, encouragement and support, and mainly for the countless hours of his time that he gave me.

I appreciate the considerable time and assistance given me by the members of my Supervisory Committee: Professors Charles Raymond, Norbert Untersteiner, Peter Hobbs, and T. Saunders English. Special thanks are due Dr. Gary Maykut for his many suggestions during the course of this research and for his extremely helpful review of an earlier version of this manuscript.

I would like to thank Robert Bindschadler, Beverly Hartline, David Hedrick, Jerry Johnson, and Rich Metcalf for their assistance and consultation. Your help and encouragement are deeply appreciated. Thanks to Miriam Lorette for her unerring guidance through the labyrinth of university procedures. I am indebted to Phyllis Brien for her tireless efforts in the final preparation of this report.

For their continual support and encouragement I am particularly grateful to the members of my family. Finally, I thank Kathy Jones, not only for her considerable scientific assistance during this project, but also for supplying the necessary encouragement and motivation for me to complete the project.

I acknowledge the Office of Naval Research, Arctic Program, under Contract N00014-76-C-0234 for their assistance which made this project possible.

CHAPTER ONE

BACKGROUND

1.1 INTRODUCTION

The overall energy balance of the polar regions is greatly influenced by the reflection, absorption, and transmissions of short-wave radiation by sea ice. The amount and spectral distribution of light penetrating into and under the ice is biologically important in determining primary productivity. Thermodynamically radiation penetration is of interest since heat absorbed in the ice or upper ocean can retard freezing or contribute to melting, thus affecting the equilibrium thickness of the ice.

The ice cover of the Arctic Ocean is both vertically and horizontally complex. Vertically, the ice exhibits variations in crystal structure, brine volume, temperature, and bubble density. Horizontally, thickness can vary from open water to thick pressure ice over distances of only a few meters; surface conditions are diverse including melt ponds, bare ice, and snow covered ice.

Optically, sea ice is a complex medium. Unlike its constituent parts of brine and fresh ice, sea ice is dominated optically by scattering rather than absorption. The intricate and highly variable structure of sea ice consisting of air bubbles, ice platelets, and brine pockets and channels considerably complicates the processes of radiative transfer within the medium.

The majority of the previous research on the optical properties of sea ice has been concerned with thick ice. Both spectral and

wavelength integrated albedos and extinction coefficients have been determined for first-year and multiyear ice under a variety of field conditions. However, due to the physical hazards involved in field measurements, the optical properties of young sea ice are virtually unknown. Although such thin ice accounts for only a small percentage of the ice cover, it transmits large amounts of energy to the ocean and hence its influence is important to the regional heat budget (Maykut, 1978).

The only practical way to study the optical properties of young ice is through laboratory experiments which allow environmental control and avoid the inherent hazards of the field. This report describes the results of a laboratory program designed to investigate the optical properties of young ice. The term "optical properties" refers to the radiative parameters of albedo and extinction coefficient over the wavelength interval 400 to 1000 nanometers. In addition to the determination of these optical properties, their dependence on such physical parameters as growth rate, air temperature, salinity, and brine volume was examined. An attempt was also made to relate, through a photographic analysis, variations in the optical properties to changes in the ice structure.

The final goal of this research was to acquire, through photometric modeling, a more precise description of and greater physical insight into the radiative processes occurring in thin sea ice. Being unable to treat such complications as anisotropic scattering, direct beam incident radiation, thin slabs, and refraction, photometric models previously applied to sea ice are inadequate for this task. A more

powerful model based on the discrete ordinates method (Chandrasekhar, 1950) was therefore developed for this purpose.

1.2 PREVIOUS EXPERIMENTAL RESEARCH

1.2.1 Albedos

Due to the importance of net shortwave radiation in heat budget calculations, measurements of albedos have long been a routine part of data collection in the Arctic. Typical values of bulk albedo are .06-.1 for open water, .2-.6 for melt ponds, .5-.7 for melting bare ice, to as much as .9 for freshly fallen snow. Areally averaged albedos have been measured from high towers and aircraft. Hansen (1961) and Langleben (1971) have formulated empirical relations between albedo, the degree of puddling and the amount of open water. Selected results of previous measurements of wavelength integrated albedo are summarized in Table 1.1.

Grenfell and Maykut (1978) have determined spectral albedos, from 400 to 1000 nm, for an extensive range of arctic ice and snow conditions. Their results indicate a wavelength dependent albedo displaying larger values at shorter wavelengths. Both the magnitude and the shape of the albedo curve are extremely sensitive to the presence of liquid water in the surface layer. A reduction of albedo, much more pronounced at longer wavelengths, occurs when surface water is present. Pond covered ice has a maximum albedo at short wavelengths with a severe decrease, by more than a factor of five, from 500 to 800 nm, eventually tapering at 1000 nm to a value determined only by specular reflection. For bare ice the magnitude of the albedo increases and its wavelengths dependence sharply declines.

Table 1.1: Review of Wavelength Integrated Albedos

SURFACE TYPE	SKY CONDITION	ALBEDO	INSTRUMENT	REFERENCE
Smooth water	Cloudy	.06	Theoretical	Burt, 1954
Mature melt pond	Cloudy	.29	Spectrophotometer	Grenfell and Maykut, 1978
Melting blue ice	Cloudy	.32	Spectrophotometer	Grenfell and Maykut, 1978
Melting white ice	Cloudy	.70	Spectrophotometer	Grenfell and Maykut, 1978
Frozen white ice	Cloudy	.74	Spectrophotometer	Grenfell and Maykut, 1978
Melting old snow	Cloudy	.77	Spectrophotometer	Grenfell and Maykut, 1978
Puddled ice	Clear	.59-.32P	Kipps: helicopter	Langleben, 1971
Open water, puddled ice	Cloudy	I(.65-.38P)	Pyranometer: plane	Hansen, 1961
Melting snow and ice	Varied	.68	—	Chernogovskii, 1963
Melting snow and ice	Varied	.56	—	Chernogovskii, 1963
Melt pond	Varied	.40	—	Chernogovskii, 1963
Dry snow	Cloudy	.84	Kipp Radiometer	Grenfell and Maykut, 1978

P is the percent area covered by ponds and I is the percent area covered by any form of ice.

1.2.2 Extinction Coefficients

While considerably fewer in number, measurements of radiation extinction in thick first-year and multiyear ice have been made. Untersteiner (1961), from changes in ice temperature profiles, calculated an optical bulk extinction coefficient of $.017 \text{ cm}^{-1}$ for multiyear sea ice. Using photometric cells Thomas (1963) measured bulk extinction coefficients of $.011 \text{ cm}^{-1}$ for pack ice and $.0219 \text{ cm}^{-1}$ for shore fast ice. Weller and Schwerdtfeger (1967), studying 135 cm thick antarctic sea ice, determined values of bulk extinction coefficient of $.012 \text{ cm}^{-1}$ and $.010 \text{ cm}^{-1}$ using data from a thermopile radiometer and temperature profiles respectively.

Spectral measurements of light penetration through first-year (Maykut and Grenfell, 1975) and multiyear (Grenfell and Maykut, 1978) sea ice were taken with a submersible spectrophotometer. The wide range of ice types investigated showed minimum extinction coefficient for ice beneath an old melt pond; increasing for first-year blue ice, the interior of multiyear white ice and the surface granular layer of multiyear white ice. In all cases the spectral extinction coefficient was fairly constant from 400 to 500 nm, exhibiting a gradual change between 500 and 600 nm, then a dramatic increase beyond 600 nm.

An understanding of the optical properties of salt water and fresh ice is critical to effectively model the transfer of radiation within sea ice. There is an abundance of literature concerning the extinction of light in various water types (Neumann and Pierson, 1966). Goodrich (1970) and Hobbs (1974) provide reviews for both bubble free

and bubbly fresh ice. Spectral extinction coefficients, from 400 to 800 nm, for fresh ice and sea ice are summarized in Figure 1.1.

1.2.3 Correlation of Optical Properties and the Physical State of the Ice

To date there has been little research done in attempting to correlate the optical properties to the physical state of sea ice. Weller (1972), studying young sea ice, observed an increase of bulk albedo with thickness. Experiments conducted by Davis and Munis (1973), using a HeNe laser (633 nm) and ice samples frozen in a 55 gallon drum, indicated that extinction coefficient increased as the ice salinity increased.

Further investigations of the relationship between salinity and extinction coefficient were conducted by Lane (1975). Several small samples of various salinities were grown at a temperature of -20°C . Transmission was found to decrease as salinity increased, though the dependence weakened for salinity greater than 5 ‰. However, Lane's samples, being frozen solid from the outside to the center, are structurally and perhaps optically quite different from natural sea ice.

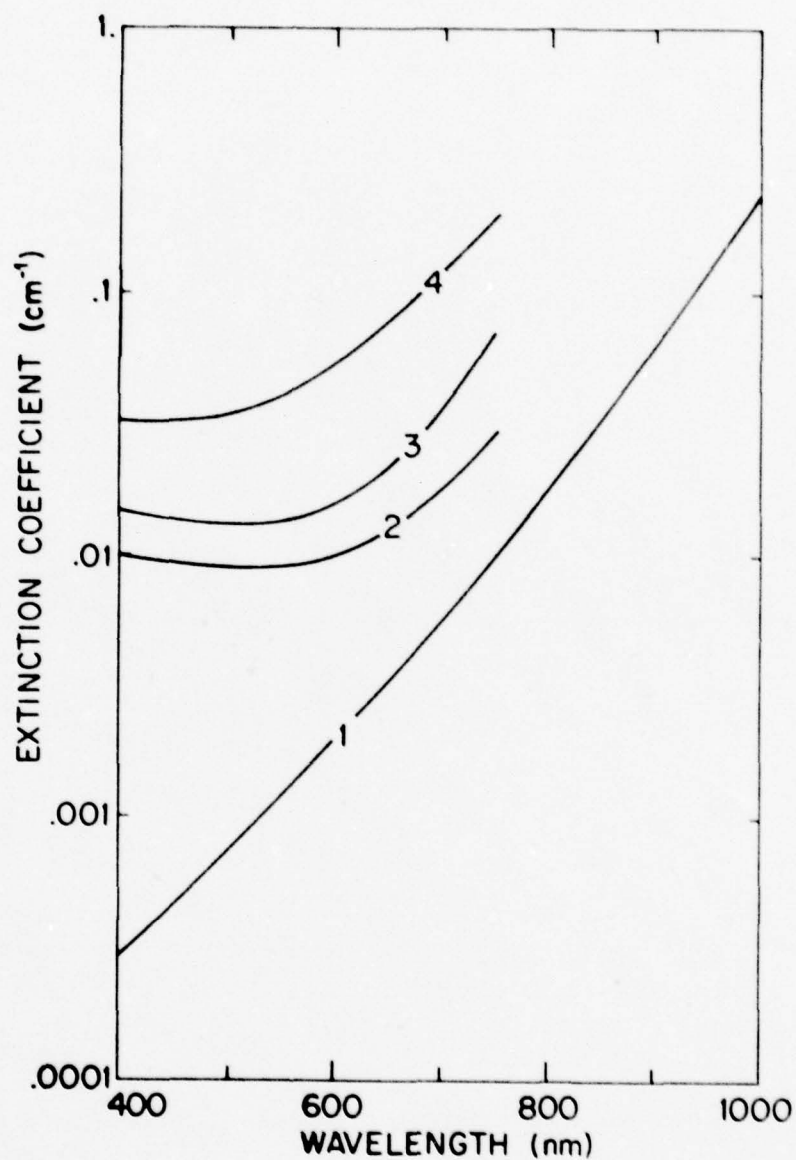


Figure 1.1: Review of spectral extinction coefficients: (1) bubble free fresh ice (Sauberer, 1950); (2) first-year blue ice; (3) interior of multiyear white ice; and (4) surface granular layer of multiyear white ice (2-4 from Grenfell and Maykut, 1978).

CHAPTER TWO

RADIATIVE TRANSFER MODELS

2.1 INTRODUCTION

Experiments investigating the optical properties of a medium typically measure incident, reflected, and transmitted irradiances. From these data the albedo and percentage of radiation transmitted are readily calculated, but additional information is needed for a more detailed analysis. To calculate and understand the optical properties and processes of a medium from measured irradiances, a suitable photometric model describing the transfer of radiation within the medium must be determined.

Historically, the Bouguer-Lambert law has been the simplest and most commonly used method for investigating radiation extinction in snow, fresh ice, sea ice, and water. While its simplicity is appealing, deficiencies of the model preclude its application in this experiment. In particular the Bouguer-Lambert model assumes an infinitely thick medium, which is invalid when examining young thin sea ice. Two photometric models are used to analyze the experimental results of this research, the Dunkle and Bevans and discrete ordinates methods.

2.2 DUNKLE AND BEVANS MODEL

Dunkle and Bevans (1956) developed a photometric model to analyze the transmittance and reflectance of a snow cover. This technique was modified by Grenfell and Maykut (1978) to calculate albedos and extinction coefficients for snow and sea ice. This approach was also

selected to determine extinction coefficients in the laboratory experiments.

The theory assumes an optically homogeneous medium, finite in depth, infinite in width and breadth, and isotropically scattering; the radiation field in the medium is assumed to be diffuse at all depths. In the present case the model is adopted to treat the additional complications of specular reflection at the upper surface and transmitted measurements made within, as well as beneath the ice. The geometry of the Dunkle and Bevens model for this experiment is illustrated in Figure 2.1. The Dunkle and Bevens model assumes two streams, an upwelling and a downwelling irradiance. This entails the solution of two simultaneous differential equations (Dunkle and Bevens, 1956),

$$dF_{\downarrow}(z, \lambda) = -k_{\lambda}F_{\downarrow}(z, \lambda)dz - r_{\lambda}F_{\downarrow}(z, \lambda)dz + r_{\lambda}F_{\uparrow}(z, \lambda)dz \quad (2.1)$$

$$dF_{\uparrow}(z, \lambda) = k_{\lambda}F_{\uparrow}(z, \lambda)dz - r_{\lambda}F_{\downarrow}(z, \lambda)dz + r_{\lambda}F_{\uparrow}(z, \lambda)dz \quad (2.2)$$

where $F_{\downarrow}(z, \lambda)$ is the downwelling spectral irradiance, $F_{\uparrow}(z, \lambda)$ is the upwelling spectral irradiance, k_{λ} is the spectral absorption coefficient, r_{λ} is the spectral volume reflectance coefficient, and z (increasing downward) is the depth within the ice. The boundary conditions for this problem are

$$z = 0 \quad F_{\downarrow}(0, \lambda) = (1-R_0)F_0 - R_0F_{\uparrow}(0, \lambda) \quad (2.3)$$

$$z = H \quad F_{\uparrow}(H, \lambda) = 0 \quad (2.4)$$

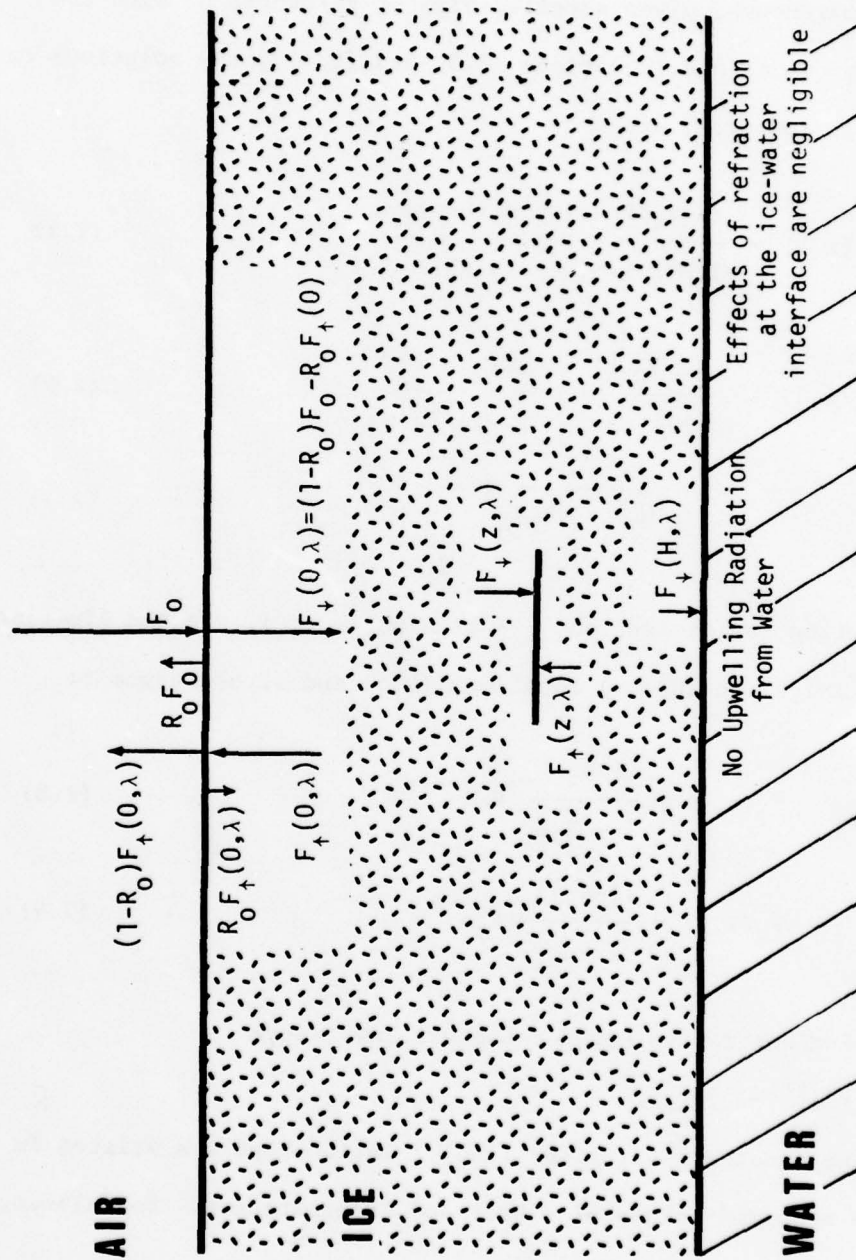


Figure 2.1: Geometry of Dunkle and Bevans model.

where R_0 is the specular reflection from the upper surface, F_0 is the incident downwelling irradiance at a given wavelength, and H is the thickness of the ice.

For a homogeneous, plane parallel slab of thickness H , with the above boundary conditions [Equations (2.3) and (2.4)], the solutions to Equations (2.1) and (2.2) are

$$F_{\downarrow}(z, \lambda) = \frac{(1-R_0)F_0 \sinh[\kappa_{\lambda}(H-z)+\gamma]}{\sinh[\kappa_{\lambda}H+\gamma] - R_0 \sinh[\kappa_{\lambda}H]} \quad (2.5)$$

$$F_{\uparrow}(z, \lambda) = \frac{(1-R_0)F_0 \sinh[\kappa_{\lambda}(H-z)]}{\sinh[\kappa_{\lambda}H+\gamma] - R_0 \sinh[\kappa_{\lambda}H]} \quad (2.6)$$

where

$$\kappa_{\lambda} = \sqrt{k_{\lambda}^2 + 2k_{\lambda}r_{\lambda}} \quad (2.7)$$

is the extinction coefficient and $\gamma = \operatorname{arcsinh}(\kappa_{\lambda}/r_{\lambda})$. In the limiting case of very thick ice ($H \rightarrow \infty$) Equations (2.5) and (2.6) reduce to

$$F_{\downarrow}(z, \lambda) = \frac{1-R_0}{1 - R_0\beta_{\lambda}} F_0 e^{-\kappa_{\lambda}z} \quad (2.8)$$

$$F_{\uparrow}(z, \lambda) = \frac{(1-R_0)\beta_{\lambda}}{1-R_0\beta_{\lambda}} F_0 e^{-\kappa_{\lambda}z} \quad (2.9)$$

which is equivalent to the Bouguer-Lambert law (where

$$\beta_{\lambda} = [(r_{\lambda}^2 + \kappa_{\lambda}^2)^{1/2} - \kappa_{\lambda}] / r_{\lambda}).$$

Combining Equations (2.5) and (2.6) relationships are written in terms of the measured values of albedo and transmittance. For albedo, $\alpha(\lambda)$,

$$\alpha(\lambda) = \frac{R_0 F_0 + (1-R_0) F_{\uparrow}(0, \lambda)}{F_0} \quad (2.10)$$

Evaluating Equation (2.6) for z equal to zero,

$$F_{\uparrow}(0, \lambda) = \frac{(1-R_0)F_0 \sinh(\kappa_{\lambda} H)}{\sinh(\kappa_{\lambda} H + \gamma) - R_0 \sinh(\kappa_{\lambda} H)} \quad (2.11)$$

and substituting into Equation (2.10),

$$\alpha(\lambda) = R_0 + \frac{(1-R_0)^2 \sinh(\kappa_{\lambda} H)}{\sinh(\kappa_{\lambda} H + \gamma) - R_0 \sinh(\kappa_{\lambda} H)} \quad (2.12)$$

The transmittance, $T(z, \lambda)$, is expressed as

$$T(z, \lambda) = \frac{F_{\downarrow}(z, \lambda)}{F_0} = \frac{(1-R_0) \sinh[\kappa_{\lambda} (H-z) + \gamma]}{\sinh(\kappa_{\lambda} H + \gamma) - R_0 \sinh \kappa_{\lambda} H} \quad (2.13)$$

Equations (2.12) and (2.13) cannot be explicitly solved for κ_{λ} and r_{λ} . Instead the equations are numerically inverted using a two-dimensional Newton-Raphson scheme. This entails the iterative solution of the simultaneous equations

$$(\alpha - f)_i - \left. \frac{\partial f}{\partial \kappa} \right|_i \Delta \kappa - \left. \frac{\partial f}{\partial r} \right|_i \Delta r = 0 \quad (2.14)$$

$$(T - g)_i - \left. \frac{\partial g}{\partial \kappa} \right|_i \Delta \kappa - \left. \frac{\partial g}{\partial r} \right|_i \Delta r = 0 \quad (2.15)$$

where α and $f(\kappa, r)$ are respectively the observed and calculated albedo and T and $g(\kappa, r)$ are the observed and calculated transmittance.

Equations (2.14) and (2.15) are expressed in matrix form by

$$\begin{pmatrix} \left. \frac{\partial f}{\partial \kappa} \right|_i & \left. \frac{\partial f}{\partial r} \right|_i \\ \left. \frac{\partial g}{\partial \kappa} \right|_i & \left. \frac{\partial g}{\partial r} \right|_i \end{pmatrix} \begin{pmatrix} \Delta \kappa \\ \Delta r \end{pmatrix} = \begin{pmatrix} (\alpha - f)_i \\ (T - g)_i \end{pmatrix} \quad (2.16)$$

Initial values of κ and r are selected using the Bouguer-Lambert model and substituted into Equation (2.16). Values of $\Delta\kappa$ and Δr are then determined, κ and r adjusted, and the process repeated. The iteration continues until the change in κ and r is less than one percent. Convergence is rapid, typically occurring within 3 iterations.

Using the Dunkle and Bevens method spectral reflectances and extinction coefficients are readily calculated and compared to results of previous researchers. However with only two streams the Dunkle and Bevens model provides no information concerning the angular distribution of radiation within the ice. The model is also limited by the assumptions of diffuse incident radiation and isotropic scattering. There is evidence to suggest that the scattering in sea ice is quite anisotropic (Grenfell and Hedrick, personal communication). These constraints limit the applicability of the Dunkle and Bevens method. In order to accurately describe the radiative transfer processes occurring in the ice, a more general photometric model is needed.

2.3 DISCRETE ORDINATES METHOD (DOM)

2.3.1 Background

Chandrasekhar (1950), using a discrete ordinates method, derived solutions to the equation of radiative transfer in a plane parallel, homogeneous, multiple scattering medium. The discrete ordinates, or streams, refer to the angles at which radiances are determined. Liou (1973, 1974) developed a numerical model, based on Chandrasekhar's solutions, to investigate radiative transfer within cloudy and hazy

atmospheres. Analytic solutions were determined for the two and four stream cases (Liou, 1974).

A primary interest in vertical irradiance distributions and the need to investigate a large number of cases dictated the use of a four stream model in this research. Numerical experiments by Liou (1974) established the effectiveness of the four stream model in studies of irradiance distributions in turbid media. A two stream model was unacceptable since errors became prohibitively large for optically thin layers. Higher order models, while offering greater angular resolution of radiance, were complicated by numerical instabilities and iterative solution schemes.

The model used here is based on the four stream solution discussed by Liou (1974). However the new application of the model to sea ice introduces several complications, primarily associated with boundary conditions and refractive effects. These difficulties are discussed in Section 2.3.2, while the remainder of this section is limited to a general description of the discrete ordinates method. The geometry of the four stream model is illustrated in Figure 2.2.

From Chandrasekhar (1950) the equation of radiative transfer for plane parallel atmospheres is

$$\mu \frac{dI(\tau, \mu, \phi)}{d\tau} = I(\tau, \mu, \phi) - S(\tau, \mu, \phi) \quad (2.17)$$

where I is the radiance, ϕ is the azimuth angle, μ is equal to $\cos \theta$, and θ is the inclination to the vertical. The sign convention is that $-\mu$'s represent downward angles. The optical depth τ can be expressed

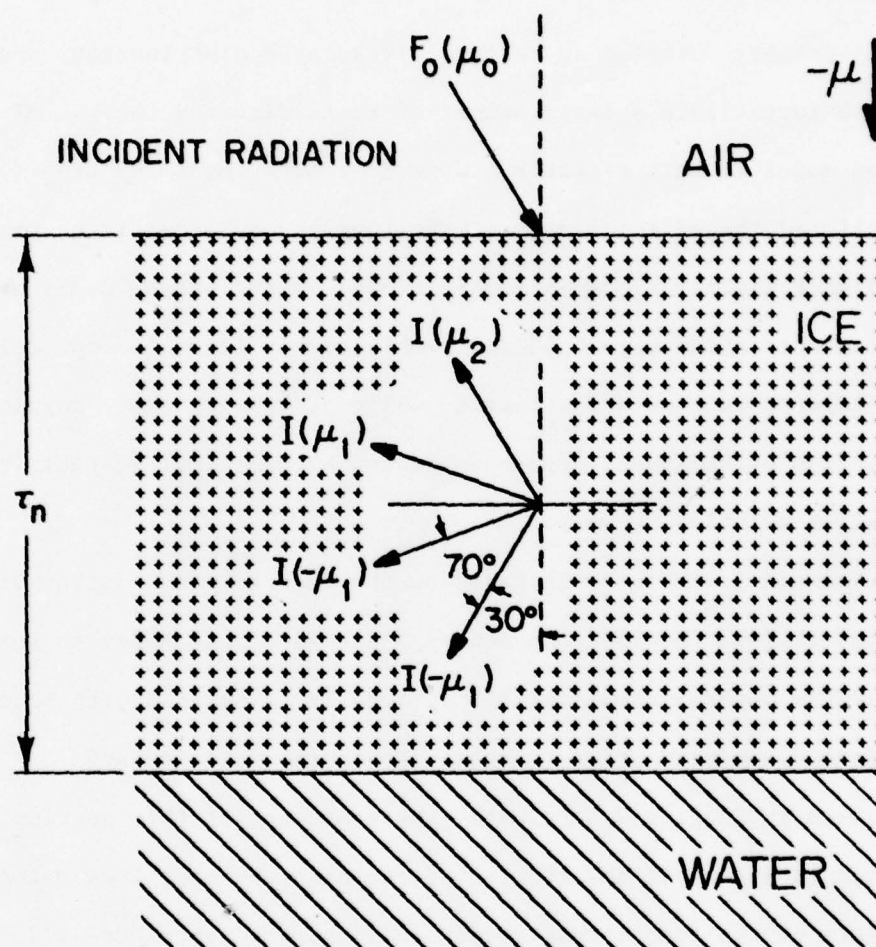


Figure 2.2: Geometry of four stream model.

in terms of the scattering coefficient σ , and the absorption coefficient k ,

$$\tau = -(\sigma + k)z \quad . \quad (2.18)$$

The minus sign is a result of the custom that τ increases downward and z decreases downward. The source function S describes the contribution of multiple scattering and for a plane parallel scattering atmosphere with a direct incident beam is expressed as

$$\begin{aligned} S(\tau, \mu, \phi) = & \frac{1}{4\pi} \int_{-1}^1 \int_0^{2\pi} p(\mu, \phi, \mu', \phi') I(\tau, \mu', \phi') d\mu' d\phi' \\ & + \frac{1}{4} E_0 p(\mu, \phi, \mu_0, \phi_0) e^{-\tau/\mu_0} \quad . \end{aligned} \quad (2.19)$$

For this analysis axial symmetry is assumed and Equation (2.17) reduces to

$$\begin{aligned} \mu \frac{dI(\tau, \mu)}{d\tau} = & I(\tau, \mu) - \frac{1}{2} \int_{-1}^1 p(\mu, \mu') I(\tau, \mu') d\mu' \\ & - \frac{1}{4} E_0 p(\mu, \mu_0) e^{-\tau/\mu_0} \end{aligned} \quad (2.20)$$

where E_0 is the solar radiance and μ_0 is the cosine of the solar zenith angle, defined to be positive.

The scattering processes within the medium are jointly defined by the phase function, $p(\mu, \mu')$, and the single scattering albedo, $\tilde{\omega}_0$. The phase function describes the angular dependence of scattering and

typically is normalized so that the integral over angle is equal to one. Different types of scattering from isotropic to strongly anisotropic may be represented by the proper choice of a phase function. Expressed in terms of Legendre polynomials,

$$p(\mu, \mu') = \sum_{\ell=0}^N \tilde{\omega}_{\ell} P_{\ell}(\mu) P_{\ell}(\mu') \quad (2.21)$$

where N is three for a four stream model. A major limitation of the four stream model is that a four point expansion cannot accurately describe complex phase functions.

The single scattering albedo $\tilde{\omega}_0$ describes the relative importance of scattering and absorbing processes,

$$\tilde{\omega}_0 = \frac{\sigma}{\sigma + \kappa} \quad (2.22)$$

$\tilde{\omega}_0$ ranges from zero for a purely absorbing medium to one for a purely scattering medium. The higher order $\tilde{\omega}_{\ell}$'s used in Equation (2.21) can be obtained from the expression

$$\tilde{\omega}_{\ell} = \frac{2\ell+1}{2} \int_{-1}^1 p(x) P_{\ell}(x) dx \quad (2.23)$$

which is derived from Equation (2.21) exploiting the orthogonality of the Legendre polynomials. For simple phase functions, such as isotropic or Rayleigh scattering, the integral in Equation (2.23) can be evaluated exactly, while for more complex phase functions numerical integration schemes must be used. The $\tilde{\omega}_{\ell}$'s for ℓ greater than zero, are normalized by multiplying the results of Equation (2.23) by $\tilde{\omega}_0$.

Expressing the integral in Equation (2.20) by a Gaussian quadrature,

$$\int_{-1}^1 p(\mu, \mu') I(\tau, \mu') d\mu' = \sum_{\substack{j=-2 \\ j \neq 0}}^2 a_j p(\mu, \mu_j) I(\tau, \mu_j) \quad (2.24)$$

Substituting Equations (2.21) and (2.23) into (2.20) for the four stream case results in

$$\begin{aligned} \mu_i \frac{dI(\tau, \mu_i)}{d\tau} = & I(\tau, \mu_i) - \frac{1}{2} \sum_{\ell=0}^3 \tilde{\omega}_\ell P_\ell(\mu_i) \sum_{\substack{j=-2 \\ j \neq 0}}^2 \mu_j P_\ell(\mu_j) I(\tau, \mu_j) \\ & - \frac{1}{4} E_0 \left[\sum_{\ell=0}^3 (-1)^\ell \tilde{\omega}_\ell P_\ell(\mu_i) P_\ell(\mu_0) \right] e^{-\tau/\mu_0} \end{aligned} \quad (2.25)$$

where the a_j 's are the Gaussian weighting functions, $a_1 = a_{-1} = .6521452$ and $a_2 = a_{-2} = .3478548$, and the μ_i represent the cosines of the discrete angles of the four streams, $\mu_{1,-1} = \pm .339981$ and $\mu_{2,-2} = \pm .8611363$.

Equation (2.20) defines a system of four simultaneous linear differential equations which were formally solved by Chandrasekhar (1950).

Chandrasekhar obtained a solution of the homogeneous system of the form

$$I(\tau, \mu_i) \propto \frac{e^{-k_j \tau}}{1 + \mu_i k_j} \sum_{\ell=0}^N \tilde{\omega}_\ell \xi_\ell P_\ell(\mu_i) \quad (2.26)$$

and a nonhomogeneous system with the particular solution,

$$I(\tau, \mu_i) = Z(\mu_i) e^{-\tau/\mu_0} \quad (2.27)$$

The total solution is the superposition of Equations (2.26) and (2.27).

Following the development of Chandrasekhar, Liou (1974) determined the analytic solution for a four stream model. After lengthy algebraic

manipulation an expression for radiance as a function of depth and angle was determined;

$$I(\tau, \mu_1) = \sum_{\substack{j=-2 \\ j \neq 0}}^2 L_j W_j(\mu_1) e^{-k_j \tau} + Z(\mu_1) e^{-\tau/\mu_0} \quad (2.28)$$

For a four stream model the functions $W_j(\mu_1)$ and $Z(\mu_1)$ expand to

$$W_j(\mu_1) = \frac{1}{1+\mu_1 k_j} \sum_{\ell=0}^3 \tilde{\omega}_\ell \xi_\ell(k_j) P_\ell(\mu_1) \quad (2.29)$$

$$Z(\mu_1) = \frac{\mu_0 E_0 (\mu_1^2 - \mu_0^2) (\mu_2^2 - \mu_0^2)}{4(\mu_0 + \mu_1) \mu_1^2 \mu_2^2 (1 - k_1^2 \mu_0^2) (1 - k_2^2 \mu_0^2)} \sum_{\ell=0}^3 \tilde{\omega}_\ell \xi_\ell\left(\frac{1}{\mu_0}\right) P_\ell(\mu_1) \quad (2.30)$$

The k_j 's denote the eigenvalues of the homogeneous differential equations, while the ξ_ℓ 's are proportionality constants which arise solving the associated homogeneous equations and can be calculated from the recursion formula

$$\xi_{\ell+1}(X) = \frac{2\ell+1-\tilde{\omega}_\ell}{X(\ell+1)} \xi_\ell(X) - \frac{\ell}{\ell+1} \xi_{\ell-1}(X) \quad (2.31)$$

where $\xi_0(X) = 1$ and $\xi_{-1}(X) = 0$.

The L_j 's in Equation (2.28) are constants of integration determined from the boundary conditions. The system of four equations [Equation (2.28)] and four unknowns (L_j 's) is expressed in matrix form and solved using a standard inversion routine. The determination of the proper boundary conditions representing the downwelling radiances at the upper boundary and the upwelling radiances at the lower boundary is discussed in Section 2.3.2.

To determine the upward, downward, and net irradiances at any level it is only necessary to express the integral of radiances as a sum of Gaussian quadratures and evaluate. The net irradiance is expressed by

$$F_{\text{net}}(\tau) = F_{\uparrow}(\tau) - F_{\downarrow}(\tau) = 2\pi \int_{-1}^1 I(\tau, \mu) \mu d\mu - \pi \mu_0 E_0 e^{-\tau/\mu_0}, \quad (2.32)$$

expanding the integral

$$F_{\text{net}}(\tau) = 2\pi \sum_{j=-2}^2 a_j I(\tau, \mu_j) \mu_j - \pi \mu_0 E_0 e^{-\tau/\mu_0}, \quad (2.33)$$

and correspondingly

$$F_{\uparrow}(\tau) = 2\pi [a_1 \mu_1 I(\tau, \mu_1) + a_2 \mu_2 I(\tau, \mu_2)] \quad (2.34)$$

$$F_{\downarrow}(\tau) = -2\pi [a_1 \mu_1 I(\tau, -\mu_1) + a_2 \mu_2 I(\tau, -\mu_2)] - \pi \mu_0 E_0 e^{-\tau/\mu_0}. \quad (2.35)$$

2.3.2 Determination of Boundary Conditions

With a general analytic four stream model developed by Liou (1974), the remaining theoretical difficulties are to determine the proper boundary conditions and derive expressions for albedo and transmittance for the case of a floating ice slab. This is done both neglecting and considering refraction.

Case of No Refraction

If refraction at the air-ice and ice-water interfaces is ignored, the boundary conditions are

$$I(-\mu_1, 0) = I(-\mu_2, 0) = C \quad (\text{upper boundary}) \quad (2.36)$$

$$I(\mu_1, \tau_N) = I(\mu_2, \tau_N) = 0 \quad (\text{lower boundary}) \quad (2.37)$$

where τ_N is the optical thickness of the ice slab. For isotropic incident radiation, representing cloudy sky conditions, C is equal to one and there is no direct beam component. To represent clear skies, C is assumed to be zero and the incident radiation field is defined by a direct beam of radiance E_0 at an angle $\arccos(\mu_0)$.

The albedo and transmittance are determined using

$$\alpha = \frac{F_{\uparrow}(0)}{F_0} \quad (2.38)$$

$$T = \frac{F_{\downarrow}(\tau_N)}{F_0} \quad (2.39)$$

Equations (2.34) and (2.35) are used to calculate $F_{\uparrow}(0)$ and $F_{\downarrow}(\tau_N)$, where F_0 is equal to π for isotropic incident radiation and $\mu_0 \pi E_0$ for an incident direct beam.

For a snow surface (Barkstrom, 1972) it is possible to consider refraction solely as a scattering phenomenon. However, for sea ice, it is usually necessary to calculate refractive effects at the interfaces explicitly.

Considering Refraction

When light passes from one medium to another of different index of refraction, Fresnel reflection and refraction occur. Figure 2.3 illustrates the elementary optical situation of a ray of light incident on a boundary between media with different indices of refraction. The angles θ , θ_R , and ϕ are related by

$$\theta = \theta_R \quad (2.40)$$

and from Snell's law

$$n_1 \sin \theta = n_2 \sin \phi, \quad (2.41)$$

where n_1 and n_2 are the respective indices of refraction.

It is also necessary to determine the relationship of the incident (I_0), reflected (I_R), and transmitted (I'_0) radiances. I_R is calculated from the Fresnel equations (Born and Wolfe, 1965) to be

$$I_R(\theta) = I_0(\theta) \frac{1}{2} \left(\frac{\sin^2(\theta - \phi)}{\sin^2(\theta + \phi)} + \frac{\tan^2(\theta - \phi)}{\tan^2(\theta + \phi)} \right) \quad (2.42)$$

The transmitted radiance is obtained from energy conservation,

$$I'_0(\phi) = \left(I_0(\theta) - I_R(\theta) \right) \frac{\cos \theta}{\cos \phi} \quad (2.43)$$

For a floating ice slab, refraction can occur at ice-water and ice-air interfaces, situations which are illustrated in Figure 2.4. Since it is assumed that there is no upwelling radiation from the water, refraction at the water-ice interface need not be considered. Due to the small difference in the value of n for water and ice, refractive

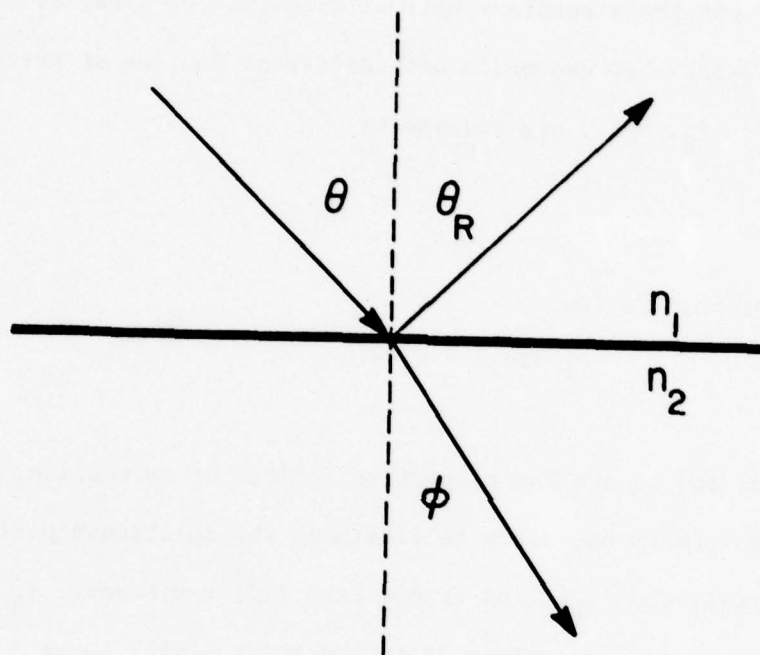


Figure 2.3: Reflection and refraction at an interface.

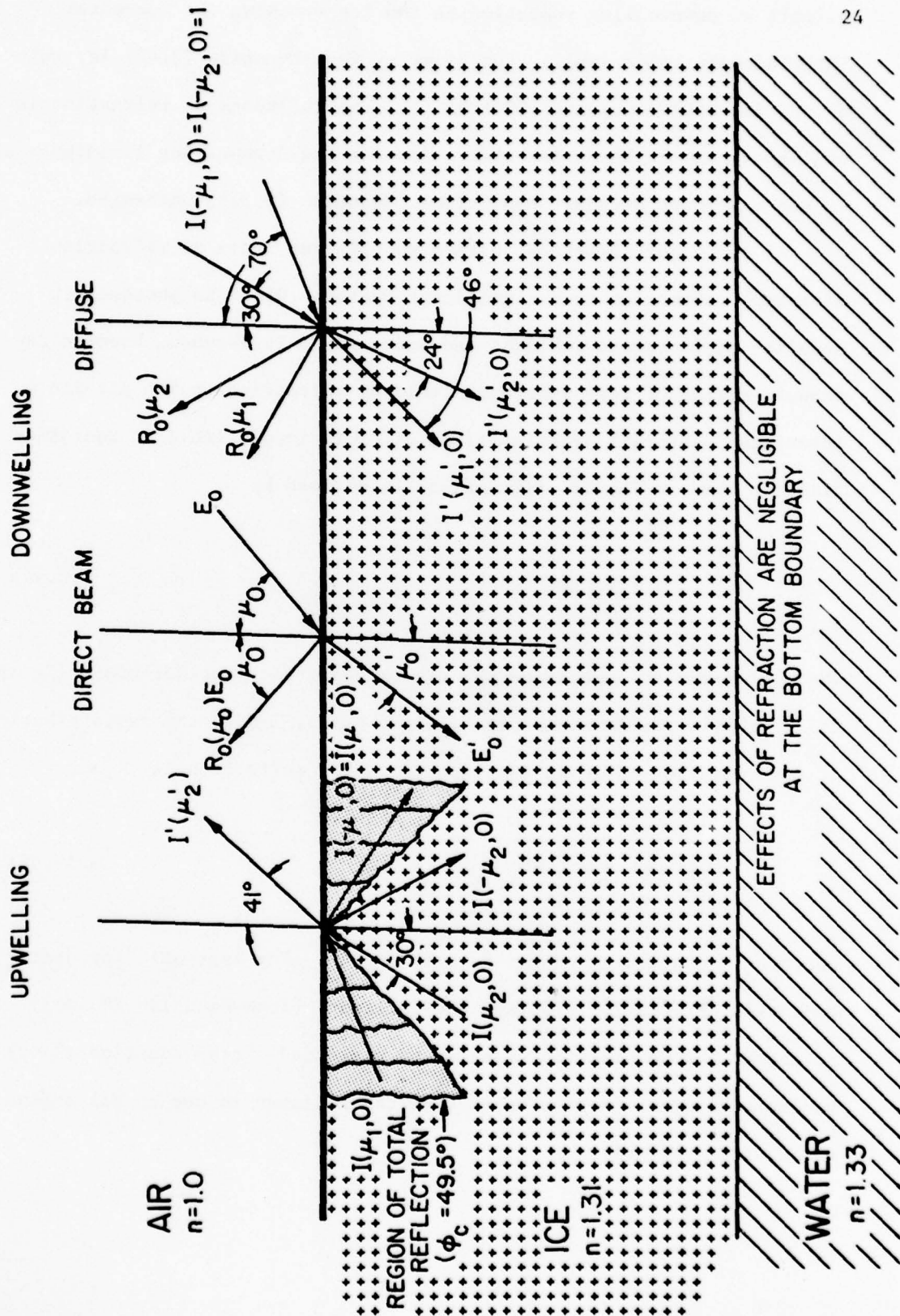


Figure 2.4: Effects of refraction for a floating ice slab.

effects on downwelling radiation in the ice reaching the ice-water interface are quite small. For example, from Equation (2.42) for unit I_0 , R_0 is .0001 at μ_2 and .0026 at μ_1 . The influence of refraction is negligible at the lower interface, leaving the downwelling irradiance at τ_N and the lower boundary conditions [Equation (2.37)] unchanged.

At the upper interface, with a much larger index of refraction mismatch, refraction is a significant factor. Often in photometric modeling an isotropic incident radiation field is assumed, however the transformation of this isotropic field by refraction at the air-ice interface is usually oversimplified. The isotropic incident radiation field in the air (before refraction) is defined by

$$I_{\text{air}}(\mu_a) = 1 \quad (2.44)$$

where $\mu_a = \cos \theta$. Determined by either geometric considerations (Jerov, 1976) or by variable transformation (Papoulis, 1965), the redistribution of the radiation field in Equation (2.44) by refraction is

$$I_{\text{ice}}(\mu_e) = n^2 (1 - I_R(\mu_a)) I_{\text{air}}(\mu_a) \quad (2.45)$$

where $\mu_e = \cos \phi$, and ranges from 1 to .646. For isotropic incident radiation, Figure 2.5 displays the incident [from Equation (2.44)], reflected [from Equation (2.42)] and refracted [from Equation (2.45)] radiation fields. Before refraction the radiance is one at all angles, while after refraction

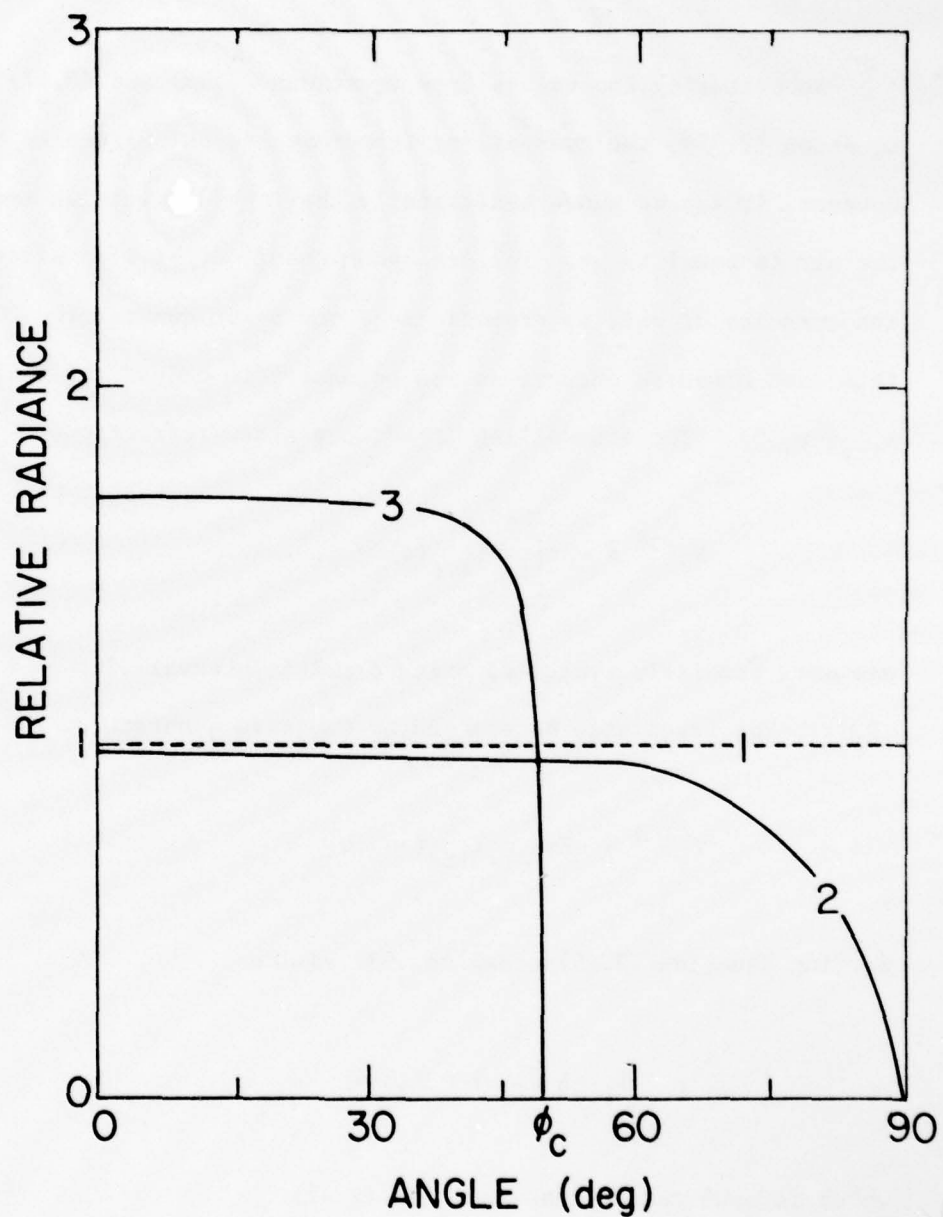


Figure 2.5: The angular distribution of isotropic incident radiation undergoing refraction ($\phi_c = 49.5^\circ$): (1) isotropic incident radiation; (2) incident radiation after the removal of specular reflection; and (3) radiation distribution in the ice after refraction

$$I_{ice}(-\mu_1, 0) = 0 \quad (2.46)$$

$$I_{ice}(-\mu_2, 0) = 1.67 \quad (2.47)$$

Substituting the values from Equations (2.46) and (2.47) into Equation (2.35), the downwelling irradiance is calculated to be -1.17π . However, it can be shown analytically that the downwelling irradiance in the air is equal to $-\pi$. The erroneous result of -1.17π is caused by the inaccuracies of what is essentially a one point quadrature. To avoid this and conserve energy, it was necessary to adjust the value of $I_{ice}(-\mu_2, 0)$. The downwelling irradiance after refraction,

$$F_0^{ice} = -2\pi \int_1^{.646} I_{ice}(\mu) d\mu \quad (2.48)$$

was more precisely evaluated using a multi-interval Simpson's rule as $.937\pi$. The irradiance determined by Gaussian quadratures reduces to

$$F_0^{ice} = -2\pi a_2 \mu_2 I_{ice}(-\mu_2, 0) \quad (2.49)$$

Setting Equation (2.49) equal to $.937$ yields

$$I_{ice}(-\mu_2, 0) = 1.564 \quad (2.50)$$

which is used rather than Equation (2.47).

The upper boundary conditions are further complicated by refraction and reflection of the upwelling radiation. Since $\arccos(\mu_1)$ is greater

than the critical angle ($\phi_c = 49.76^\circ$), $I(u_1, 0)$ is totally reflected and from the Fresnel equation .022 of $I(u_2, 0)$ is reflected. Combining these results with Equation (2.46) and (2.50) yields the upper boundary conditions for diffuse incident radiation.

$$I(-u_1, 0) = I(u_1, 0) \quad (2.51)$$

$$I(-u_2, 0) = .022 I(u_2, 0) + D \quad (2.52)$$

where $D = 1.564$.

If the incident radiation is a direct beam $E_0(u_0)$, the refracted beam $E'_0(u'_0)$ is determined from Equations (2.41), (2.42), and (2.43). The boundary conditions are the same as for diffuse incident [Equations (2.51) and (2.52)] except that for a direct beam D is equal to zero.

While refraction does not change the expression for transmittance [Equation (2.39)], it does complicate the calculation of albedo. To determine transmittance and albedo, F_0 , $F_t(\tau_N)$, and $F_{air\uparrow}(0)$ must be calculated. F_0 and $F_t(\tau_N)$ remain the same as the nonrefractive case, leaving transmittance unchanged. $F_{air\uparrow}(0)$, however, is quite different. It is important to remember that the albedo is the ratio of the incident downwelling to the upwelling irradiance in the air, before the incident light is refracted and after the upwelling is refracted. The model calculates upwelling radiances at angles u_1 and u_2 in the ice. In the case of no refraction

$$F_{air\uparrow}(0) = F_{ice\uparrow}(0) = 2\pi \left(a_1 u_1 I_{ice}(u_1, 0) + a_2 u_2 I_{ice}(u_2, 0) \right) \quad (2.53)$$

But when considering refraction, with $I_{ice}(\mu_1, 0)$ internally reflected, Equation (2.53) no longer is applicable.

It was decided that the albedo could most accurately be calculated by allowing $I_{ice}(\mu_1, 0)$ and $I_{ice}(\mu_2, 0)$ to define an upwelling radiation field of the form,

$$I_{ice}(\mu) = A\mu + B \quad (2.54)$$

with

$$A = \frac{[I_{ice}(\mu_1, 0) - I_{ice}(\mu_2, 0)]}{(\mu_1 - \mu_2)} \quad (2.55)$$

and

$$B = I_{ice}(\mu_1, 0) - A\mu_1 \quad (2.56)$$

The form of Equation (2.54) is the highest order possible with only two points. As a simple consistency check of Equation (2.54), the end points $I(1, 0)$ and $I(0, 0)$ are evaluated to insure that they are non-negative.

The upwelling irradiance emergent from the ice is expressed as

$$F_{air\uparrow}(0) = 2\pi \int_{\mu_c}^1 I_{ice}(\mu) (1 - R_F) \mu d\mu \quad (2.57)$$

The cosine of the critical angle, μ_c , is the lower limit of integration since light from zero to μ_c is internally reflected. R_F is a correction for the Fresnel reflection of the emergent radiation and is assumed to equal .065, which is the integrated value for Fresnel reflection under isotropic conditions. Equation (2.57) now becomes

$$F_{air\uparrow}(0) = 2\pi(.935) \int_{\mu_c}^1 (A\mu + B) \mu d\mu \quad (2.58)$$

integrating gives

$$F_{\text{air}\uparrow}(0) = 5.87 (.243 A + .291 B) \quad . \quad (2.59)$$

The upwelling irradiance in the air consists of $F_{\text{air}\uparrow}(0)$ plus a contribution from Fresnel reflection of the incident radiation,

$$F_{\text{total}}(0) = F_{\text{air}\uparrow}(0) + R_0 \quad (2.60)$$

where $R_0 = .065\pi$ for isotropic incident radiation and $R_0 = u_0 \pi I_R(u_0)$ for an incident direct beam, with I_R determined by Equation (2.42). By substituting $F_{\text{total}}(0)$ for $F_{\uparrow}(0)$ in Equation (2.38) the albedo, considering refraction, is calculated.

Based on this solution to the equation of radiative transfer a system of computer programs was written to investigate the optical processes of a floating ice slab. Model input parameters are optical thickness, phase function, and single scattering albedo. The four stream model calculated albedo, transmittance, and radiances and irradiances at any depth within the ice. Direct or diffuse incident radiation is introduced through the boundary conditions. The optical thickness can be varied from very small to semi-infinite. The single scattering albedo and phase function give considerable insight into the physics governing radiative transfer within the ice. The applications of the four stream model are discussed in Chapter Five.

CHAPTER THREE

EXPERIMENTAL APPARATUS AND TECHNIQUES

3.1 APPARATUS AND PROCEDURES

The experiments were performed in a cold room whose air temperature could be controlled over the range -40°C to $+10^{\circ}\text{C}$. Freezing occurred in a cylindrical plexiglas tank, 61 cm high and 116 cm in diameter (Figure 3.1). A cylindrical design was chosen to avoid stress concentrations, enabling the use of a very thin, .375 cm, plexiglas wall while maintaining structural integrity. Mirrored plexiglas was selected to reduce optical edge effects by making the ice sheet appear larger in areal extent. This was necessary to justify the theoretical assumption of a plane-parallel medium. The tank's base was 1.25 cm thick plexiglas painted black to minimize reflection. To prevent leaks from the tank silastic was used as an inner sealer. The bottom of the tank was insulated with 7.6 cm of "blue foam". Insulation for the walls was provided by 5.1 cm of "white foam" surrounded by 5 to 10 cm of loose zonolite aggregate and topped by weatherstripping. The tank and insulation were contained in a wooden catchbasin protecting against water spills should a leak occur.

The source of illumination was a "sun" consisting of nine, 500 watt incandescent light bulbs. Blue frosted superfluors with a color temperature of 4800°K were used since they provided more short wavelength light than conventional incandescent bulbs. To produce uniform illumination the lights were mounted on a glossy white circular piece of wood, one meter in diameter, in an array consisting of a hexagon with an inner

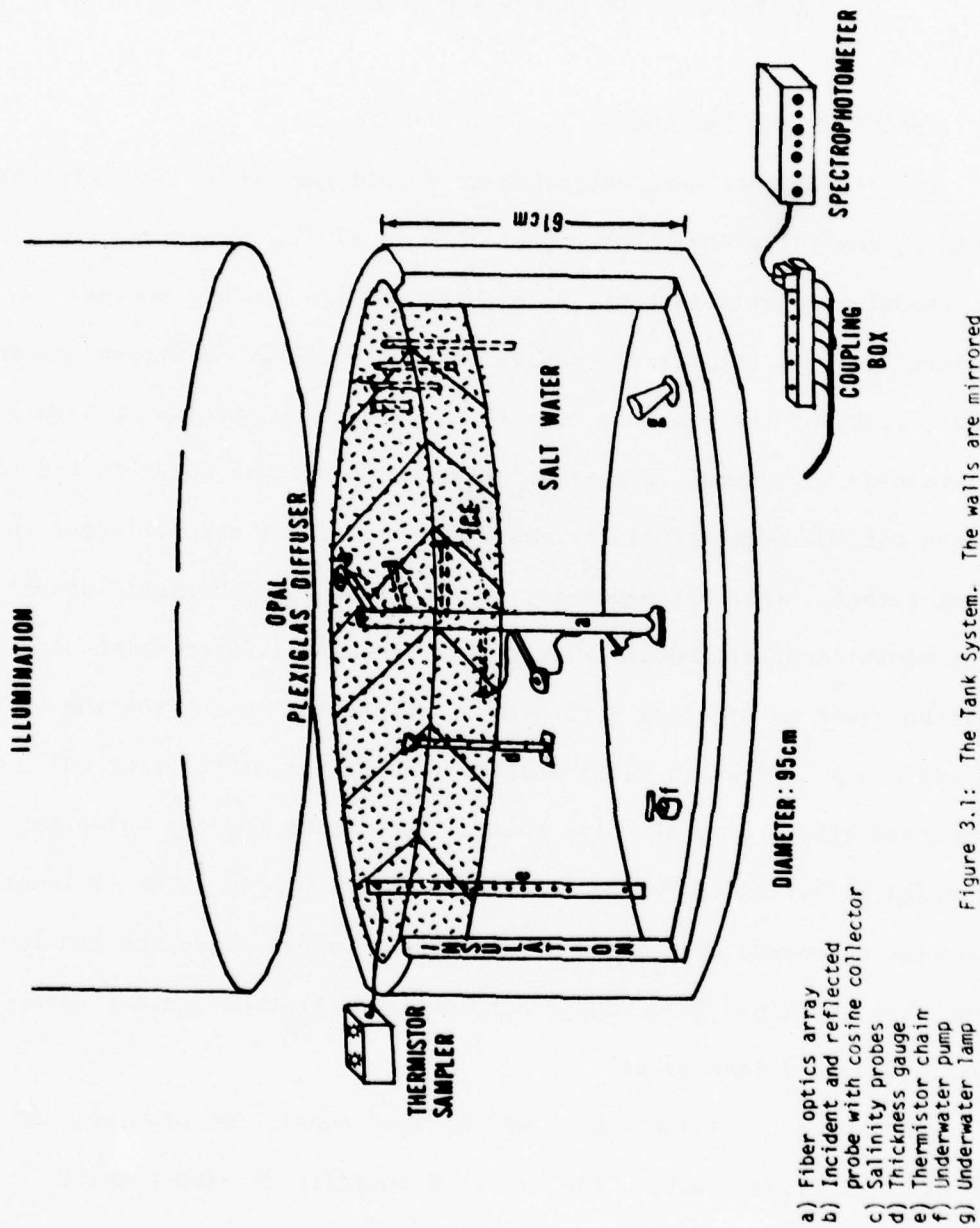


Figure 3.1: The Tank System. The walls are mirrored and the bottom is black. The cylindrical tank is housed inside a square holding tank which provides additional regulation and protection against leaks.

triangle (Figure 3.2a). This configuration provided maximum illumination with minimum surface melting. A sheet of opal plexiglas placed between the "sun" and the ice surface acted as a diffuser, creating lighting conditions similar to cloudy skies. An underwater lamp installed on the bottom of the tank enabled the ice to be viewed in transmitted light.

The profiling spectrophotometer described by Roulet *et al.* (1974) was used to measure spectral irradiances over the wavelength region 400 to 1000 nanometers. The key feature of this spectrophotometer was the use of fiber optics to transmit light from the interior of the medium to the instrument, allowing *in situ* optical measurements to be made. Glass fiber optics probes were selected for high transmission over the entire wavelength region of interest. The fiber optics probes were mounted on a central plexiglas column in a spiral array as shown in Figure 3.1. Typically six probes were used. An above surface probe was used for measurements of incident and reflected irradiances, while four probes frozen into the ice at depths of 3, 6, 10, and 19 cm and a sixth probe always below the ice at a depth of 33 cm, measured transmitted irradiances. A specially designed box (Figure 3.2b) coupled the fiber optics probes to the spectrophotometer. Tests were conducted to insure that the box allowed the probes to be coupled in a reproducible fashion. Optical data were recorded on tape using an analog to digital converter.

To relate the optical measurements to the physical state of the ice, measurements of ice thickness, temperature, and salinity were made.

Ice thickness was measured during the experiments using a thickness gauge consisting of plastic pipe (CPVC), .64 cm in diameter, 45.7 cm long, and graduated in intervals of .25 cm, with a flat plexiglas base.

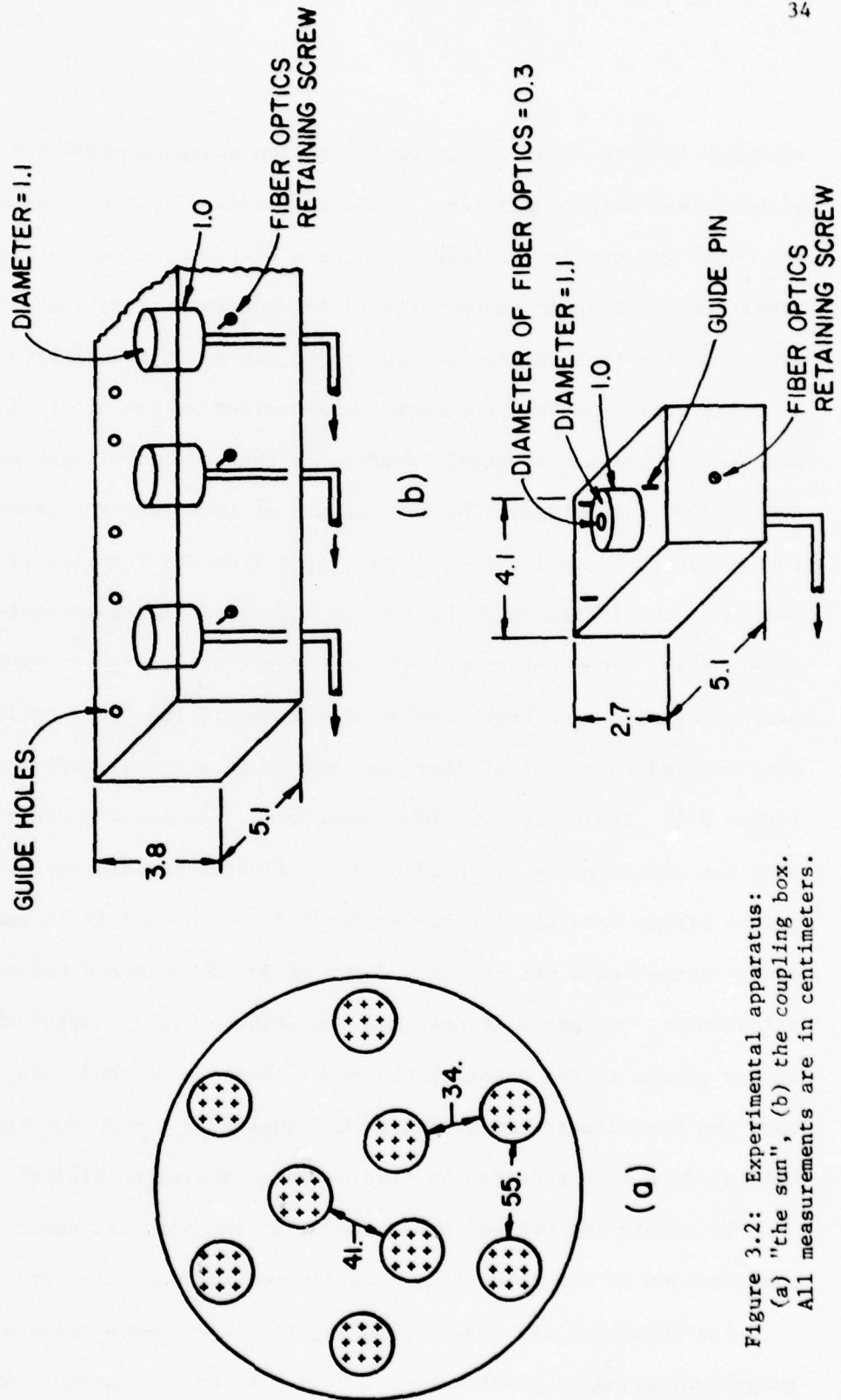


Figure 3.2: Experimental apparatus:
 (a) "the sun", (b) the coupling box.
 All measurements are in centimeters.

Frozen vertically into the ice, measurements were made by pulling the gauge upwards until the base reached the bottom of the ice.

A vertical chain of thermistors was used to obtain temperature data. Temperatures were usually recorded at 3 cm above the surface, at the surface, and at depths of 2, 4, 6, 8, 10, 12, 14, 16, 18, 20, 22, and 34 cm. The thermistors were potted in silastic on a plexiglas strip and painted with marine varnish to provide electrical insulation. Thermally insulating effects of the varnish were unimportant since ice temperature changes were slow compared to thermistor response time.

To determine salinity profiles several lengths of CPVC pipe, 1.13 cm in diameter, were frozen into the ice. When a salinity profile was needed a tube was removed from the ice providing an ice core which was then cut into 2 cm sections. After the sections melted the salinity was measured using an ENDECO Type 102 optical salinometer.

After building and assembling the pieces of apparatus a series of tests were conducted to check the accuracy of the equipment and eliminate design flaws. The accuracy of the thickness gauge and the salinity probes was checked. As a result of these tests two major additions to the system were made. A fan was added to enhance growth by providing air circulation and an underwater pump was used to circulate the water, thus retarding the growth of ice along the wall of the tank. With the tank system it was possible to grow ice 25 to 30 cm thick similar to that found in the Arctic, determine the state and structure of the ice, and make in situ optical measurements.

The early testing of the tank provided insights regarding methods of conducting successful experiments which were formalized into a

standard set of procedures used to perform the tank experiments. Before each experiment the tank was thoroughly cleaned, the water filtered through a Water Pic filter, and the NaCl and water mixed in an intermediate storage tank so that any residue was not added to the tank. As is frequently done in laboratory experiments [Weeks (1962), Martin (1974), Eide and Martin (1975), Davis and Munis (1973), Lane (1975), and others] a NaCl solution was substituted for seawater. The cold temperatures during the experiments tended to cause wear and breakage of the equipment. In particular, fiber optics probes, thermistors, the thickness gauge, and the tank's waterproofing were checked frequently for necessary repairs or replacements. Due to their short life, new light bulbs were installed in the "sun" at the beginning of every experiment.

Each experiment consisted of two parts, a growth phase where the air temperature of the cold room was held constant and a warming phase where the air temperature was changed and the ice allowed to attain a linear temperature profile at the new air temperature. A group of optical and physical measurements for a given ice thickness and air temperature is referred to as a site. For example, a typical experiment has a growth phase consisting of eight sites for ice thicknesses between 0 and 26 cm and a warming phase with sites at air temperatures of -10°C and 0°C . The last site of the growth phase is also included in the warming phase. Optical measurements consist of incident, reflected, and transmitted irradiances; while ice thickness, salinity, temperature, and photographs constitute the physical measurements. Table 3.1 outlines the procedure involved for a particular site.

Table 3.1
Experimental Procedures

STEP	TIME (minutes)	ACTION
1	0	Turn on electronics, warm up.
2	20	Measure thermistor resistances.
3	25	Turn on sun.
4	30	Measure spectrophotometer background signal.
5	32	Make optical measurements of incident, reflected, and several transmitted intensities.
6	40	Measure spectrophotometer background signal.
7	41	Turn off sun and electronics.
8	45	Measure thickness.
9	50	Remove salinity core, section, and allow to melt for later use.
10	60	Photograph ice surface.

At the end of the growth phase, a core was removed for photographic analysis of the ice structure. A vertical slab approximately two centimeters thick was prepared and photographed in both reflected and transmitted light. A close-up profile was made using transmitted light. To display the crystal structure crossed-polaroid pictures of both horizontal and vertical thin sections were taken and the remainder of the ice core was stored for reference.

Though primarily influenced by the air temperature during freezing, the duration of an experiment also depended on such factors as the length of the warming phase and the amount of breakage occurring. Typically, experiments could be initiated at four week intervals.

3.2 DATA REDUCTION

3.2.1 Optical Measurements

The reduction and analysis of the optical information, as outlined in Figure 3.3, was a multistep procedure. Raw data, consisting of spectrophotometer slit positions and irradiances were recorded on a cassette tape recorder. The tape was read through a software program on a Raytheon 704 computer which encoded the information generating a CDC compatible magnetic tape. The reduction continued on a CDC 6400 computer where the data were partitioned into individual scans, consisting of about 230 ordered pairs of wavelength and irradiance values over the wavelength interval 400 to 1000 nm. Repeated scans for a given probe and site were then averaged together and transposed onto a standard wavelength grid.

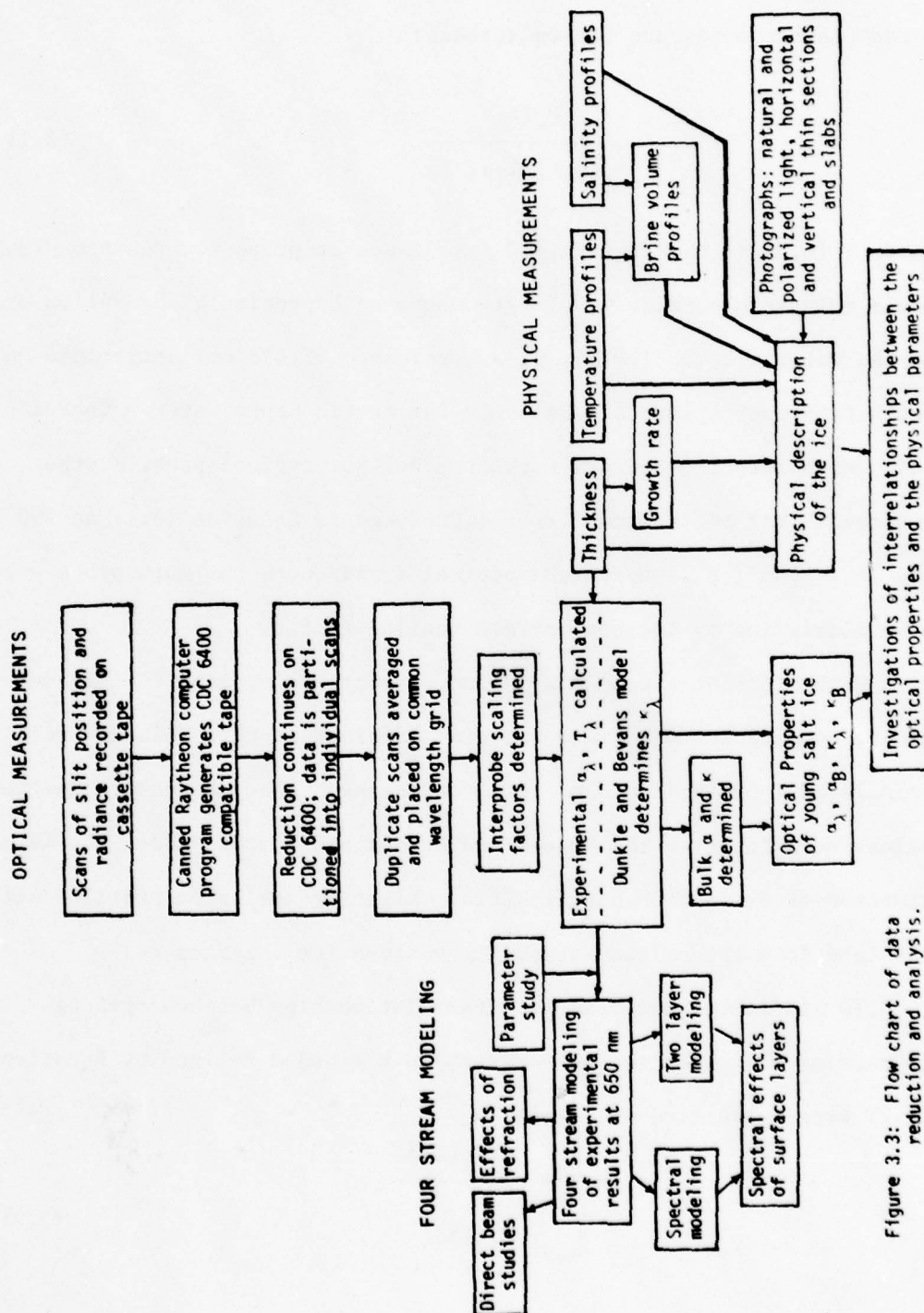


Figure 3.3: Flow chart of data reduction and analysis.

Since several fiber optics probes were used concurrently, it was necessary to determine the relative sensitivity of each probe. Scaling factors S_n were selected for each probe using data from the no ice (open water) measurements and the relationship

$$S_n = \frac{F_0(\lambda)}{F_{\downarrow}(n, \lambda)[1 - \alpha(\lambda)]} \quad (3.1)$$

where $F_{\downarrow}(n, \lambda)$ is the transmitted irradiance at probe n . Equation (3.1) could only be used at a wavelength where no appreciable absorption occurs in the water. Smith (1973), at a wavelength of 490 nm, determined an extinction coefficient of $.0444 \text{ m}^{-1}$ for Arctic Upper Water. Substituting this value into the Bouguer-Lambert model for typical probe depths indicated that the maximum error introduced by Equation (3.1) at 490 nm was less than 1.5%. Measured spectral irradiances for each probe were then multiplied by the appropriate scaling factor.

With scans on a common grid and appropriate scaling factors determined, comparisons were made between different depths. Albedos were calculated from incident and reflected scans. Albedos and transmitted values were input to the Dunkle and Bevans photometric model for determination of extinction coefficients. Light transmission profiles were obtained from transmitted scans for various ice thicknesses.

To aid in the analysis of interrelationships between optical properties and other ice parameters, bulk albedos defined by Equation (3.2) were calculated

$$\alpha_B = \frac{\int_{400}^{1000} \alpha_{\lambda} F_0(\lambda) d\lambda}{\int_{400}^{1000} F_0(\lambda) d\lambda} \quad (3.2)$$

To obtain the necessary spectral albedos, experimental results over the interval 500 to 1000 nm were smoothed using a high order polynomial fit. Due to the typically small signal to noise ratio for wavelengths less than 500 nm, experimental values were discarded and the value at 500 nm assumed to apply to the entire 400 to 500 nm region. This approximation was based on the results of Grenfell and Maykut (1978) which showed $a(\lambda)$ to be fairly constant below 500 nm. Values of $F_0(\lambda)$ for both clear and cloudy skies were obtained from Sauberer and Durnhirm (1958) and Cast (1960) and are plotted in Figure 3.4.

3.2.2 Physical Measurements

Ice temperatures, salinities, and thicknesses were routinely measured during the experiments. Thermistor readings of resistance were converted into temperatures. Using temperature and salinity profile data as input brine volumes were calculated from the expression

$$v_B = -.055 \frac{S}{T} \quad , \quad (3.3)$$

where v_B is brine volume, S is the salinity in parts per thousand, and T is the temperature in degrees Centigrade.

Ice thicknesses were plotted as a function of time (t) and Equation (3.4) was used to determine point to point growth rates (f)

$$f = \frac{H_i - H_{i-1}}{t_i - t_{i-1}} \quad . \quad (3.4)$$

Theoretical thicknesses and growth rates were calculated using a Stefan

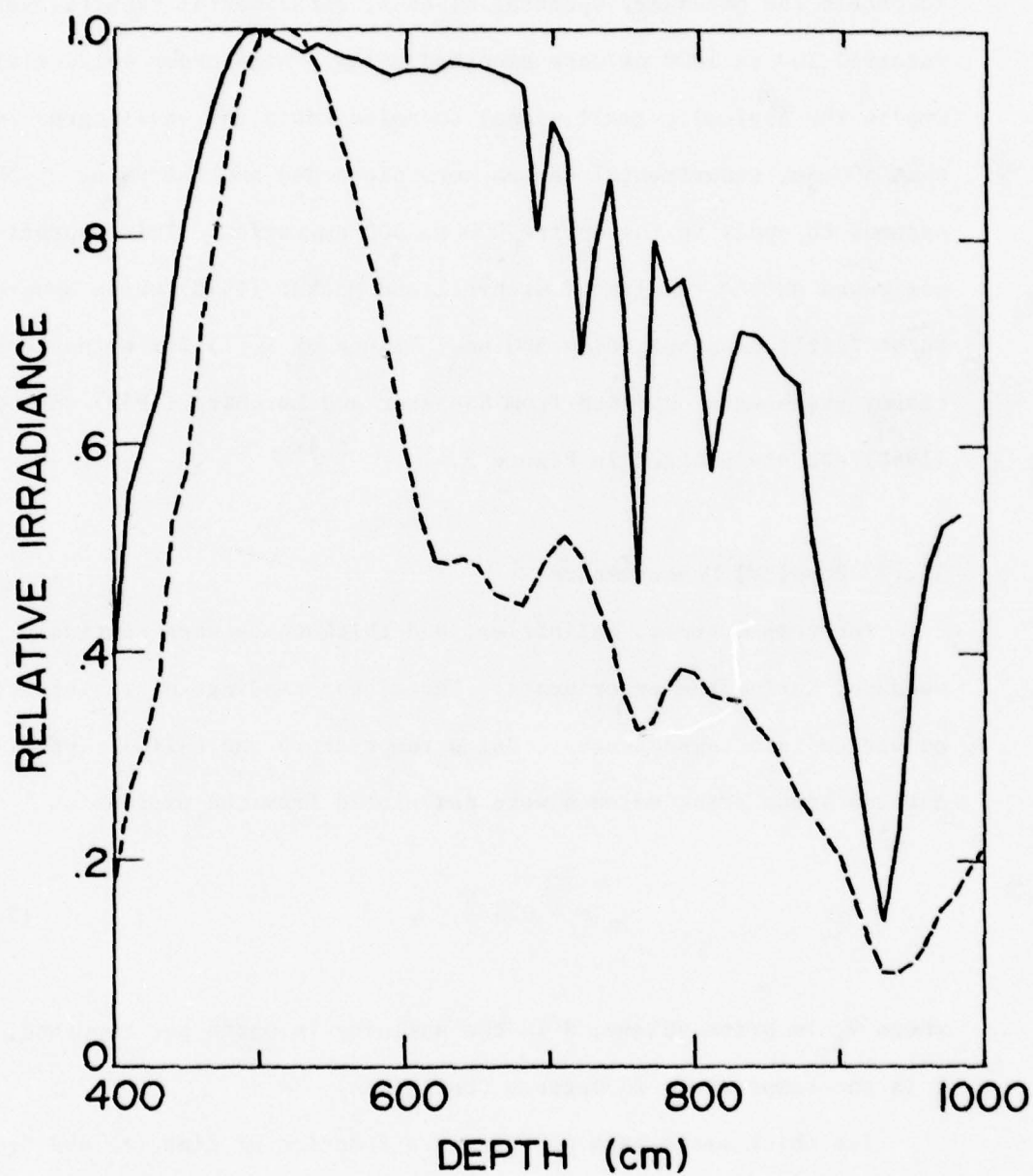


Figure 3.4: Normalized incident radiation under: ————clear skies (Sauberer and Dirmhirn, 1958), and -----cloudy skies (Gast, 1960).

growth model, which had been modified to use empirical formulas for the heat of fusion and conductivity of sea ice, and compared to measured values.

3.3 ERROR ANALYSIS

3.3.1 Optical Measurements

The optical measurements contained three potentially significant sources of error: temporal and spatial variation in illumination, instrumental noise, and the bandpass of the instrument. In designing and testing the experimental configuration several steps were taken to minimize errors caused by the system of illumination. The sun was enlarged from six bulbs to nine, thus providing an incident radiation field of greater areal uniformity. In early tank testing the incident radiation was measured at the beginning and end of each set of readings to examine the variability of the lighting. It was determined that there was no appreciable change in incident irradiance during a set of measurements, but that the variation between sites was large enough to necessitate an incident measurement for each site.

The electronic noise level was independent of wavelength and equal to ± 2.5 mV for the more sensitive instrument setting and ± 1 mV for the less sensitive. However, since this noise level affected a signal which varied in magnitude with wavelength, the percent error had a decided wavelength dependence. Figure 3.5 illustrates the resultant ranges in calculated albedos for representative cases. Due to low signal levels the uncertainty between 400 and 450 nm was so extreme as to preclude any meaningful interpretation of the data.

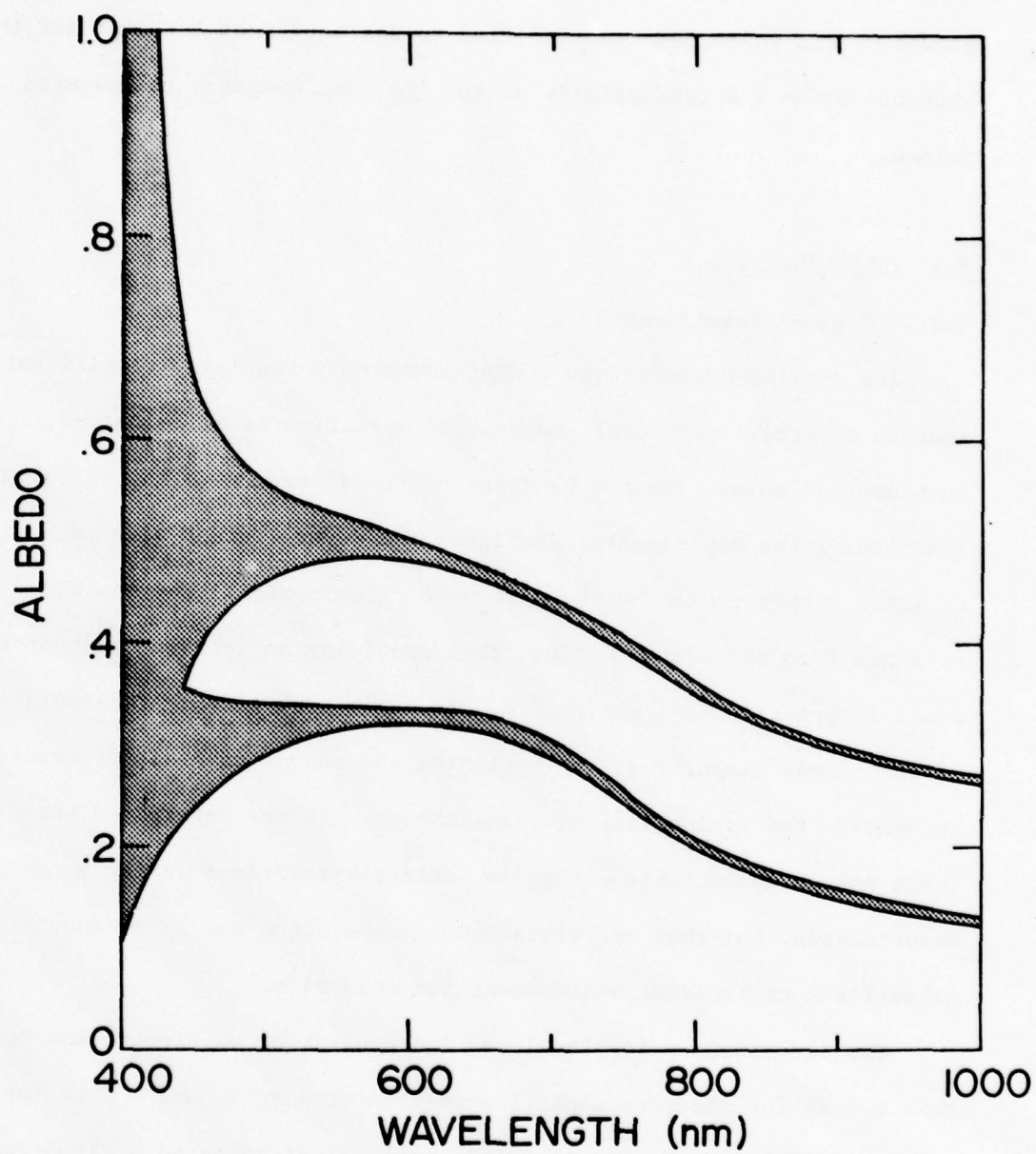


Figure 3.5: Range of uncertainty in albedo due to instrumental noise: The lower curve is ice 11.7 cm thick at an air temperature of -10°C and the upper curve is ice 14.6 cm thick at an air temperature of -30°C .

Spectral errors were introduced at long wavelengths by the large bandpass of the instrument. This bandpass error was manifested as an apparent decrease in the wavelength dependence of a property. The spectrophotometer, using a glass prism, had less resolving power in the red portion of the spectrum than in the blue. Also, as was shown in Figure 1.1, previous research indicated an accelerating increase in extinction coefficient with wavelength for sea ice. Thus, the loss of spectral resolution, while not important at shorter wavelengths, became critical at longer. Deconvolution techniques were used in an attempt to increase spectral resolution. However, deconvolution magnified small signal variations into large oscillations (Figure 3.6) yielding unrealistic values and making it inapplicable in this experiment. Since its spectral dependence was weaker, albedo was not as strongly influenced by this error as extinction coefficient. Because of the bandpass broadening, extinction coefficients calculated for wavelengths greater than 800 nm were not reported.

3.3.2 Physical Measurements

Thicknesses and the depths of the fiber optics probes were measured with an accuracy of ± 1.5 mm. There was no preferential growth of ice along the thickness gauge. Determining salinity profiles the error in reading the optical salinometer was $\pm .1$ ‰ and the sectioning was accurate to ± 1 mm in position. Additional uncertainty in salinity was caused by the small sample volume. Because of brine drainage, salinity measurements from the bottom section of the core were erroneously small. Thermistor positions were known to ± 1 mm while the error in temperature varied from .2 to .4°C as illustrated in Figure 3.7.

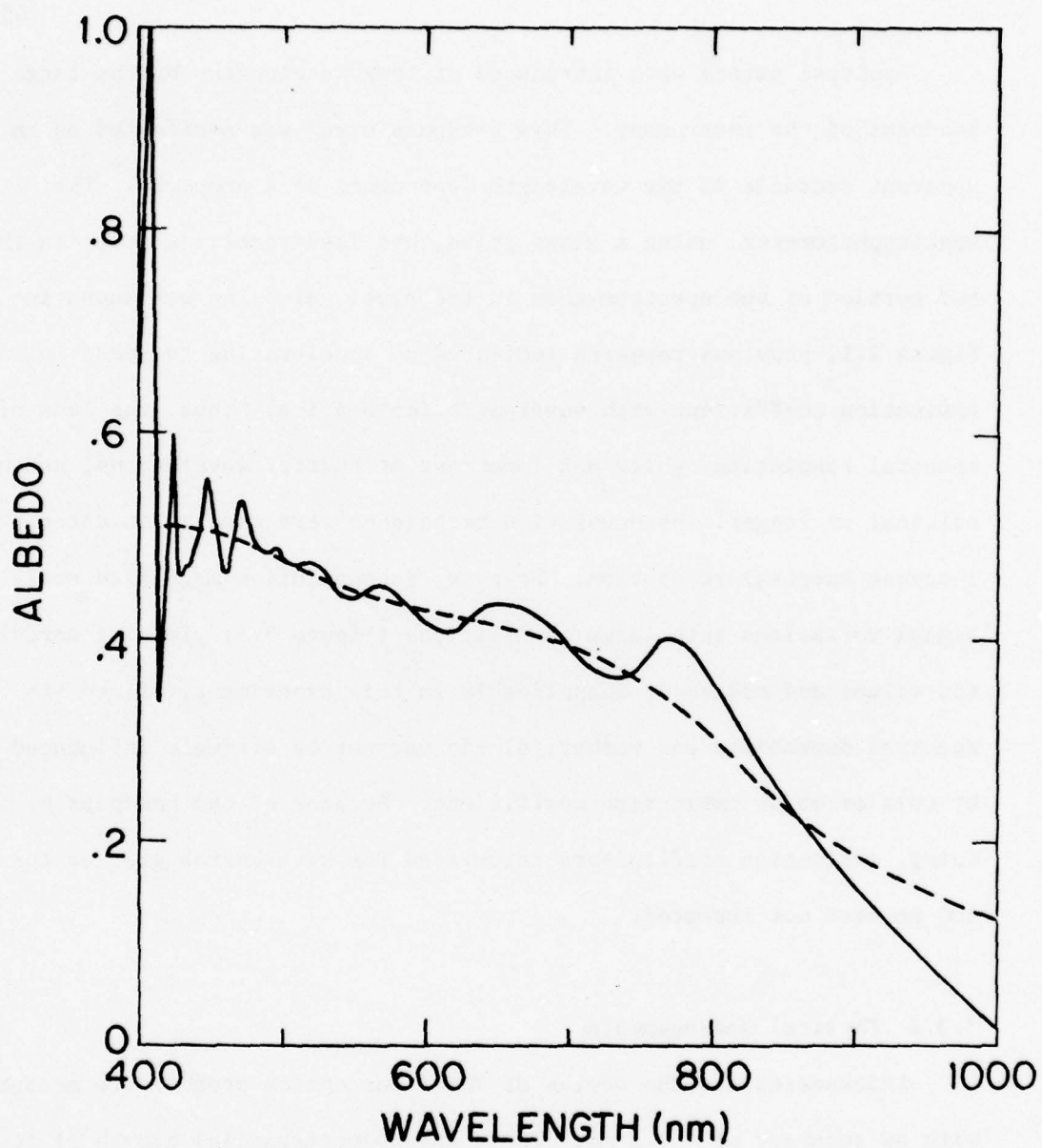


Figure 3.6: Effects of deconvolution on albedo: (-----) before deconvolution and (————) after deconvolution.

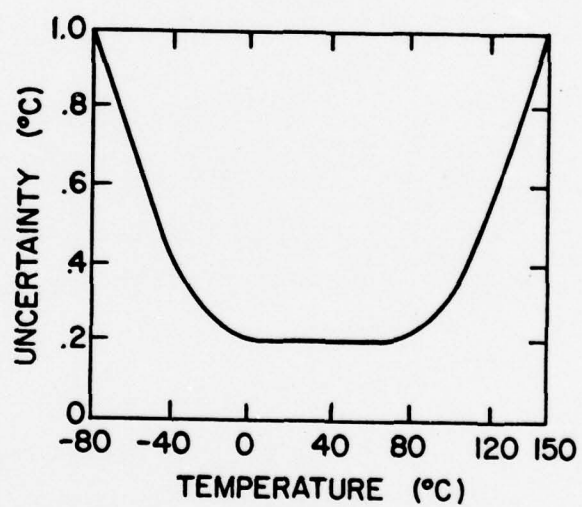


Figure 3.7: Thermistor uncertainty.

CHAPTER FOUR

EXPERIMENTAL RESULTS

4.1 INTRODUCTION

A series of 18 experiments were performed using the apparatus and methods discussed in Chapter Three. Six of these occurred during the testing phase, yielding primarily information regarding improvements to the experimental system. After the testing was completed, it was determined that eight cases would best satisfy the experimental objectives. Due to assorted electronic failures, it was necessary to perform twelve experiments to completely fulfill these data requirements.

Experiments were conducted for different water salinities and over a range of air temperatures. On the basis of water salinity, experiments were grouped into three categories; fresh water (Experiments 1 and 2), salinity (31 ‰) comparable to Arctic Ocean water (3-6), and intermediate (16 ‰) salinity water (7, 8). Salt ice was grown at air temperatures of -10, -20, -30, and -37°C. The environmental conditions for the experiments are summarized in Table 4.1 with more detailed information regarding individual sites displayed in Table 4.2.

4.2 SELECTED RESULTS

4.2.1 Fresh Ice Results

During the first two experiments fresh ice, grown at an air temperature of -15°C, was investigated to compare to the salt ice cases and to examine the influence of air bubbles. Experiments 1 and 2 exhibited a range of bubble conditions including bubble free ice, spherical bubbles, and long cylindrical vertically oriented bubbles.

Table 4.1
Summary of Tank Experiments

Experiment Number	Water Salinity (‰)	Air Temperature During Freezing (°C)	Probe Depths (cm)	Number of Sites Growth: Warming
1	0	-15	9.7, 17.7, 18.2 18.2, 33.0	8:0
2	0	-15	3.0, 10.7, 19.0 34.0	5:0
3	30.6	-10	3.1, 6.9, 11.0 19.3, 34.5	7:2
4	30.2	-20	2.5, 6.3, 10.5 18.5, 33.6	7:3
5	30.8	-30	3.2, 6.9, 11.0 19.4, 34.4	6:2
6	31.1	-37	3.0, 6.4, 10.9 19.0, 34.1	7:2
7	16.3	-10	3.2, 6.7, 11.0 19.9, 34.5	7:3
8	16.5	-20	3.0, 6.4, 10.9, 20.3, 34.3	7:2

Table 4.2
Ice Thickness (cm) and Air Temperature (°C)
for Experimental Sites

		Experiment							
Site		1	2	3	4	5	6	7	8
	1	Open Water	Open Water	Open Water	Open Water	Open Water	Open Water	Open Water	Open Water
	2	2.54 -15	9.2 -15	4.3 -10	2.0 -20	3.2 -30	3.8 -32	4.5 -20	3.6 -10
	3	4.4 -15	12.5 -15	7.6 -10	4.6 -20	11.2 -30	7.6 -32	9.3 -20	7.9 -10
	4	6.4 -15	18.2 -15	11.7 -10	7.6 -20	14.6 -30	14.5 -33	12.1 -20	11.6 -10
	5	8.9 -15	22.4 -15	18.5 -10	11.7 -20	19.6 -30	17.5 -36	15.4 -20	14.2 -10
	6	10.4 -15	—	21.1 -10	17.8 -20	23.9 -30	23.5 -37	19.3 -20	19.6 -10
	7	12.2 -15	—	27.2 -10	21.6 -20	29.0 0	26.0 -37	22.6 -20	23.0 -10
	8	16.8 -15	—	28.4 0	25.7 -16	29.2 -20	28.0 -22	23.8 0	23.4 0
	9	—	—	25.9 -5	26.2 -10	—	29.0 -2	23.8 -20	23.4 -10
	10	—	—	—	27.9 0	—	—	—	23.4 -20

The top seven centimeters of ice grown in Experiment 1 were virtually bubble free. Bubbles then appeared and gradually increased in number between 7 and 12 cm, with a high density of bubbles being present from 12 cm to the bottom of the ice. The bubbles were predominately spherical with a few being cylindrical.

Measurements across the bubble free region indicated that within the limits of error bubble free ice and water are optically indistinguishable. This is in agreement with other reported measurements of extinction coefficient for pure ice and water (Goodrich, 1970). Based on the results of previous researchers, transmission differences, for 7 cm thick ice, between the two cases are calculated to be no greater than 1.5% for wavelengths between 400 and 800 nm; a difference less than the experimental error levels.

In the bubbly region of Experiment 1 albedo evidenced a slight increase with thickness. Figure 4.1 illustrates spectral albedos measured for fresh ice of thickness 6.4, 12.2, and 16.8 cm. While the albedo of bubble free ice (Curve 1) is the same as that for water, there is an increase as the ice thickens (Curves 2 and 3). The increasing density of air bubbles in the ice results in greater scattering and a larger albedo. There was no noticeable difference in extinction coefficient between these cases. However, the ability to measure variations in extinction coefficient is less precise due to additional errors introduced by the inter-probe scaling factors.

Experiment 2 exhibited a very different type of bubble structure with vertical strings of small bubbles and long, thin, vertically oriented cylindrical bubbles prevalent. The diameter of the cylinders was roughly .2 mm with lengths ranging from 2 to 40 mm; 7 mm being

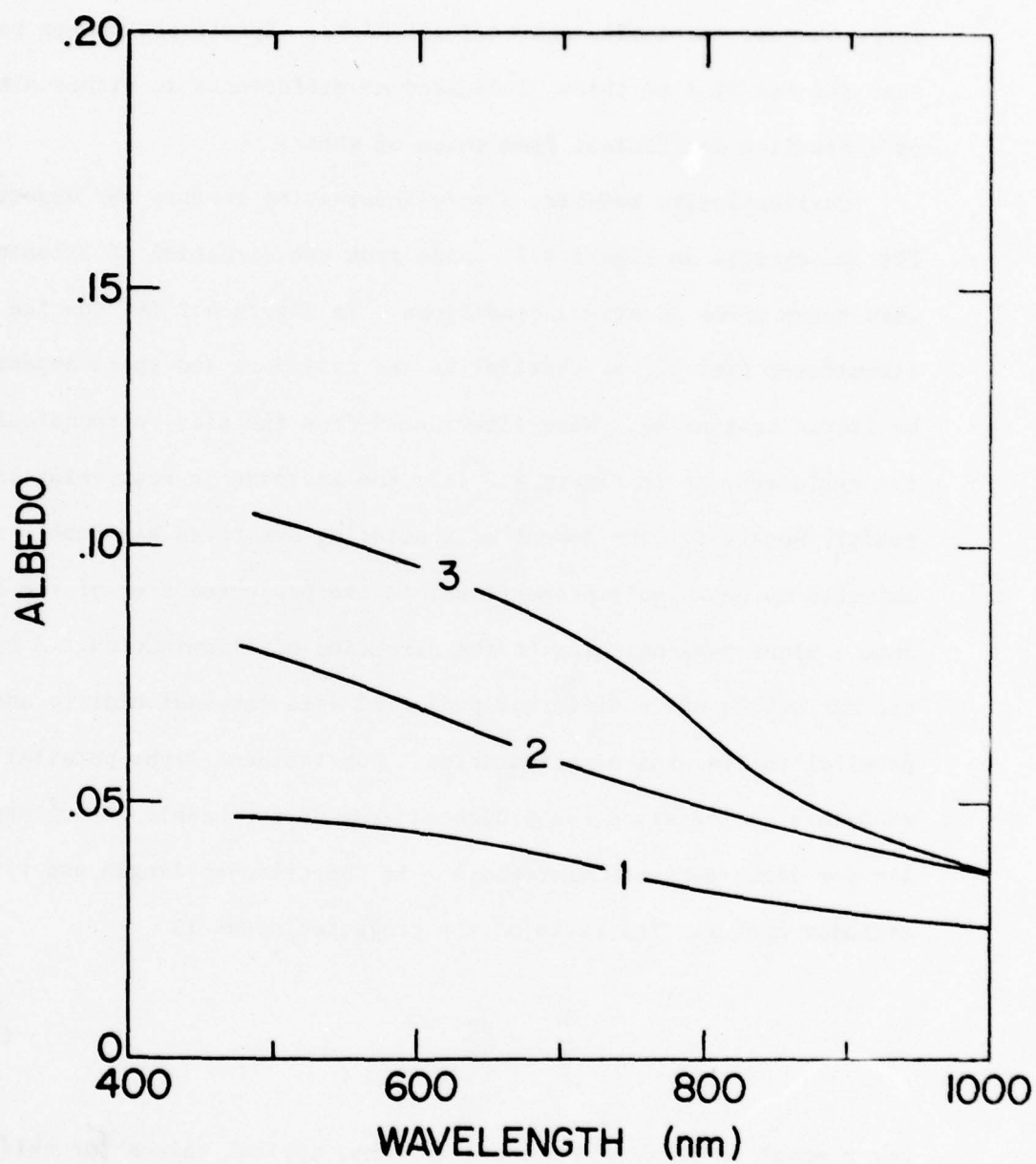


Figure 4.1: Spectral albedos for fresh ice of thickness:
(1) 6.4 cm; (2) 12.2 cm; and (3) 16.8 cm.

typical. In many instances closer inspection revealed that what appeared to be one cylindrical bubble was a linear array of many small bubbles. However, in a general sense, the bubbles can be described as long, narrow, vertically oriented cylinders. Spectrophotometer results, even for ice 22.4 cm thick, indicated no differences in either albedo or extinction coefficient from those of water.

Qualitatively, however, a very interesting feature was observed. The photographs in Figure 4.2, aside from the direction of illumination, were taken under identical conditions. In Figure 4.2 (A) the ice is illuminated from above, parallel to the cylinders and there appears to be little scattering. When illuminated from the side, perpendicular to the cylinders, as in Figure 4.2 (B), the increase in scattering is readily apparent. The amount of scattering due to an air bubble can be expected to be roughly proportional to the projected area of the bubble onto a plane perpendicular to the direction of illumination. A cylindrical air bubble has a different projected area perpendicular to and parallel to its axis of orientation. For incident light parallel to the cylinders' orientation the projected area of the bubble is πr^2 and is $2\ell r$ for light perpendicular where ℓ is the cylinder length and r is the cylinder radius. The ratio of the projected areas is

$$\frac{A_{\perp}}{A_{\parallel}} = \frac{\pi r}{2\ell} \quad (4.1)$$

For r equal to .1 mm and ℓ equal to 7 mm, typical values for this experiment, A_{\perp}/A_{\parallel} is .0225, implying that the scattering should be on the order of 45 times greater for the perpendicular case. Further quantitative investigations of this phenomena are suggested in Chapter Six.

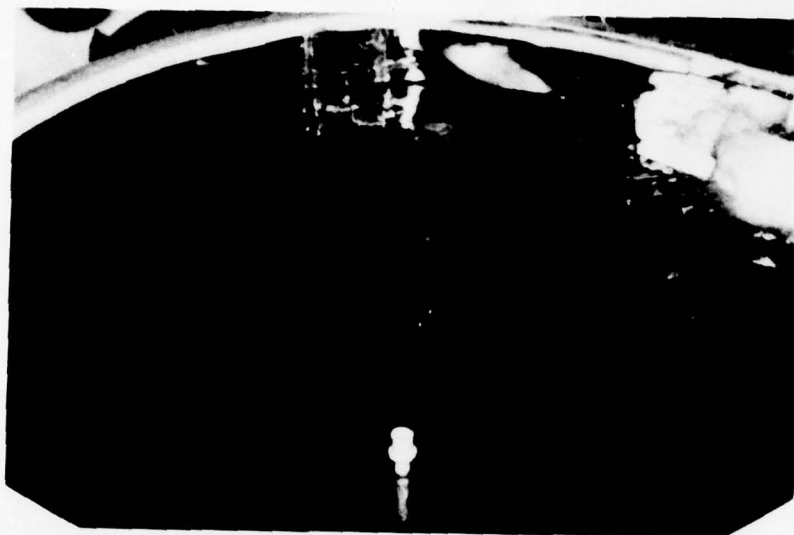
A**B**

Figure 4.2: Scattering by cylindrical bubbles in fresh ice:
(A) illumination parallel to cylinders, and (B) illumination perpendicular.

4.2.2 Salt Ice Results: Experiment 5

Experiments 3 through 6 are designed to determine the optical properties of young thin salt ice under a range of conditions. To avoid a tedious itemizing of data, only the results from one representative experiment, Experiment 5, are discussed in detail. Results from the remaining experiments are summarized in Appendix A.

The initial water salinity in Experiment 5 was 30.8 ‰. During the growth phase, the air temperature was held at -30°C . Measurements were made at ice thicknesses of 0.0, 3.2, 7.6, 14.6, 19.6, and 23.9 cm. After completing the growth phase the air temperature was raised to -2°C and measurements were taken after allowing sufficient time for the ice to achieve a linear temperature gradient. For the final site the air temperature was lowered to -20°C and the process repeated. Figures 4.3 and 4.4 display temperature and salinity profiles recorded in conjunction with the optical measurements. Temperature profiles, within thermistor error limits, were linear. The ice surface temperature was always warmer than the air temperature of -30°C , though approached it as the ice grew thicker.

The ice salinities were quite high with the profiles exhibiting considerable scatter. The profiles, for the most part, did not exhibit the strongly c-shaped curve associated with field measurements of young sea ice. Since the amount of brine entrapped increases with growth rate, the salinity of young ice decreases from the surface downward until reaching the skeletal growth layer at the bottom where due to the porous structure, the salinity again increases. However, in the experiments the salinity decrease over the middle region was not as pronounced

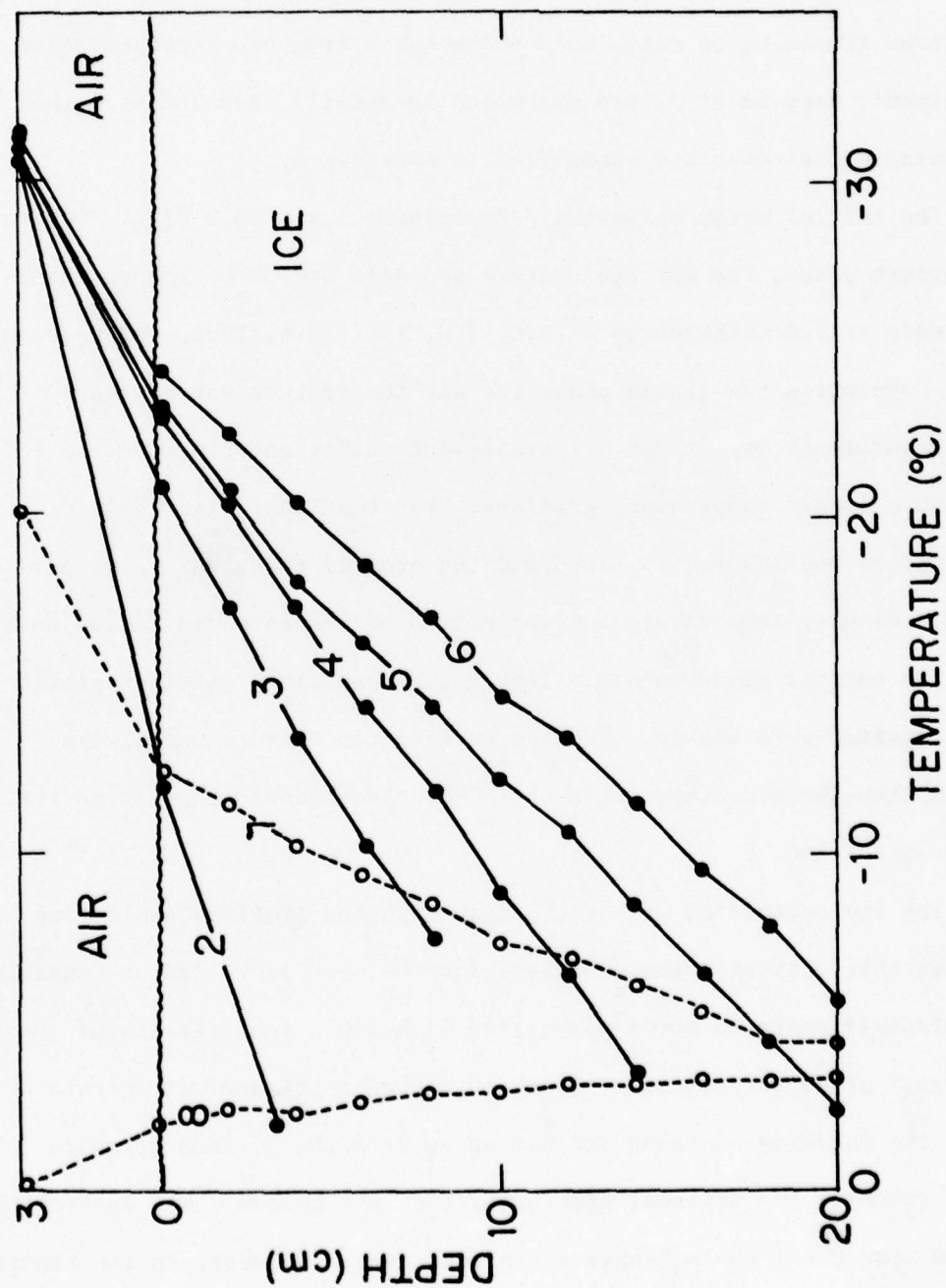


Figure 4.3: Temperature profiles for Experiment 5, Sites 2-8; — growth phase, — warming phase. The ice thicknesses were: (2) 3.2 cm; (3) 7.6 cm; (4) 14.6 cm; (5) 19.6 cm; (6) 23.9 cm; (7) 29.0 cm; and (8) 29.2 cm.

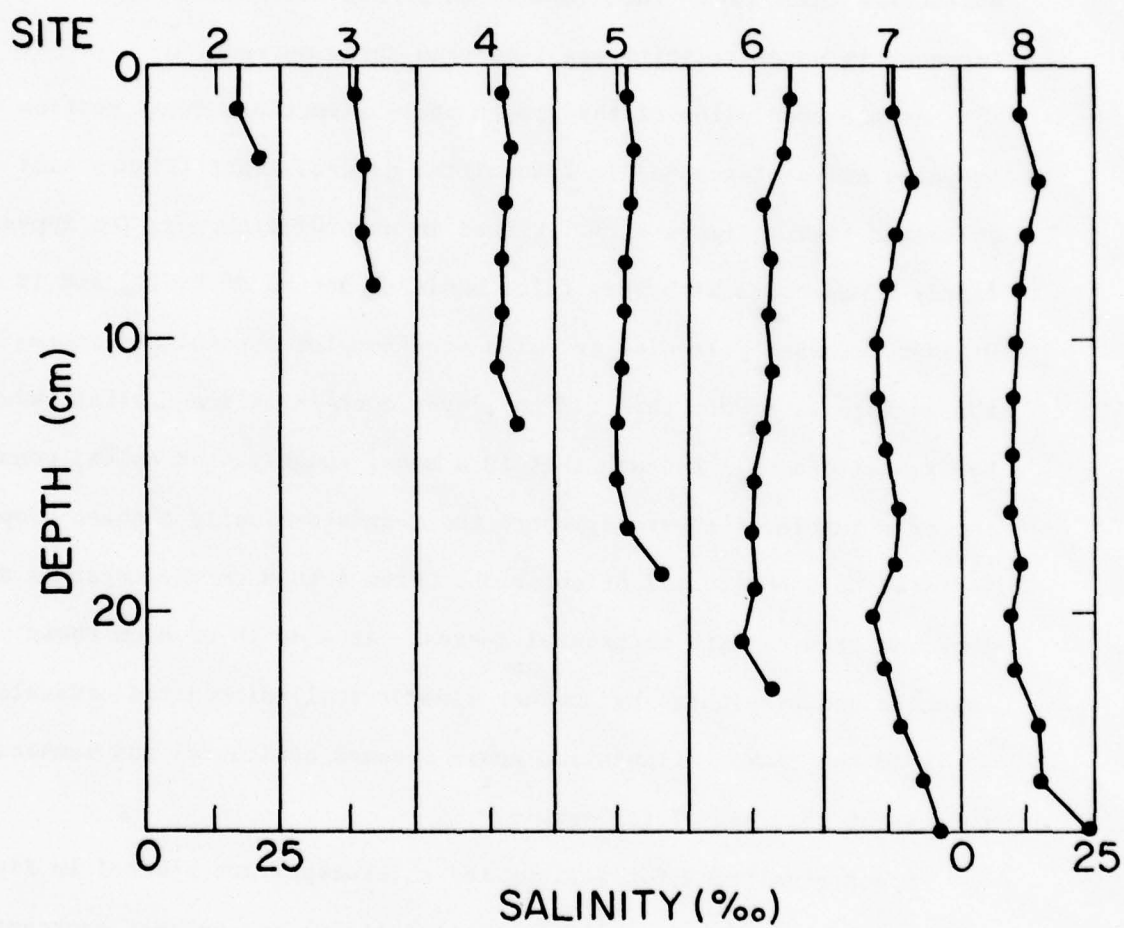


Figure 4.4: Salinity profiles for Experiment 5. The numbers correspond to the same cases discussed in Figure 4.3. The scale is the same for each site.

since the decrease in growth rate was counterbalanced by an increase in water salinity.

Ice thickness as a function of time and the accompanying growth rates are displayed in Figure 4.5. The growth rate smoothly decreased as the ice thickened. The decrease in growth rate caused by the increase in water salinity was less than three percent.

At the conclusion of the growth phase a vertical cross section was prepared and photographed in transmitted natural light (Figure 4.6) and polarized light (Figure 4.7). Viewed in natural light the ice appears fairly homogeneous with very faint bands at depths of 9, 11, and 18 cm. However, crossed polaroids reveal a more complex crystal structure. At the surface is a very thin (.3 cm) layer containing ice crystals with horizontal c-axes. Beneath that is a zone, roughly 4 cm thick, consisting of a jumble of crystals, where the c-axis gradually changes from a vertical to a horizontal orientation. From 4 to 8 cm the crystals are long and ordered with horizontal c-axes. At a depth of 8 cm these crystals are terminated by another zone of small disordered crystals. At 11 cm the c-axis orientation again becomes horizontal and remains so throughout the rest of the sample.

Spectral albedos for various ice thicknesses are plotted in Figure 4.8. Albedos from 400 to 450 nm (dotted lines) are assumed constant. There is a pronounced increase in albedo as the ice becomes thicker. Plotted for comparison (dashed curve) are the albedos of thick, melting, multiyear white ice and melting, first-year blue ice (dots and dashes) taken from Grenfell and Maykut (1978). The albedo of the multi-year ice is similar to that for cold, growing ice only 23.9 cm thick. The increase in albedo with ice thickness is wavelength dependent, with

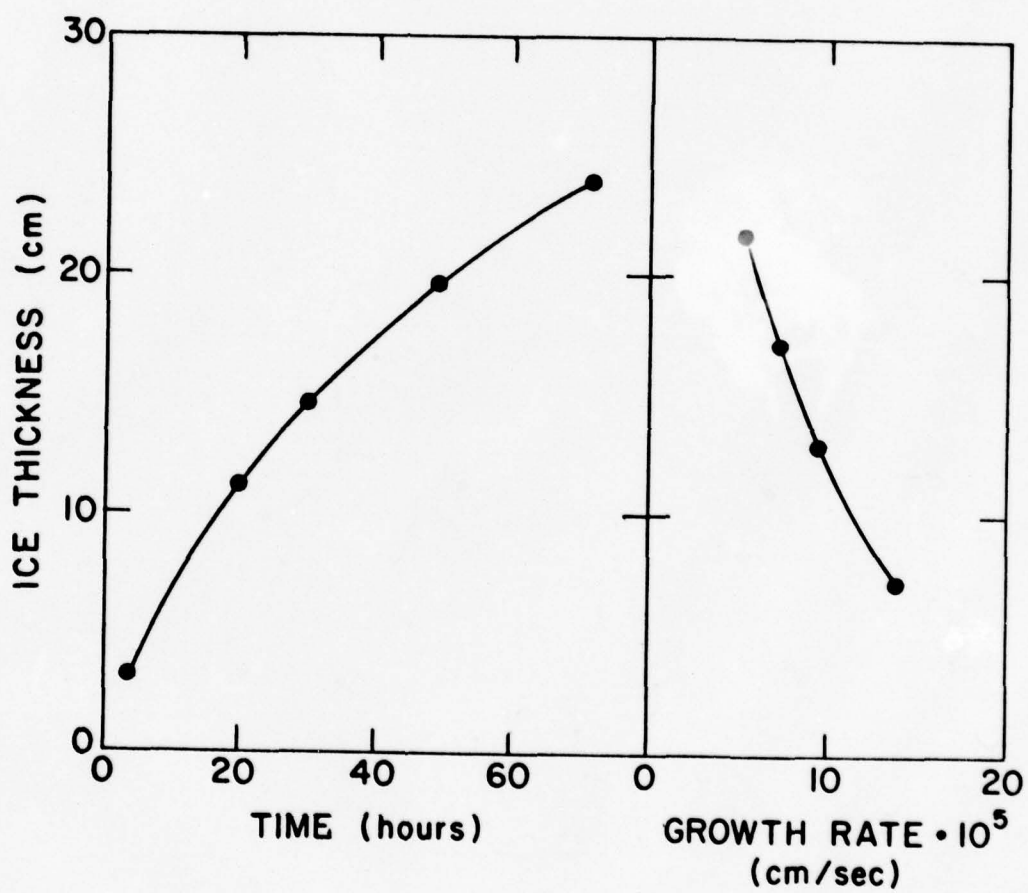


Figure 4.5: Ice growth data for Experiment 5.

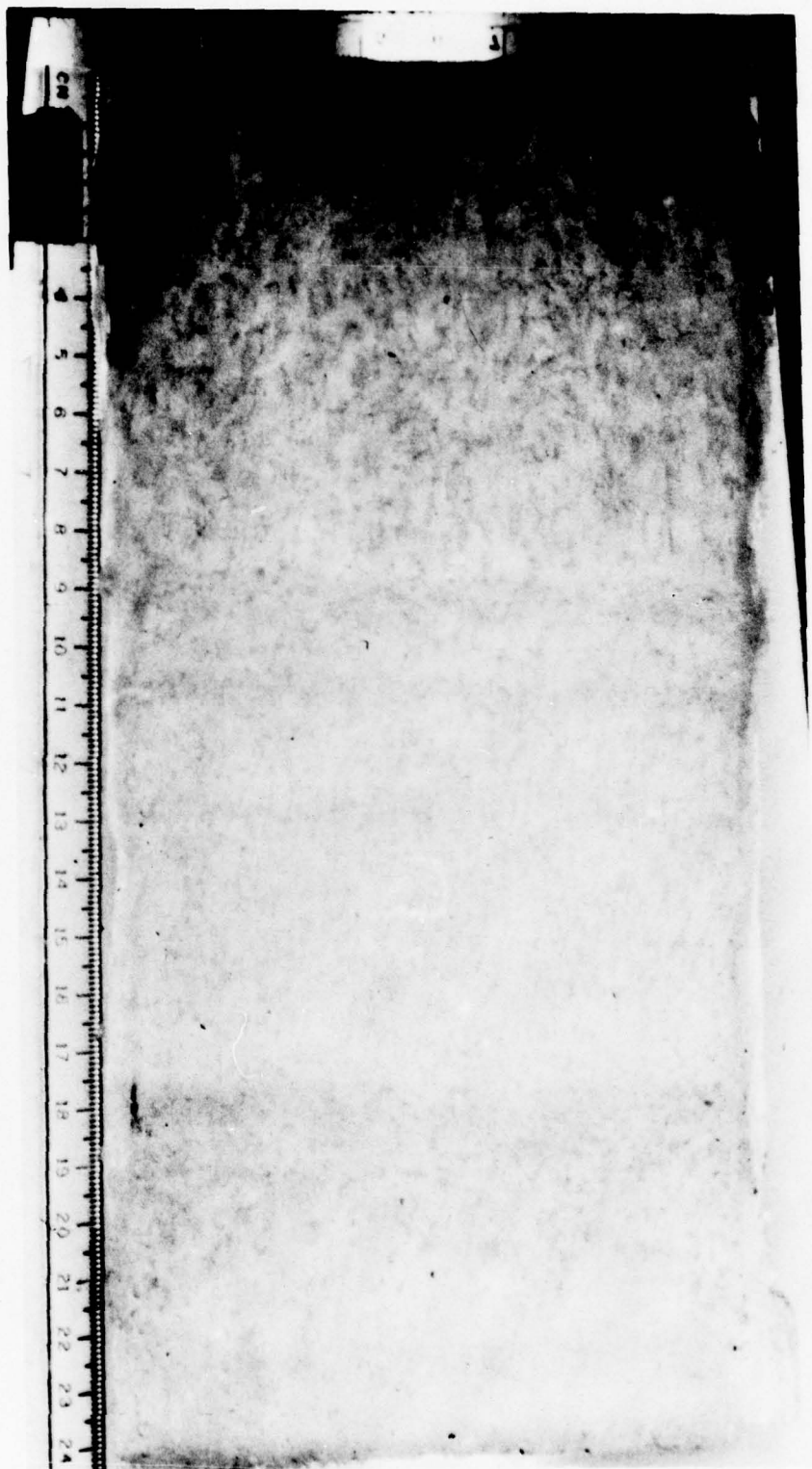


Figure 4.6: Ice slab from Experiment 5 photographed in transmitted light.



Figure 4.7: Ice slab from Experiment 5 photographed through crossed polaroids.

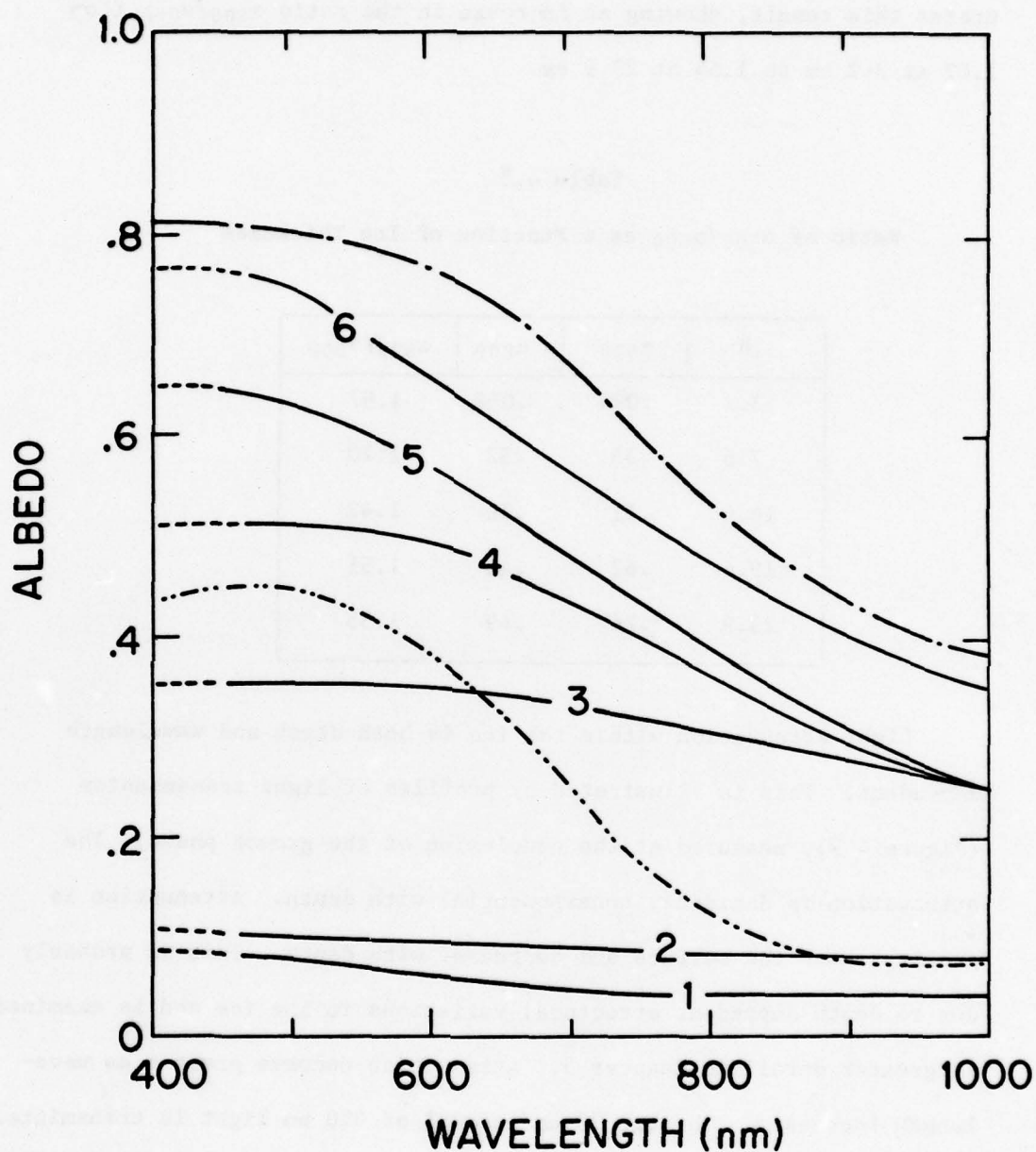


Figure 4.8: Spectral albedos for Experiment 5: (1) open water, cloudy sky bulk albedo of .07; (2) ice thickness of 3.2 cm, .09; (3) 7.6 cm, .31; (4) 14.6 cm, .44; (5) 19.6 cm, .53; (6) 23.9 cm, .63; - - - - - melting first-year blue ice (Grenfell and Maykut, 1978); and - - - - - melting multiyear white ice (Grenfell and Maykut, 1978).

a greater increase occurring at shorter wavelengths. Table 4.3 corroborates this result, showing an increase in the ratio $\alpha_{500}/\alpha_{800}$ from 1.07 at 3.2 cm to 1.55 at 23.9 cm.

Table 4.3

Ratio of $\alpha_{500}/\alpha_{800}$ as a Function of Ice Thickness

H	α_{500}	α_{800}	$\alpha_{500}/\alpha_{800}$
3.2	.094	.088	1.07
7.6	.35	.32	1.10
14.6	.51	.36	1.42
19.6	.62	.41	1.51
23.9	.76	.49	1.55

Light attenuation within the ice is both depth and wavelength dependent. This is illustrated by profiles of light transmission (Figure 4.9), measured at the conclusion of the growth phase. The attenuation is decidedly nonexponential with depth. Attenuation is greatest near the surface and decreases with depth. This is probably due to depth dependent structural variations in the ice and is examined in greater detail in Chapter 5. Attenuation becomes greater as wavelength increases. Through 20 cm ice 20% of 500 nm light is transmitted, while at 800 nm only 12% penetrates.

Incident, reflected, and transmitted spectral intensities were used in conjunction with the Dunkle and Bevans model to calculate spectral extinction coefficients. Values plotted in Figure 4.10 are for ice 23.9 cm thick, using measurements from a depth of 19.4 cm. Extinction

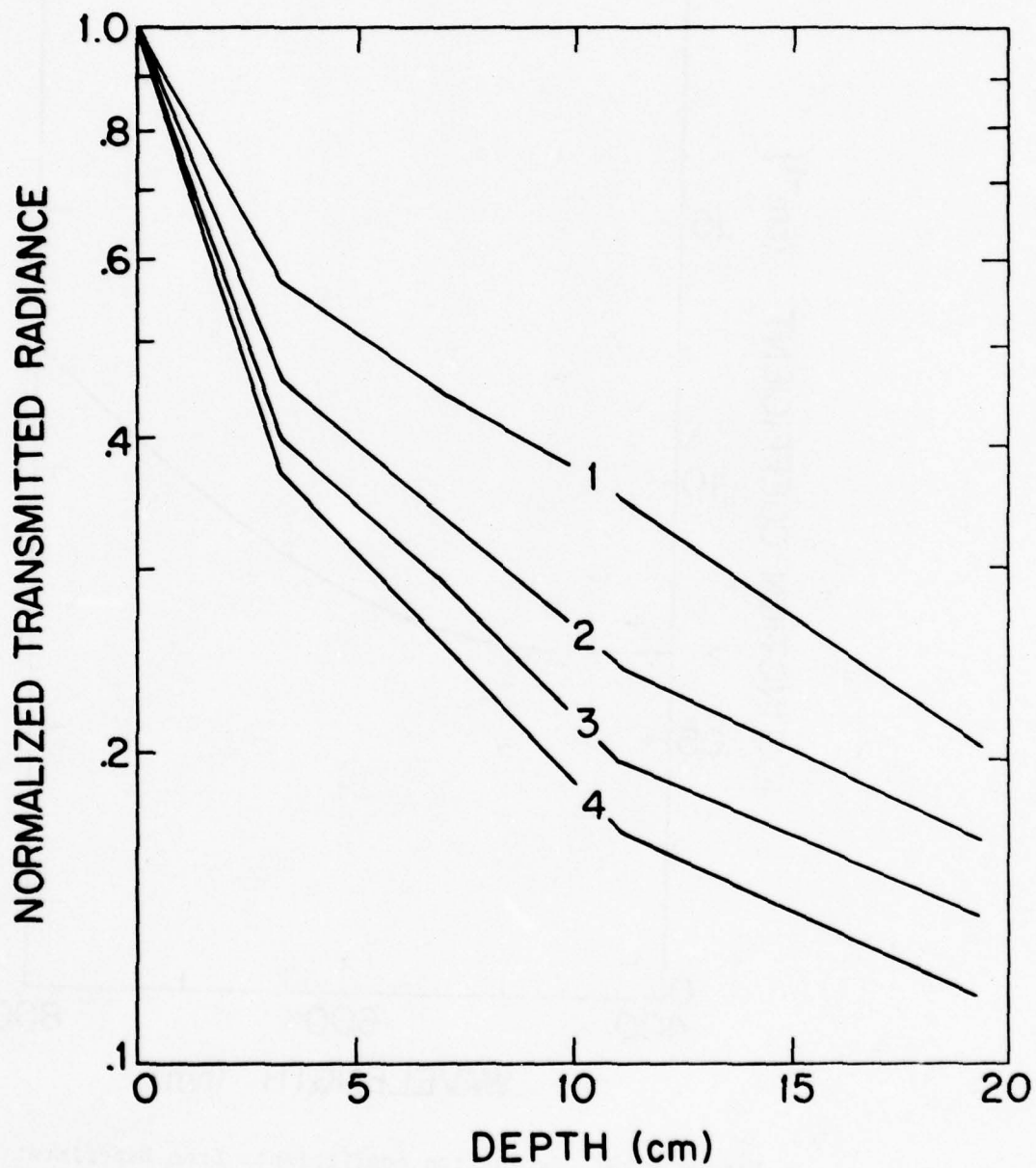


Figure 4.9: Spectral transmission profiles from Experiment 5 for 23.9 cm thick ice with an air temperature of -30°C : (1) 500 nm; (2) 600 nm; (3) 700 nm; and (4) 800 nm.

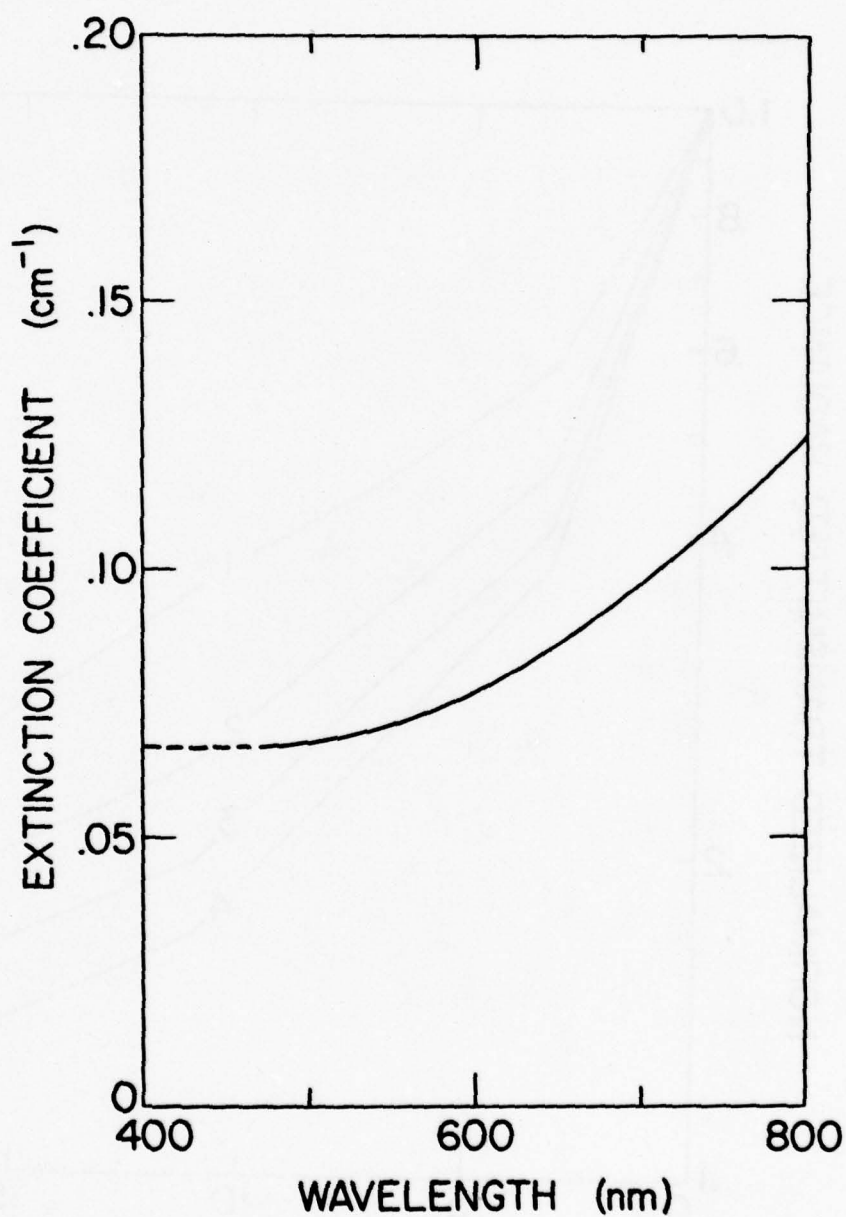


Figure 4.10: Extinction coefficients from Experiment 5
for ice 23.9 cm thick with an air temperature of -30°C.

exhibits a marked wavelength dependence, increasing slowly between 450 and 600 nm, then sharply from 600 to 800 nm. At 600 nm the value is only about 20% larger than at 500 nm, but by 800 nm it is 90% larger than the value at 500 nm.

Extinction coefficients at all wavelengths are considerably larger than previously reported results for thick ice. At 500 nm the extinction coefficient for this case is twice that measured in the surface granular layer of multiyear white ice and ten times greater than values for the interior of multiyear white ice (Grenfell and Maykut, 1978). The bulk extinction coefficient, calculated over the wavelength region 400 to 800 nm, is $.084 \text{ cm}^{-1}$. This optical bulk extinction coefficient is approximately five times larger than the values of $.017$ and $.012 \text{ cm}^{-1}$ measured by Untersteiner (1961) and Weller and Schwertfeger (1967) for multiyear ice and first-year ice, respectively.

The reason for the above differences must be related to other physical properties of the ice. In these experiments the ice is thinner, colder, and saltier than the sea ice observed in previous work. The causes of larger extinction coefficients in the thin cold ice case are examined in Section 4.3.

4.2.3 Thermal Determination of Extinction Coefficients

In three of the experiments an independent analysis of attenuation in the ice is undertaken to provide supplementary confirmation of the extinction coefficients. A method relating the heat absorbed in the ice to the extinction coefficient, comparable to that of Untersteiner (1961), is used.

The ice is illuminated for 200 minutes, with temperature profiles taken at the start and finish of that period. Knowing these temperature profiles and the salinity profile, the absorbed heat as a function of depth is calculated. From basic thermodynamics

$$dQ = c_s \rho dT \quad (4.2)$$

where dQ is the heat absorbed per unit volume, $c_s = 0.5 + 4.1(S/T^2)$ (Untersteiner, 1961), and ρ is the density $= \rho_{ice}(1-v_B) + \rho_w v_B \approx \rho_{ice}$. Integrating Equation (4.2) over temperature,

$$Q_2 - Q_1 = \rho(T_2 - T_1)(0.5 + 4.1 \frac{S}{T_1 T_2}) \quad (4.3)$$

Heat is transmitted within the ice by both conduction and absorption of radiation. A computer program, using a forward differences treatment of the heat conduction equation (Richtmyer, 1957), was written to evaluate the contribution of conduction to temperature changes within the ice. For the experimental conditions conduction was found to be insignificant below a depth of four centimeters, thus heating in this region is due only to absorbed radiation. Consequently,

$$\Delta Q_1 = \frac{\partial F_1}{\partial z_1} \Delta t \quad , \quad (4.4)$$

for time interval Δt at some depth z_1 . Since attenuation over a small z interval can be approximated by a Bouguer-Lambert model, Equation (4.4), at depths z_1 and z_{1+1} , is expressed as

$$\Delta Q_1 = -\kappa F_0 e^{-\kappa z_1} \Delta t \quad (4.5)$$

$$\Delta Q_{i+1} = -\kappa F_0 e^{-\kappa z_{i+1}} \Delta t \quad . \quad (4.6)$$

Dividing Equation (4.5) by (4.6) and solving for κ ,

$$\kappa = - \left[\ln \frac{\Delta Q_{i+1}}{\Delta Q_i} \right] / (z_{i+1} - z_i) \quad . \quad (4.7)$$

The κ calculated by Equation (4.7) is a bulk extinction coefficient, integrated over the spectrum available at depth z_i . Figure 4.11 illustrates salinity and temperature profiles, before and after radiative heating for ice 26 cm thick and grown at an air temperature of -37°C . The heat absorbed in two centimeter intervals for depths from 0 to 20 cm was calculated and displayed in Figure 4.12. For greater accuracy, a best fit of the curve was determined for the region from 4 to 12 cm. Shallower depths were influenced by conduction, while small temperature changes at larger depths increased errors. The bulk extinction coefficient determined in this fashion was 0.19 cm^{-1} , in general agreement with the optical results.

4.3 CORRELATION OF OPTICAL PROPERTIES AND PHYSICAL PARAMETERS

4.3.1 Overview

Sea ice is a complex medium with a state and structure dependent on such parameters as thickness, growth history, temperature, salinity, and brine volume. One of the goals of this research is to investigate correlations between the optical properties and the physical state and structure of the ice. Complicating this task are the interrelationships among the physical parameters themselves; for example, salinity and brine volume are explicitly related by Equation (3.2). More difficult

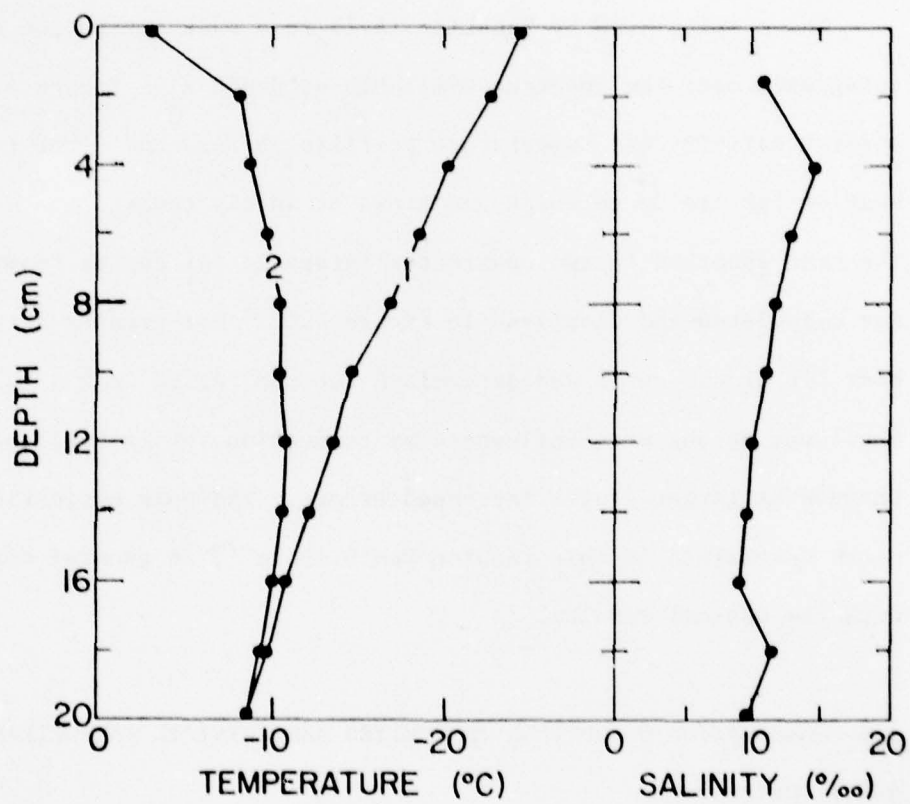


Figure 4.11: Temperature and salinity profiles used in thermal calculations of extinction coefficient: (1) $t = 0$ minutes and (2) $t = 200$ minutes.

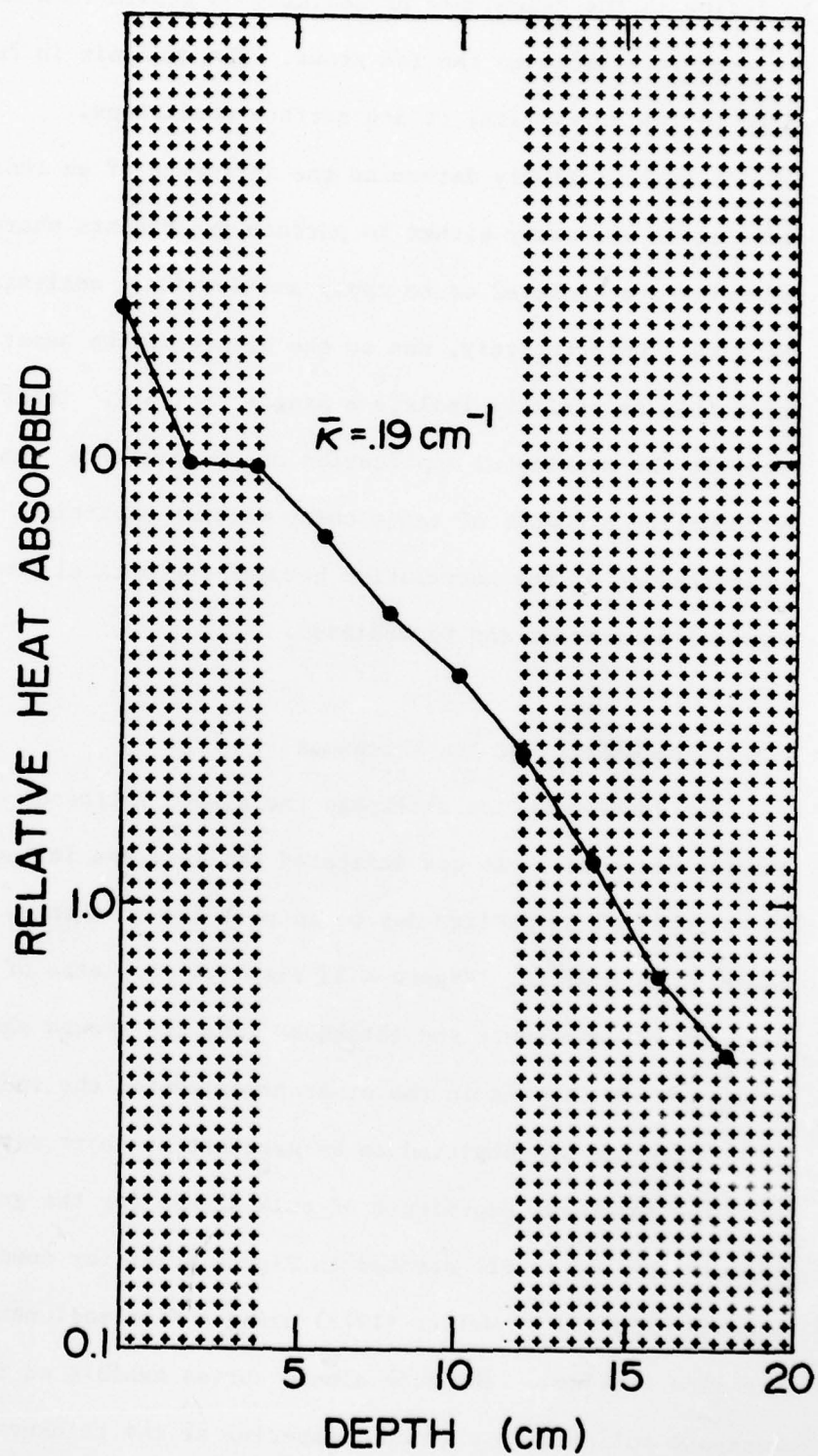


Figure 4.12: Profile of heat absorbed during a 200 minute period of illumination.

to define is the dependence of salinity on growth rate and changes in temperature profile as the ice grows. The analysis is further complicated by the variability of ice surface conditions.

To quantitatively determine the influence of an individual parameter it is necessary either to perform experiments where effects of the parameter are isolated or to apply multivariate analysis techniques to the data. Unfortunately, due to the nature of the experiments, it is impossible to strictly isolate a single variable. Insufficient data prohibit the meaningful application of multivariate analysis. However, by comparing a number of cases under varying conditions a qualitative understanding of the correlation between the optical properties and the physical parameters can be achieved.

4.3.2 The Effects of Ice Thickness

For increasing ice thickness the albedo increases and the transmission decreases. As was indicated earlier, the influence of thickness on the optical properties may be in part due to changes in the ice temperature profile. Figure 4.13 displays isopleths of albedo as a function of wavelength and thickness from the growth phase of Experiment 4 ($T_{\text{air}} = -20^{\circ}\text{C}$). As in the other experiments, the increase of albedo with thickness was observed to be greatest at short wavelengths.

The thickness dependence of bulk albedo for the growth phases of Experiments 3-6 is illustrated in Figure 4.14; for comparison bulk albedos measured by Weller (1972) using a Kipp radiometer (400 to 3000 nm) are also included. The bulk albedo curves exhibit an initial rapid increase followed by a gradual tapering as the thickness increases. The large increase in Curve 4, as the thickness increases from 17.4 to 23.7

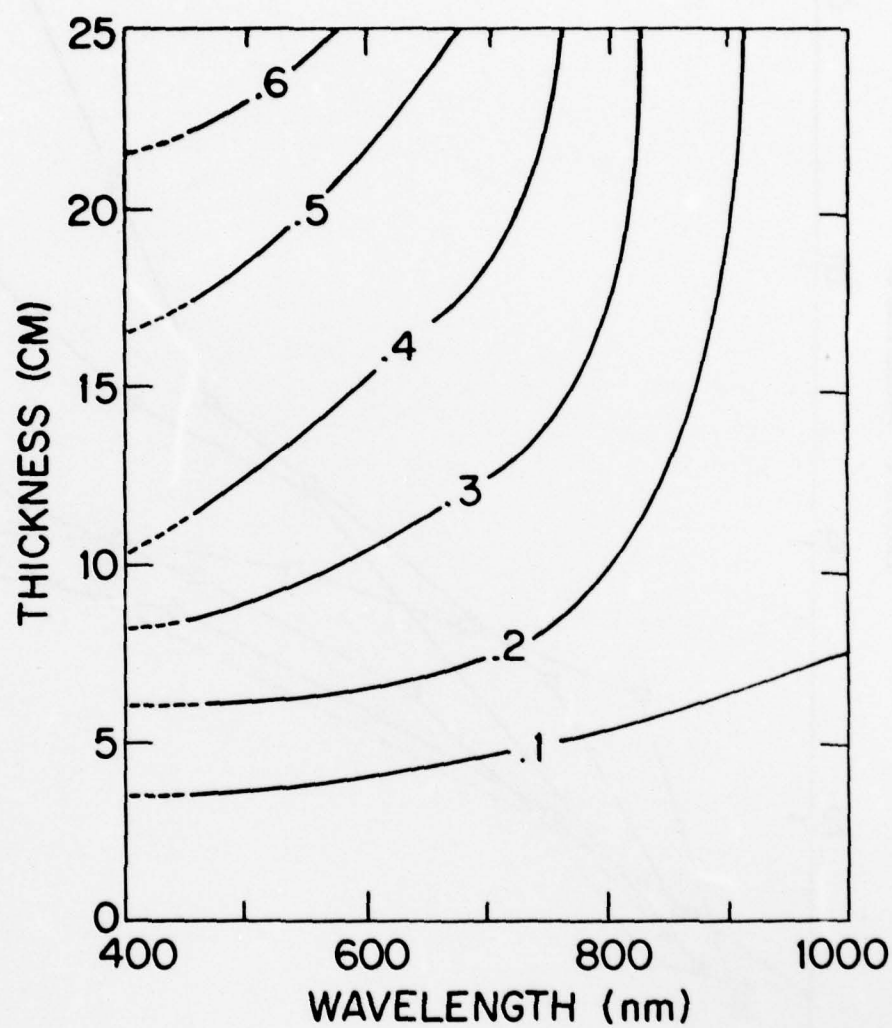


Figure 4.13: Isopleths of albedo as a function of wavelength and thickness (taken from the growth phase of Experiment 4).

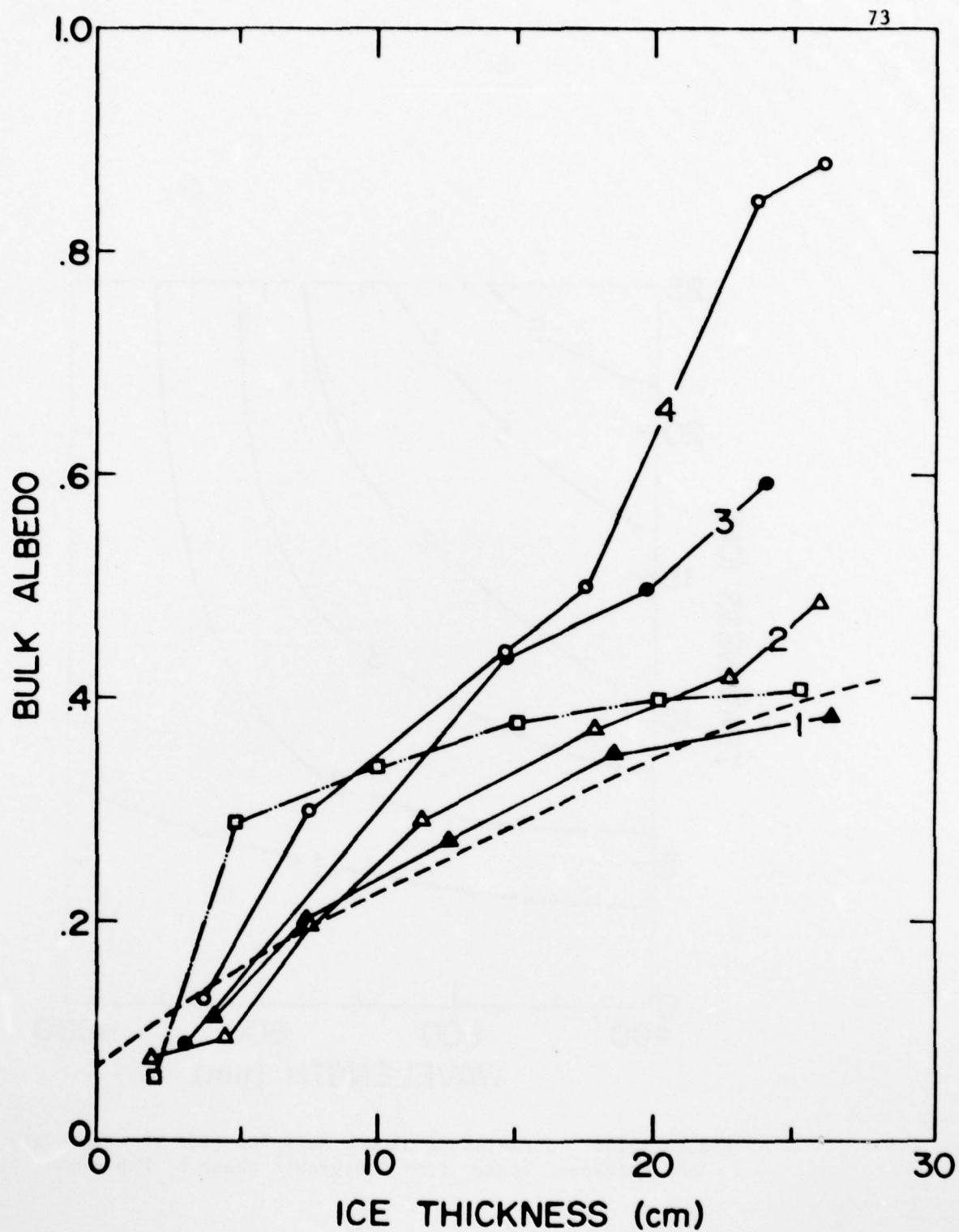


Figure 4.14: Bulk albedo as a function of ice thickness for:
 (1) Experiment 3 (air temperature of -10°C); (2) Experiment 4 (-20°C);
 (3) Experiment 5 (-30°C); (4) Experiment 6 (-37°C);
 Weller, 1972; and ----theoretical curve using Equation 5.1.

cm, is due to the temperature in the upper few centimeters of the ice dropping below the eutectic point, resulting in the precipitation of solid salts.

Using a simple approach a relationship between bulk albedo and thickness is derived. Assuming single scattering, vertically homogeneous reflectivity, exponential attenuation within the ice, and specular reflection of magnitude R_0 , the contribution to the albedo from a layer a depth dz thick is

$$\alpha_B(dz) = be^{-2az} \quad (4.8)$$

Integrating over z from 0 to H gives

$$\alpha_B(H) = \frac{b}{2a} (1 - e^{-2aH}) + R_0 \quad (4.9)$$

where the specular reflection R_0 is seven percent, b and a are the amounts backscattered and absorbed in a layer dz . Thickness dependent bulk albedos from Experiment 3 conducted at an air temperature of -10°C are least influenced by changes in temperature profiles and are selected to fit Equation (4.9). A nonlinear regression program, using Equation (4.9) and ordered pairs of bulk albedo and thickness as input, calculated b and a to be .0184 and .0149, respectively, with a correlation coefficient of .98. Not only does Equation (4.9) fit the data reasonably well (dashed curve, Figure 4.14), but in the limiting case of very large ice thickness ($H \rightarrow \infty$) it gives a physically realistic value of .69.

A relationship such as Equation (4.9), while offering little physical insight, is of practical value. Maykut (1977) discusses the importance of thickness variation in the large-scale (regional) heat and

mass balance of the ice pack. If the ice thickness distribution $g(H)$ is known, then the regional average of some thickness dependent property $\phi(H)$ is given by

$$\bar{\phi} = \int_{H_{\min}}^{H_{\max}} \phi(H)g(H)dH \quad . \quad (4.10)$$

Substituting Equation (4.9) into Equation (4.10) for a known thickness distribution of bare ice, a regional albedo average can be calculated.

4.3.3 The Effects of Air Temperature During Freezing and Growth Rate

For Experiments 3-6 the air temperatures during the growth phase were -10 , -20 , -30 , and -37°C , enabling an investigation of how differences in the air temperature during freezing and thus the growth rate affect the optical properties. According to the Stefan equation (Carslaw and Jaeger, 1959) the air temperature and growth rate, assuming a linear temperature gradient in the ice, are related by

$$f = \frac{dH}{dt} = \frac{c_t(T_f - T_a)}{L_f \rho_{\text{ice}} H} \quad (4.11)$$

where L_f is the latent heat of fusion, T_a is the air temperature ($^{\circ}\text{K}$), T_f is the freezing temperature, c_t is the coefficient of thermal conductivity, ρ_{ice} is the density of ice, and H is the ice thickness. Because of the dependence of growth rate on ice thickness, to facilitate comparisons, each experiment was represented by a growth rate determined when the ice was 10 cm thick.

Data from the growth phase of Experiments 3-6 were used to construct contours of bulk albedo as a function of ice thickness and air temperature (Figure 4.15) and as a function of ice thickness and growth rate

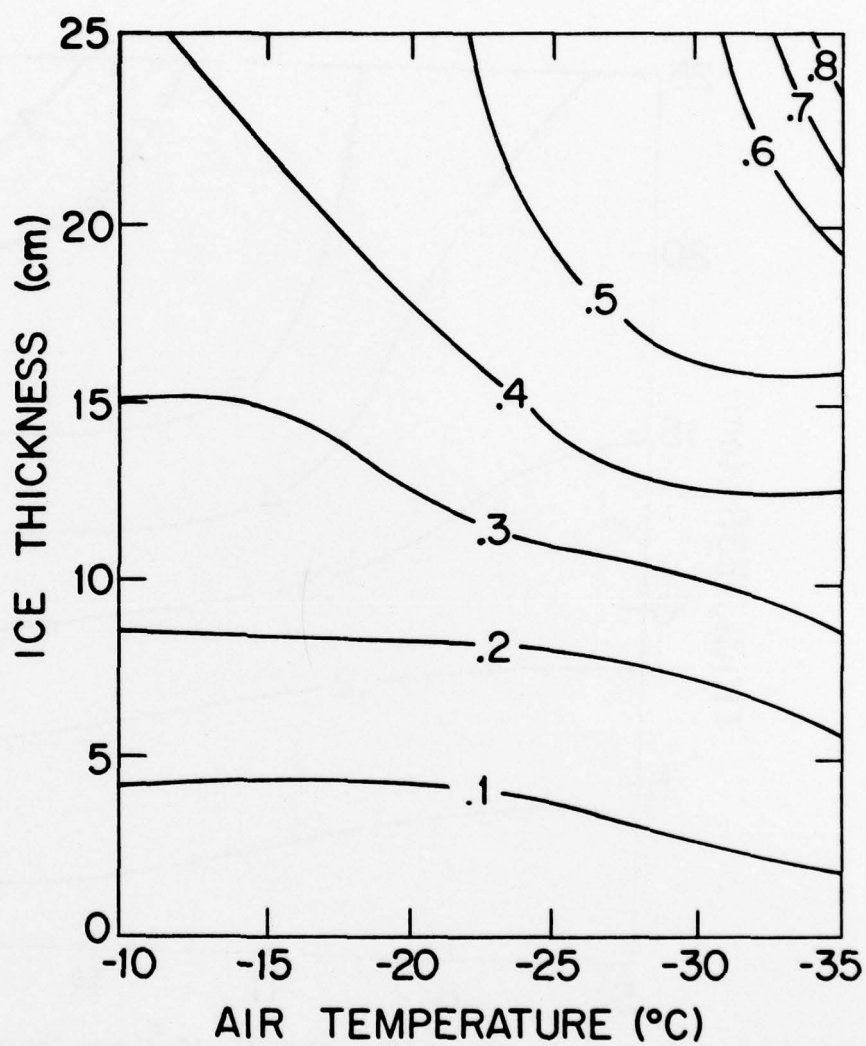


Figure 4.15: Isopleths of bulk albedo as a function of air temperature during freezing and ice thickness.

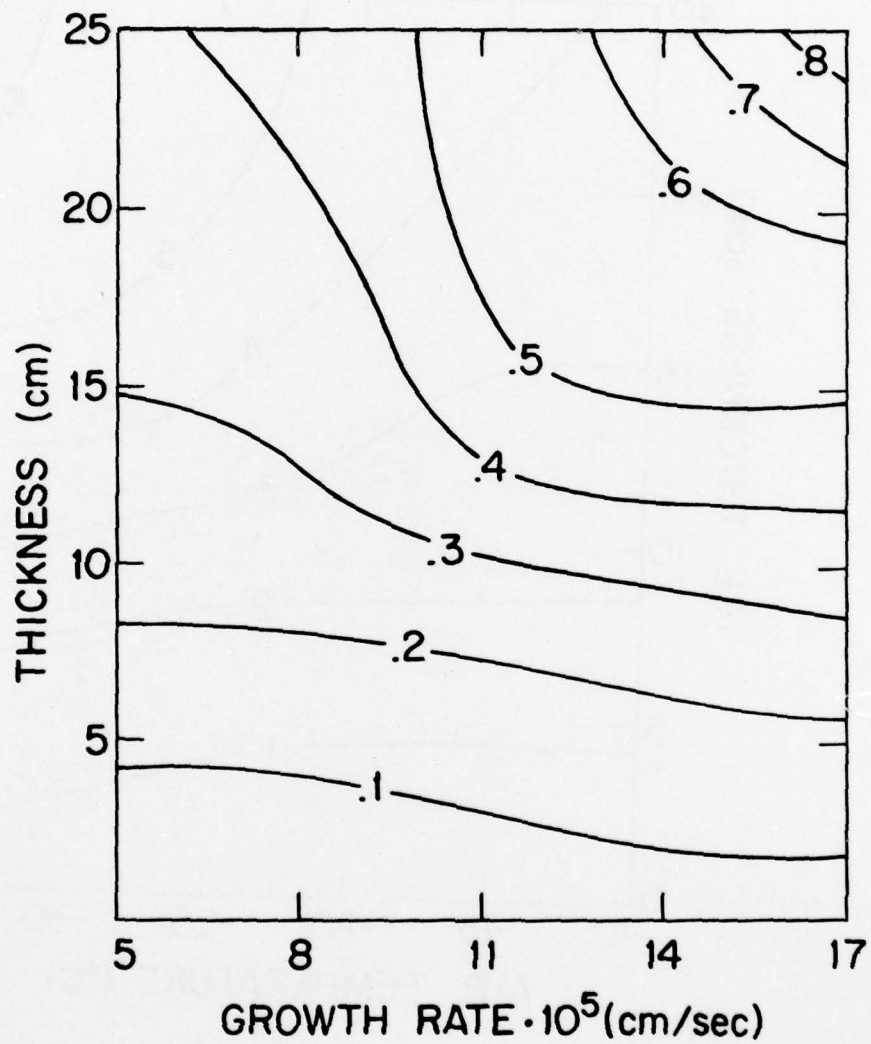


Figure 4.16: Isopleths of bulk albedo as a function of growth rate and ice thickness

(Figure 4.16). Lack of data makes the portion of the 0.5 contour above 17 cm uncertain. Both figures display the same general characteristic: a weak dependence of albedo on air temperature and growth rate when the ice is thin which becomes increasingly strong as the ice thickens. The very large albedos (upper right hand corner of plots) are a result of the formation of highly reflective solid salts when the ice temperature dropped below the eutectic point.

Spectral albedos, selected from Experiments 3-6, for ice of comparable thickness (about 20 cm) are plotted in Figure 4.17. In all cases, the albedo increases as the growth rate increases (air temperature decreases), with the albedo more than doubling between Curves 1 and 4. Displayed in Figure 4.18 are corresponding spectral extinction coefficients calculated for the same cases shown in Figure 4.17. Ice grown under colder conditions (faster growth) exhibits larger extinction coefficients, increasing at 600 nm by a factor of five between Curves 1 and 4.

The experiments discussed so far, in addition to different growth conditions, also have dissimilar ice temperature profiles. Therefore, observed differences may be due to variations both in growth rate and in temperature profile. To more fully isolate the effect of the growth rates on the optical properties, sites are compared where the temperature profiles are nearly the same. In Experiments 3, 5, and 6, as part of the warming phase, the ice was allowed to come to thermal equilibrium at a temperature near the melting point. Though less pronounced than results from growth phase, warming phase results show a distinct correlation between growth rate and optical properties of the ice (Figures 4.19 and 4.20). Table 4.4 compares relative and absolute values of albedo

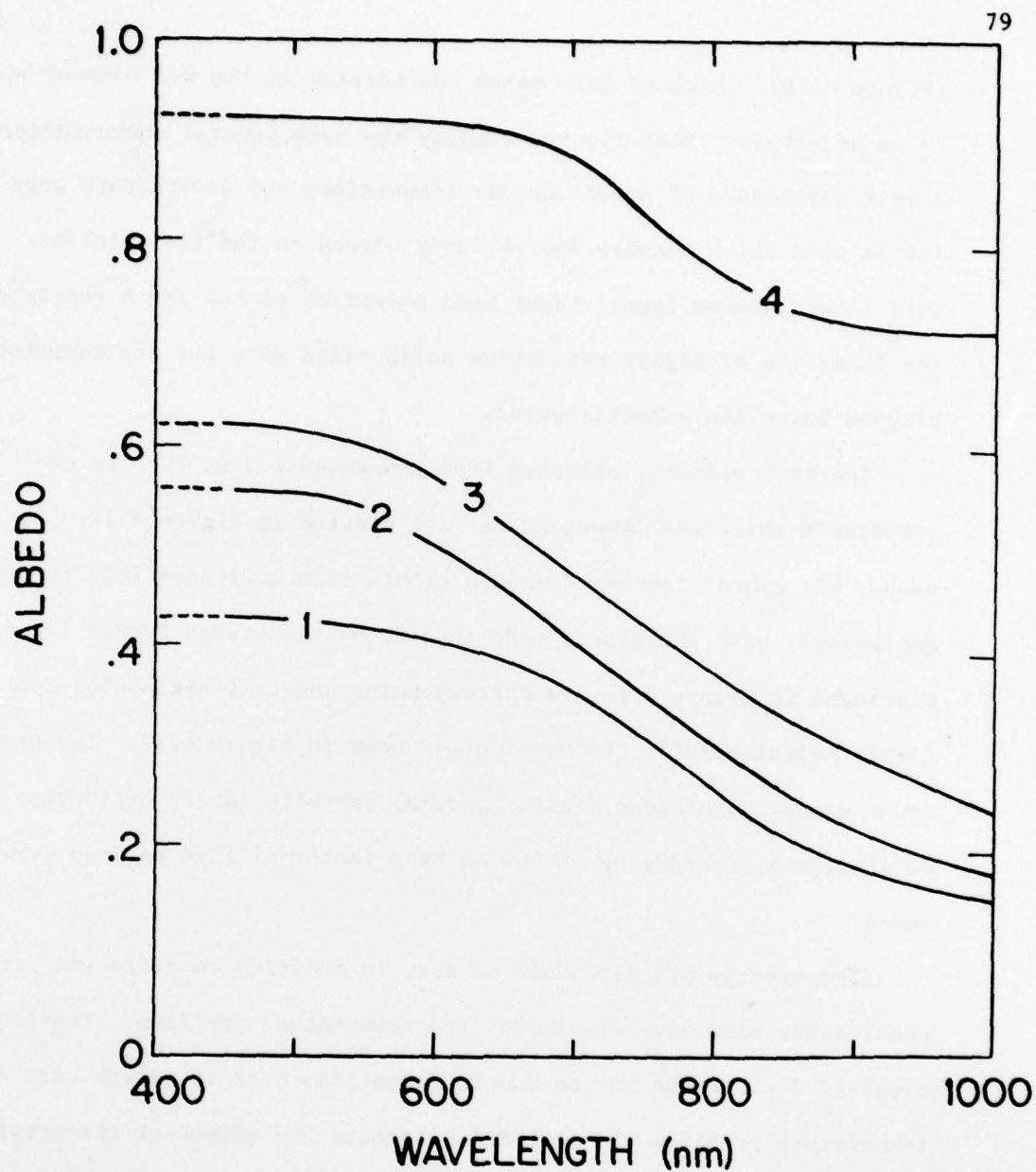


Figure 4.17: Spectral albedo comparisons for sea ice grown at different air temperatures. The growth rates were determined when the ice was 10 cm thick.

Experiment	Thickness (cm)	Air Temp (°C)	Growth Rate ($\times 10^{-5}$ cm/sec)	Bulk Albedo (cloudy)
(1) 3	21.1	-10	4.5	.37
(2) 4	21.6	-20	8.0	.42
(3) 5	19.6	-30	11.4	.53
(4) 6	23.5	-37	17.0	.86

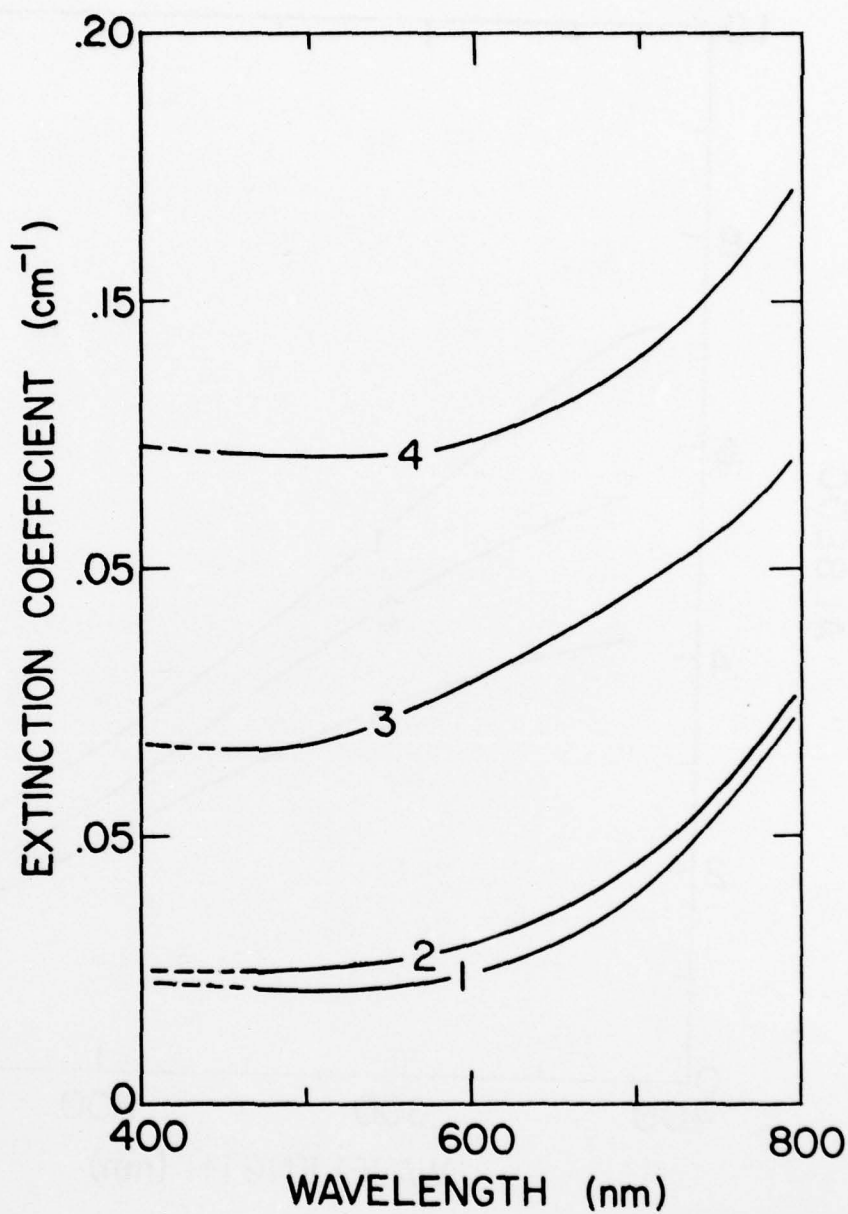


Figure 4.18: Comparison of spectral extinction coefficients for ice grown at different air temperatures. The numbers correspond to the same cases described in Figure 4.17.

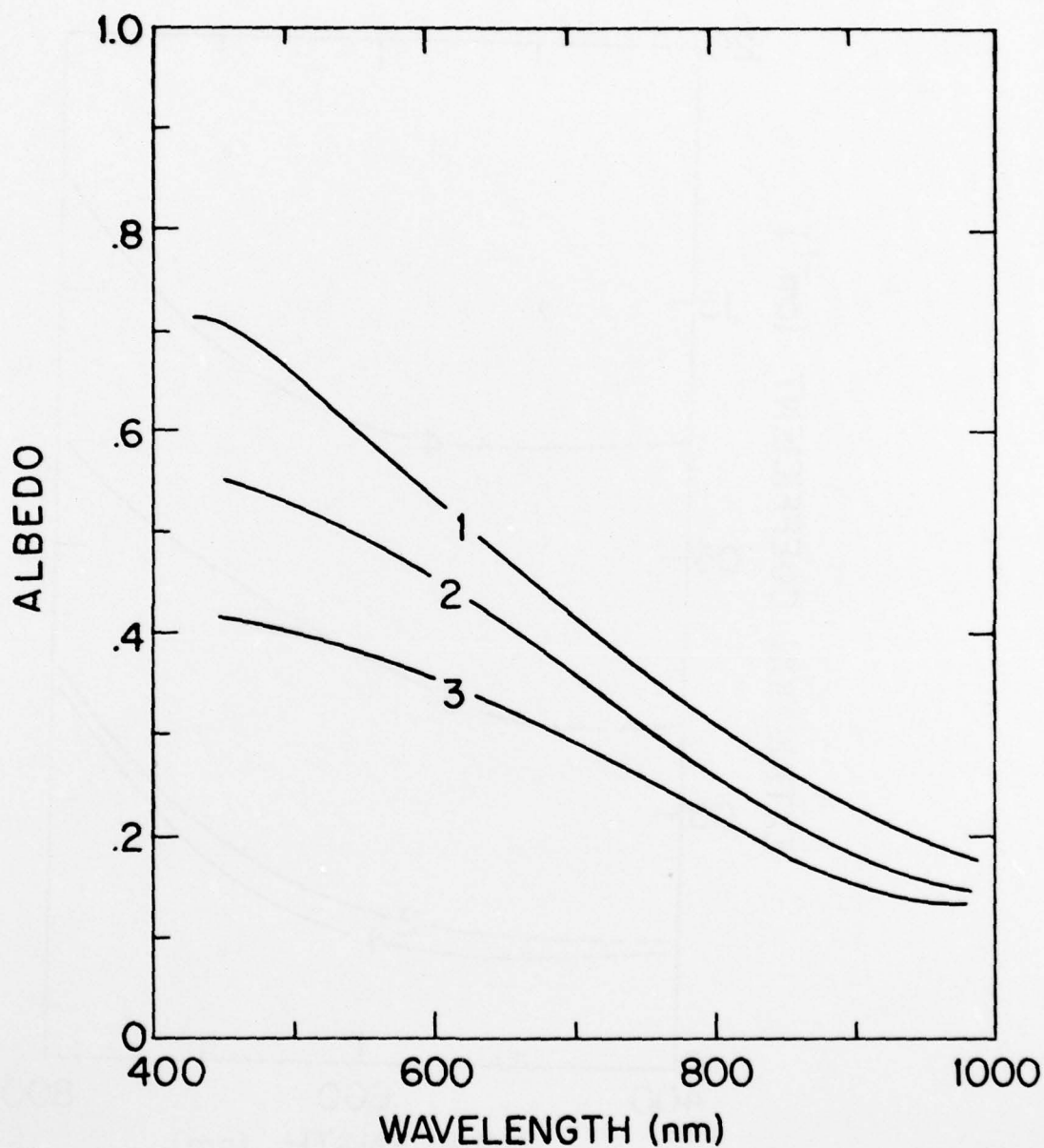


Figure 4.19: Comparison of spectral albedos for ice of similar temperature profiles, but grown at different air temperatures. In each case the ice is roughly 28 cm thick and the air temperature is approximately 0°C : (1) Experiment 6, grown at an air temperature of -37°C , and cloudy sky bulk albedo of .51; (2) Experiment 5, -30°C , .42; and (3) Experiment 3, -10°C , .33.

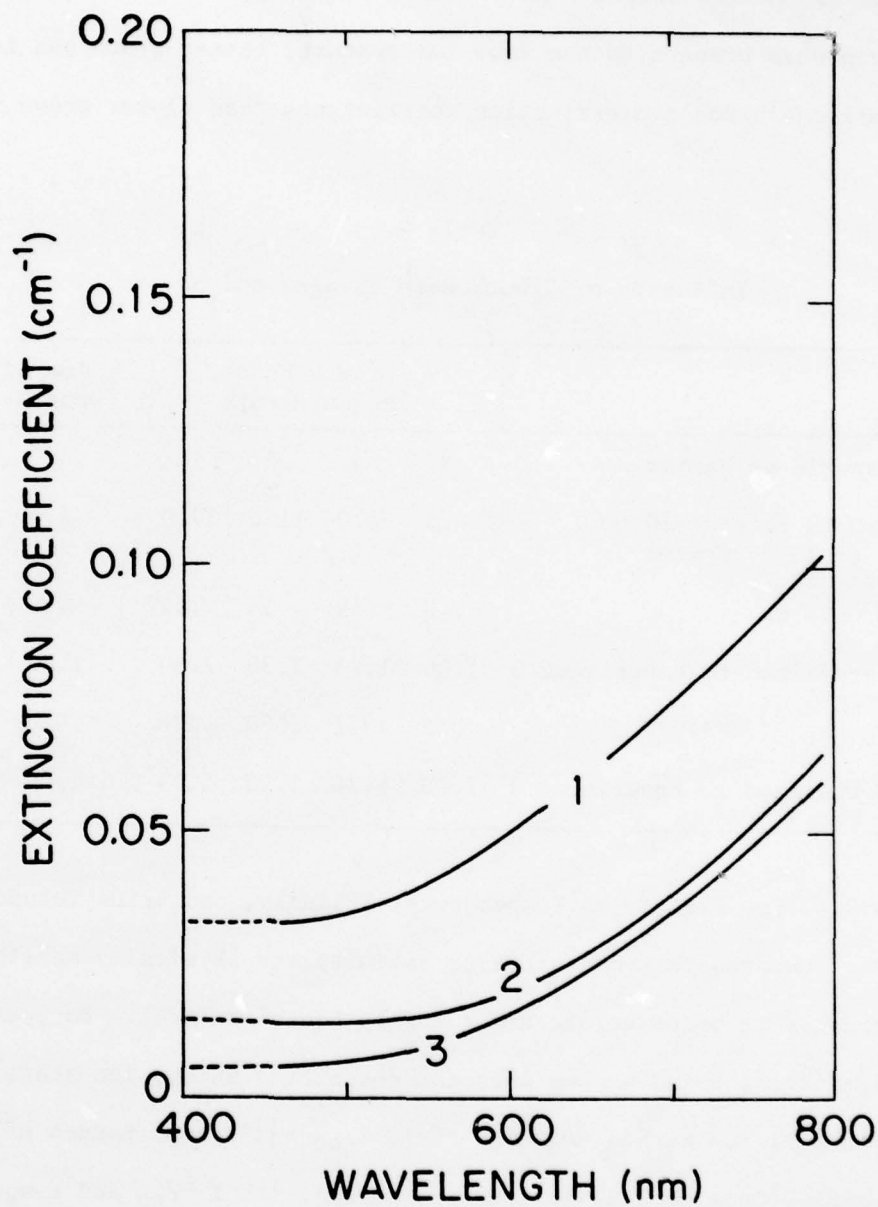


Figure 4.20: Comparison of spectral extinction coefficients for ice of similar temperature profiles, but grown at different air temperatures. The conditions and numbers correspond to the same cases described in Figure 4.19.

AD-A074 908

WASHINGTON UNIV SEATTLE DEPT OF ATMOSPHERIC SCIENCES
THE OPTICAL PROPERTIES OF YOUNG SEA ICE (U)

F/G 8/12

UNCLASSIFIED

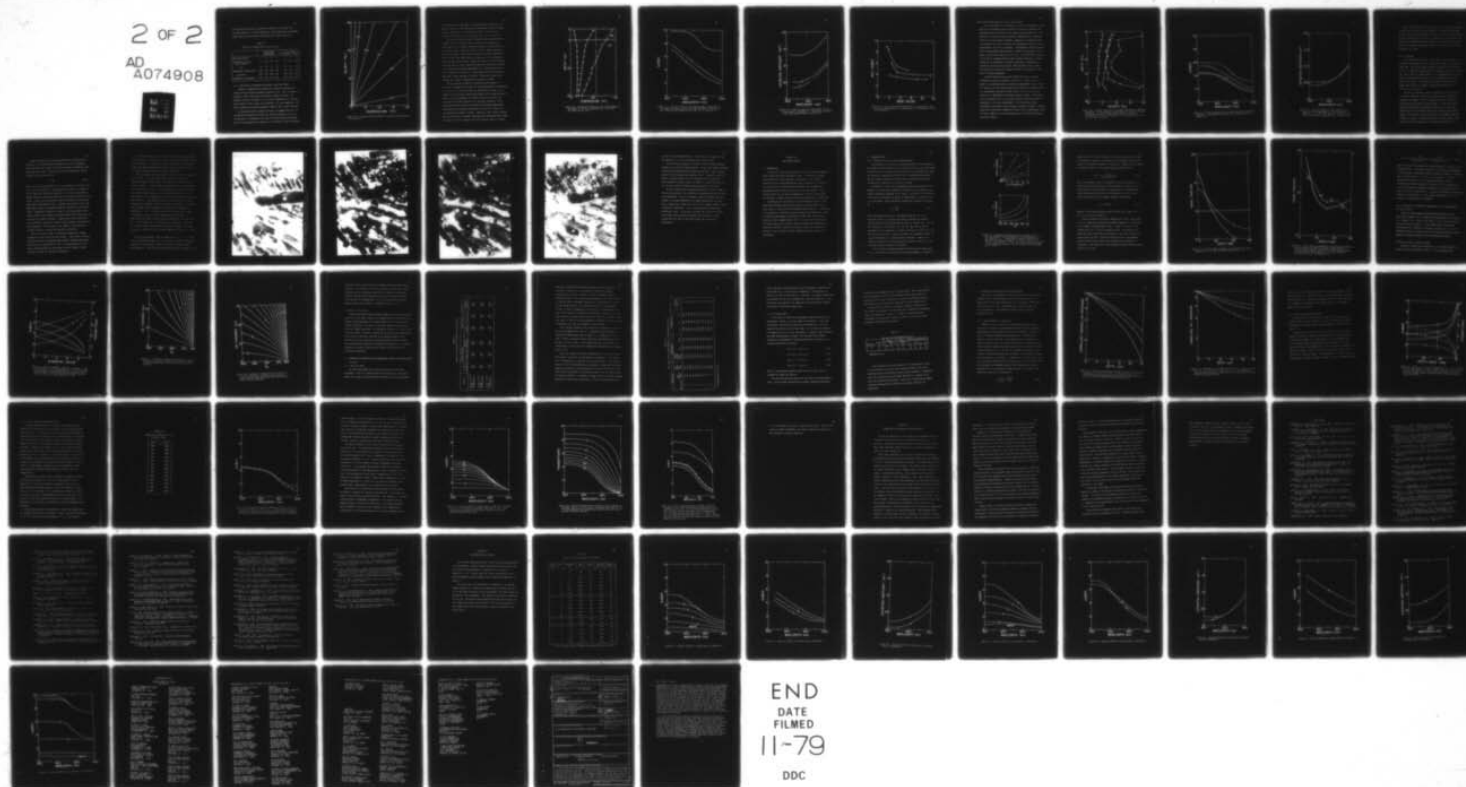
AUG 79 D K PEROVICH
SCIENTIFIC-17

N00014-76-C-0234

NL

2 OF 2

AD
A074908



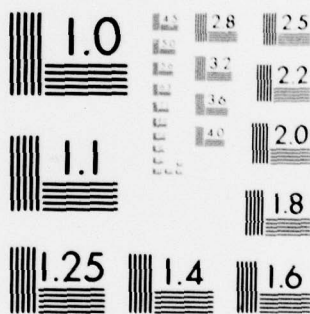
END

DATE

FILMED

11-79

DDC



MICROCOPY RESOLUTION TEST CHART
NATIONAL BUREAU OF STANDARDS-1963-A

and extinction coefficient obtained from Figures 4.17 through 4.20. Even when brought to the same temperature, faster grown sea ice exhibits larger albedos and extinction coefficients than slower grown ice.

Table 4.4
Influence of Growth Rate on α_{600} and κ_{600}

	Growth Phase Measurements				Ice of Similar Temperature Profile		
Experiment Number	3	4	5	6	3	5	6
Growth Rate at 10 cm ($\times 10^{-5}$ cm/sec)	4.5	8.0	11.4	17.0	4.5	11.4	17.0
α_{600}	.40	.49	.55	.92	.36	.45	.53
Normalized to Experiment 3	1.00	1.23	1.38	2.30	1.00	1.25	1.47
$\kappa_{600}(\text{cm}^{-1})$.025	.031	.080	.126	.016	.019	.050
Normalized to Experiment 3	1.00	1.24	3.20	5.04	1.00	1.19	3.13

4.3.4 The Effects of Temperature, Salinity, and Brine Volume

Changes in temperature or salinity are physically manifested by changes in brine volume according to Equation (3.3). But, as Figure 4.21 indicates, brine volume does not describe a unique ice state. For example, ice with a salinity of 10 ‰ and a temperature of -20°C has a brine volume of 2.8% as does ice of salinity 1 ‰ and temperature -2°C . Their structure and optical properties, however, can be quite different.

As discussed earlier, Figures 4.17 and 4.18 suggest that both ice temperature and growth rate affect the optical properties of sea ice. The influence of temperature could best be studied during the warming phase of an experiment when changes in ice thickness, crystal structure,

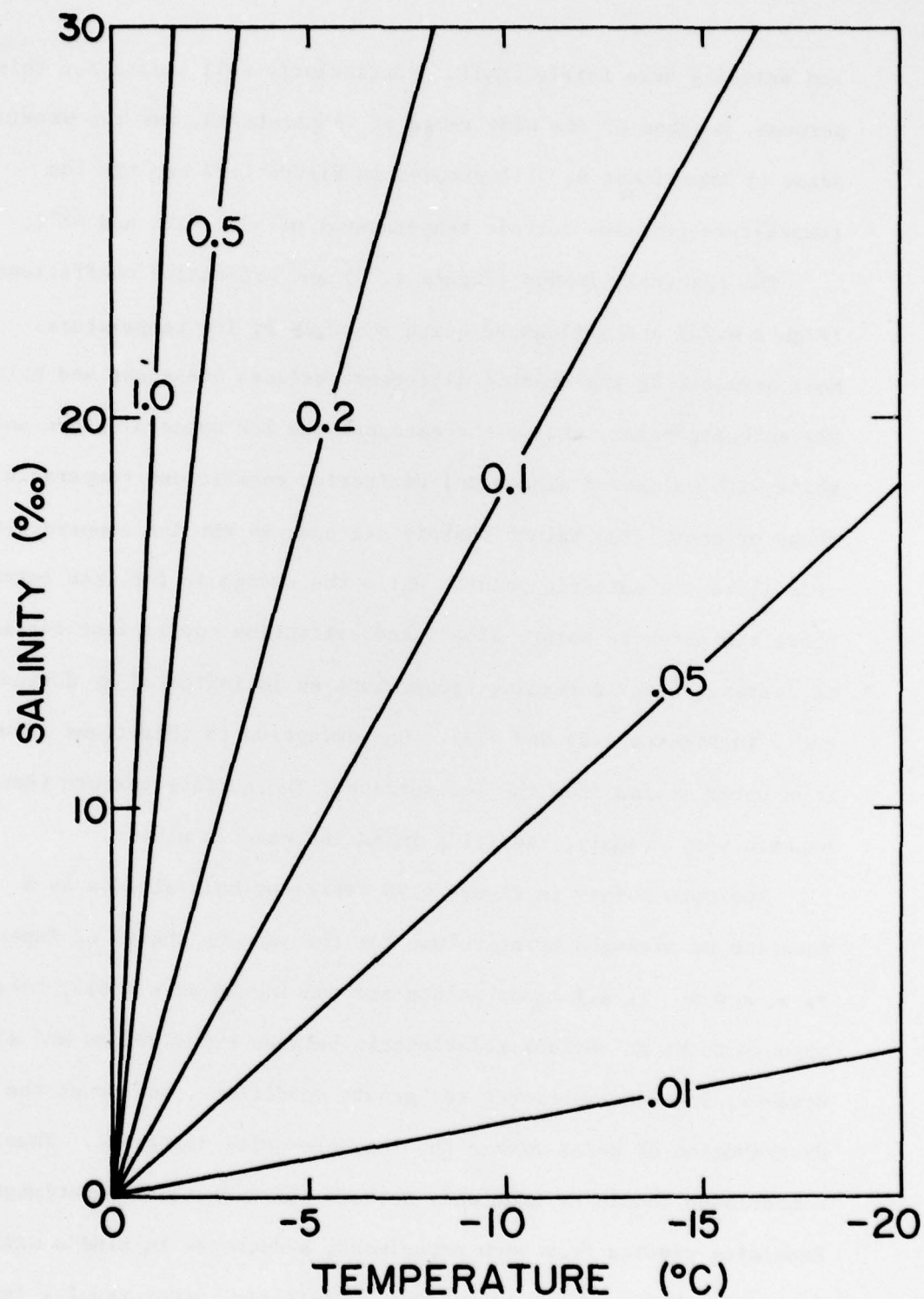


Figure 4.21: Isopleths of brine volume as a function of temperature and salinity.

and salinity were fairly small. Particularly well suited for this purpose, because of the wide range of temperatures, was the warming phase of Experiment 6. Illustrated in Figure 4.22 are the ice temperature profiles for air temperatures of -37°C , -22°C , and -2°C .

The spectral albedos (Figure 4.23) and extinction coefficients (Figure 4.24) are influenced quite strongly by ice temperature. Most dramatic is the drastic difference between ice above and below the eutectic point. Below the eutectic the ice appears opaque and white with values of albedo and extinction coefficient comparable to those of snow. The values sharply decrease as the ice temperature goes above the eutectic point. While the change is far less extreme above the eutectic point, albedo and extinction coefficient continue to decrease with increasing temperature as is indicated by Curves 2 and 3 in Figures 4.23 and 4.24. One exception to this trend occurs when water drains from the ice surface. The surface texture then becomes very crumbly, resulting in an increase in albedo.

The data points in Figure 4.25 represent bulk albedos as a function of averaged brine volume for the warming phases of Experiments 3, 5, and 6. If all these points are considered as a whole, there appears to be no obvious relationship between brine volume and albedo. However, in each experiment the growth conditions, and hence the distribution of brine within the ice, are quite different. Thus, comparisons should be made only between the individual experiments. Examining results from each experiment, a decrease in albedo with increasing brine volume is evident. Similarly, other results indicate that the extinction coefficient decreases with increasing brine volume. The family of curves in Figure 4.25 also indicates that for a given

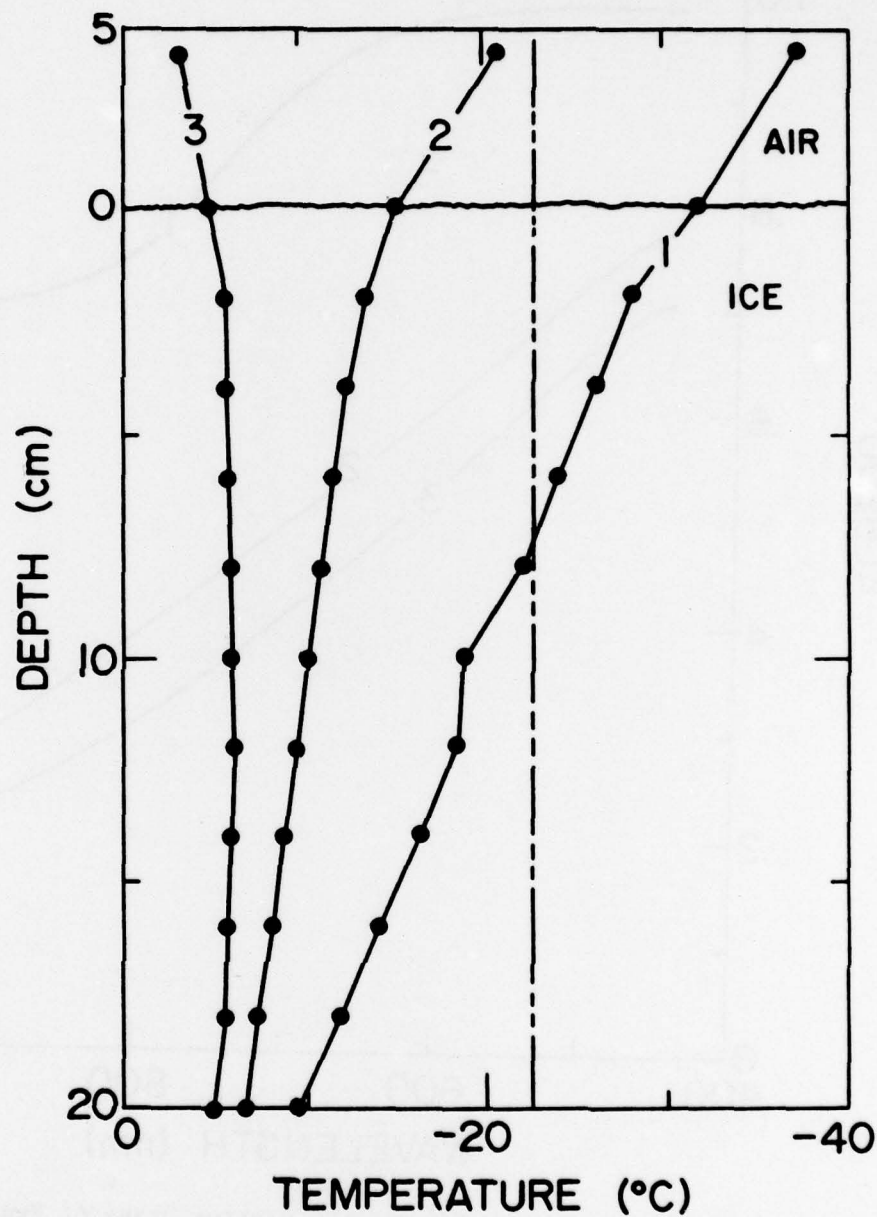


Figure 4.22: Temperature profiles for the warming phase of Experiment 6. The air temperature was: (1) -37°C ; (2) -22°C ; and (3) -2°C .

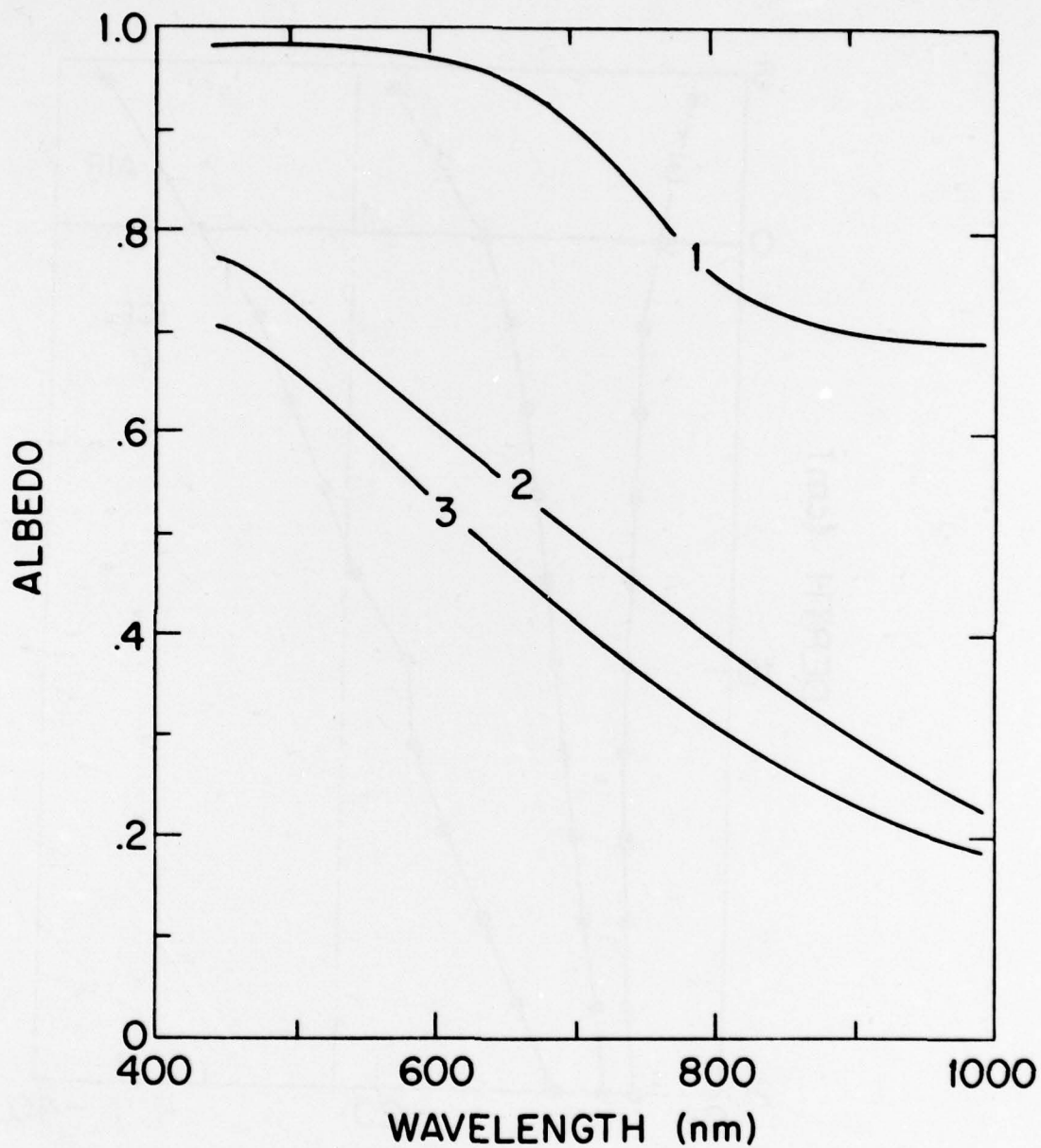


Figure 4.23: Spectral albedos for the warming phase of Experiment 6. The numbers correspond to the same cases described in Figure 4.22. The cloudy sky bulk albedos are (1) .90, (2) .59, and (3) .51.

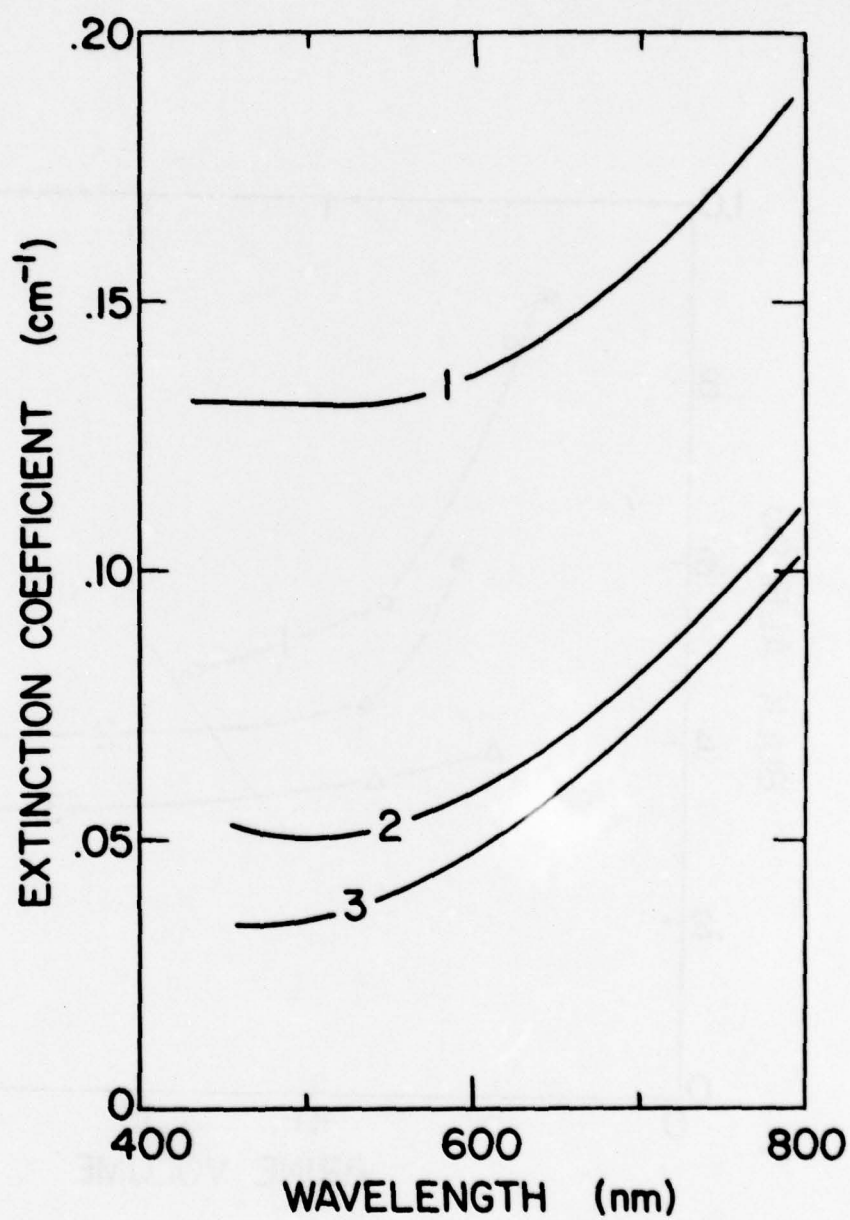


Figure 4.24: Spectral extinction coefficients for the warming phase of Experiment 6. The numbers correspond to the same cases described in Figure 4.22.

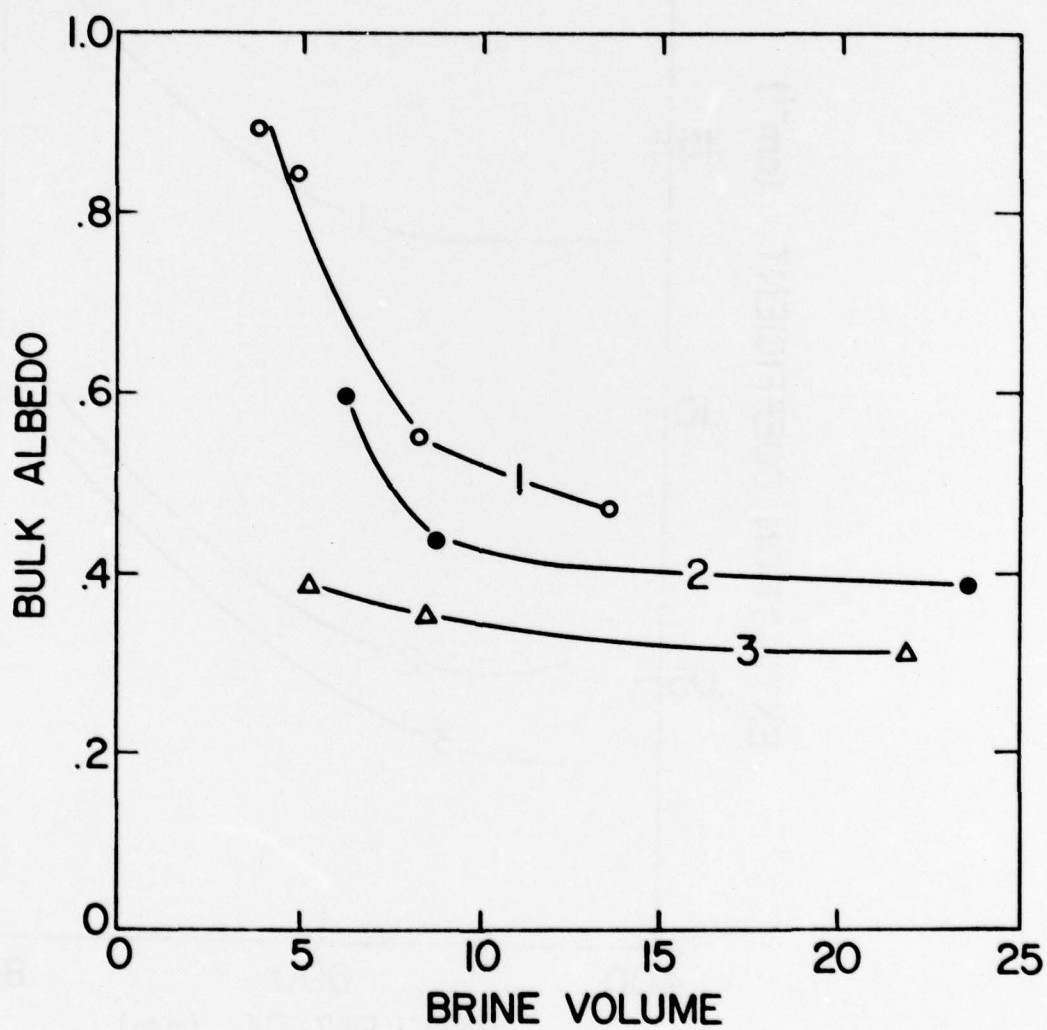


Figure 4.25: Brine volume versus bulk albedo for measurements taken during the warming phase of (1) Experiment 6; (2) Experiment 5; and (3) Experiment 3.

brine volume faster grown ice has a larger albedo.

The relationship of ice salinity to the optical properties is very difficult to determine, since typically the effects of salinity are intertwined with the effects of ice temperature and growth rate. The influence of salinity is best observed by comparing ice of different salinity, but with similar thickness, temperature, and growth history. To investigate the role of salinity, two intermediate salinity cases (Experiments 7 and 8) were performed. Environmental conditions during these two experiments were identical to those of Experiments 3 and 4, except that the water salinity was 16 ‰. With lower water salinity, less brine was entrapped despite similar growth conditions. By duplicating the air temperature of previous experiments comparable ice temperature profiles were obtained. While decreased water salinity did increase the growth rate [Equation (4.10)] the change was quite small for these experiments.

Salinity profiles and spectral albedos for sites of similar thickness are plotted in Figures 4.26 and 4.27. Curves 3 and 4 in Figure 4.27 comparing spectral albedos from Experiments 3 and 7, while not identical, do not display significant differences. However, there is a significant difference between Curves 1 and 2, with the less saline ice of Experiment 8 displaying a greater albedo. This difference is primarily due to a very saline surface water skim present in Experiment 4, but not in Experiment 8. The water skim reduces scattering in the surface layer causing a decrease in albedo. Spectral extinction coefficients, compared in Figure 4.28 for Experiments 4 and 8, differ slightly for short wavelengths and are virtually identical from 600 to 800 nm.

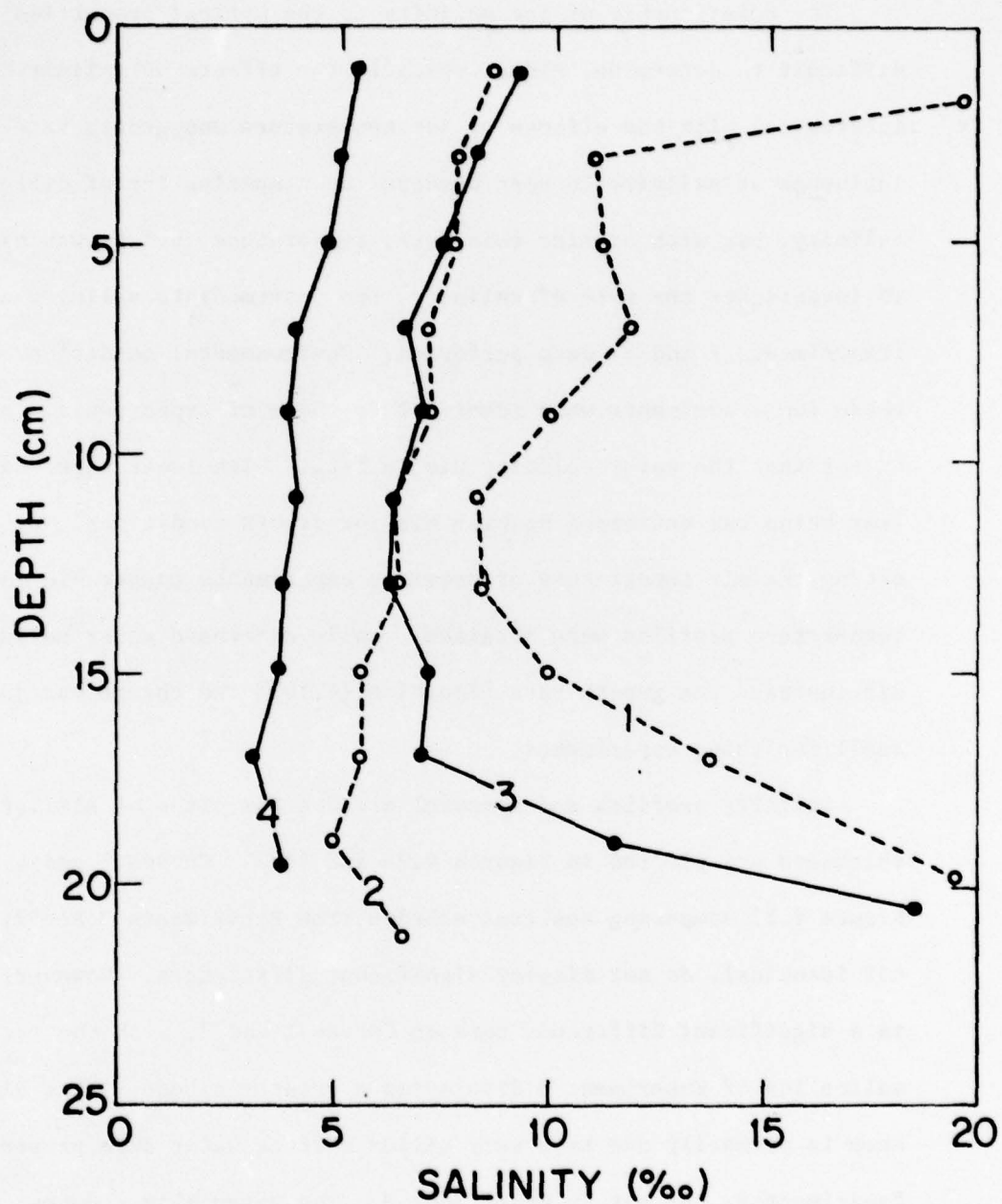


Figure 4.26: Salinity profiles for ice grown from water of different salinities. In all cases the ice is roughly 22 cm thick. The air temperature and initial water salinity for the cases are: (1) -20°C , $30.2\text{ }^{\circ}/_{\text{oo}}$; (2) -20°C , $16.5\text{ }^{\circ}/_{\text{oo}}$; (3) -10°C , $30.6\text{ }^{\circ}/_{\text{oo}}$; and (4) -10°C , $16.3\text{ }^{\circ}/_{\text{oo}}$.

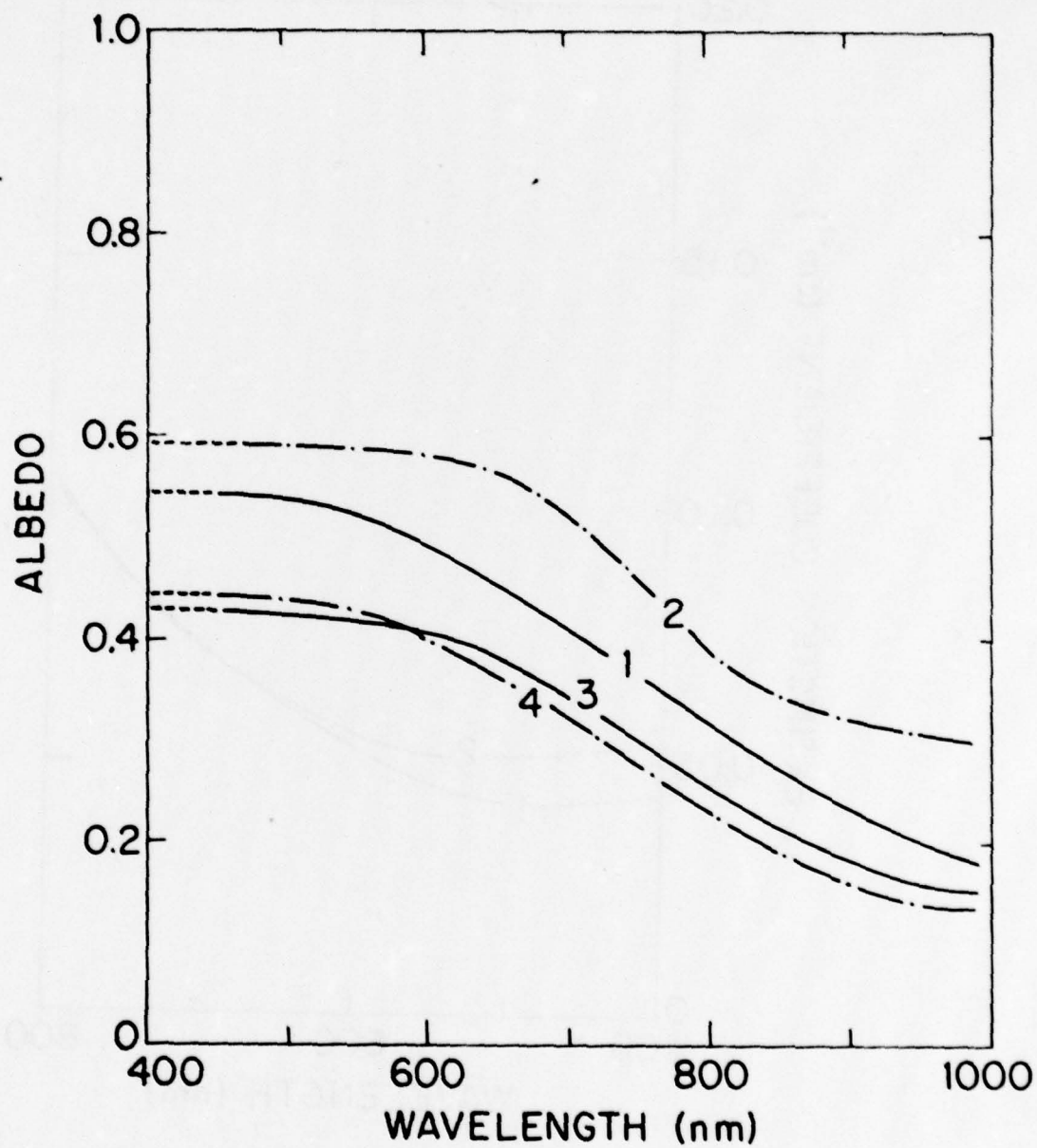


Figure 4.27: Spectral albedos for ice grown from water of different salinities. The numbers correspond to the cases described in Figure 4.26.

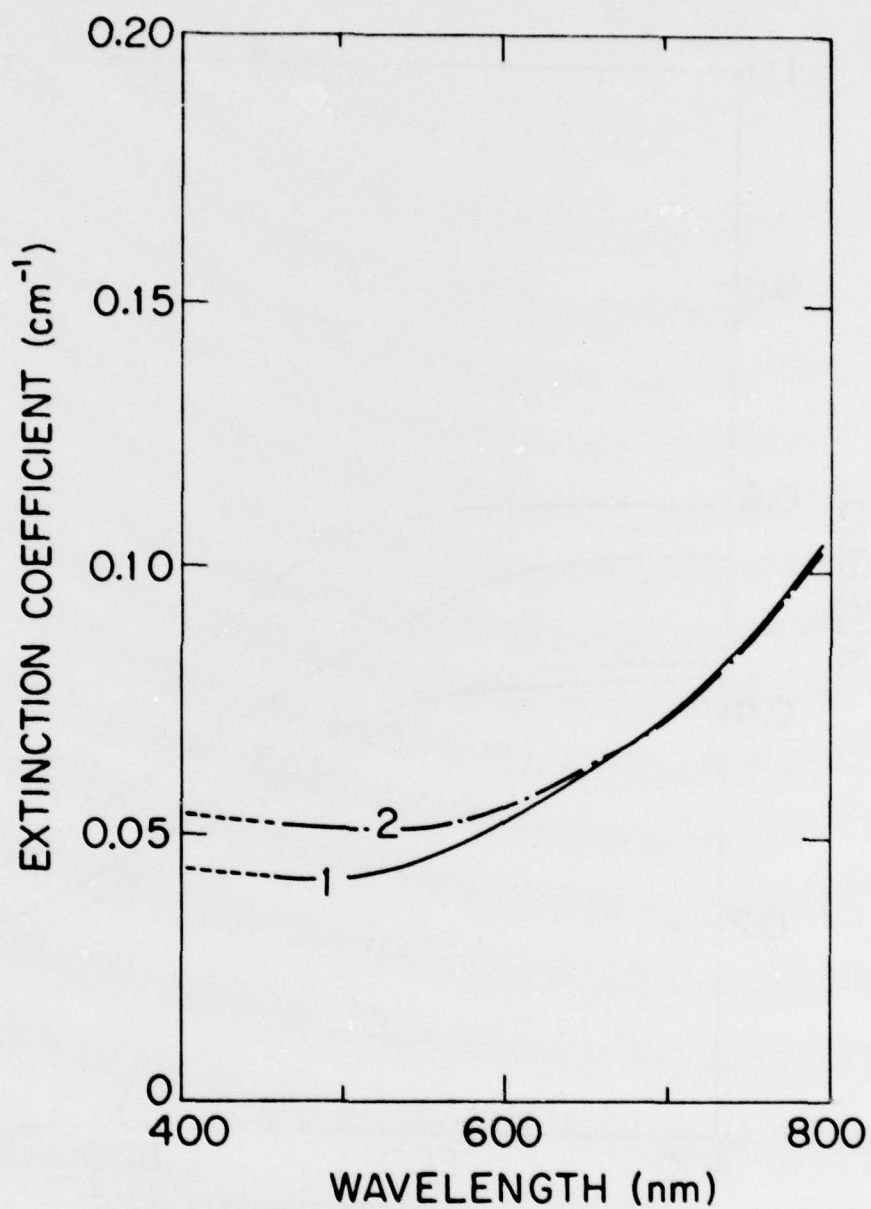


Figure 4.28: Spectral extinction coefficients for ice grown at an air temperature of -20°C from water of salinity: — 30.2 ‰ and - - - 16.5 ‰. The numbers correspond to cases described in Figure 4.26.

Lane's (1975) results indicate that above 5 ‰ salinity appears to have little effect on light transmission. Certainly small amounts of salt affect the optical properties of the ice; this is quite evident from the limiting case of fresh ice. However, for the relatively high salinities investigated here and within the resolution of this experiment, no consistent relationship between ice salinity and the optical properties is evident.

4.3.5 Discussion

Since the absorption by the ice and brine is fixed, changes in the optical properties of the ice result from changes in the amount of scattering. The initial sharp increase in albedo with ice thickness is due to a rapidly increasing number of opportunities for back scattering. But as the ice becomes thicker it is increasingly difficult for light to penetrate deep into the ice, be backscattered, and travel back to the surface. Contributions to albedo are mostly from the upper layers, hence the asymptotic behavior with thickness as illustrated in Figure 4.13.

The optical properties, albedo in particular, are sensitive to ice surface conditions. When an ice surface becomes crumbly and irregular, the number of air-ice interfaces increases, enhancing scattering and resulting in larger albedos. A water skim smooths surface irregularities reducing scattering and is a layer where absorption, but no scattering takes place, effecting a decrease in albedo. This decrease is more pronounced at wavelengths where the absorption is great. Theoretical studies of how the surface layer affects the optical properties are discussed in Section 5.4.3.

Growth rate affects the optical properties by altering the ice structure. As the growth rate increases, more brine is entrapped and the platelet and crystal sizes decrease (Weeks and Hamilton, 1962; Weeks and Assur, 1967). Weeks and Assur (1967) empirically related platelet size and growth rate by

$$f = \frac{P}{a^2} \quad (4.12)$$

where a is the platelet width (cm), f is the growth rate (cm/sec), and p is 1.33×10^{-7} (cm³/sec). Predicted platelet widths, at a depth of 10 cm, range from .28 mm for Experiment 6 to .54 mm for Experiment 3. Smaller platelets and crystals imply more scattering locations per unit volume. Crystal size and platelet width also gradually increase with depth (Weeks and Hamilton, 1962). Crystals and platelets in the tank experiments, while not rigorously monitored, appeared to follow these trends. Examining air bubbles in fresh ice, Gow and Langston (1972) found as growth rate increases the average bubble radius decreases and the density of bubbles increases. Higher growth rates yielded more brine inclusions, platelets, crystals, and air bubbles, producing more scattering sites. This increase in the number of scattering sites produces increases in albedo and extinction coefficient.

Below the eutectic point ice appearance dramatically changes, becoming very white with solid salts visible. Sinha (1977), using an electron microscope, photographed brine pockets showing precipitated solid salts at a temperature of -30°C. The precipitation of solid salts, providing additional scattering locations, causes a marked increase in albedo and extinction coefficient.

Above the eutectic point ice structure variations with temperature are less obvious. Viewing a vertical ice section in transmitted light, as the temperature is raised, the features within the ice become more visible and light transmission increases, but the structural cause is not apparent without detailed microscopic examination.

After growing an ice sheet roughly 20 cm thick at an air temperature of -30°C , a core was removed and a sample was prepared for observation under the microscope. The sample was a horizontal thin section, roughly .7 cm thick from 10 cm deep in the ice. The salinity of the sample was $11.2 \text{ }^{\circ}/_{\text{oo}}$. At this depth the crystals were orderly and oriented with horizontal c-axis, and a horizontal section, cut perpendicular to the orientation of the crystals and platelets includes many boundaries. The sample was frozen on a glass plate and further thinned using a bandsaw; finally its surface was polished. To minimize brine drainage from the sample the preparation was performed at a temperature of -25°C . Finally water was frozen around the periphery of the sample to seal the edges, inhibiting brine drainage. The sample was placed under the microscope and warmed over a period of two days. The procedure was to increase the air temperature, allow the ice to attain thermal equilibrium, photograph the sample, and repeat the process. This was done at fourteen temperatures between -27°C and -1°C .

Four microphotographs, taken at temperatures of -27 , -7 , -4 , and -1°C are presented in Figure 4.29 a-d. Arrows are used to follow the evolution of representative features as the brine volume increases with temperature. The thin dark lines between platelets in Figure 4.29A



Figure 4.29: Microphotographs of a horizontal thin section: (A) -27°C ; (B) -7°C ; (C) -4°C ; and (D) -1°C . The double arrow in Figure 4.29A is 1 mm in length. **A**







are due to the precipitated salts. These lines do not appear in the photographs (B, C, and D) taken above the eutectic point.

The microscope observations illustrate several points regarding changes in ice structure during warming. As the brine volume increases, the platelet boundaries become broader and smoother. Small isolated pockets of brine enlarge and sometimes connect. Similarly, small air bubbles, released within the ice by melting often join together. These changes all tend to reduce the amount of scattering within the ice, and thus reduce the albedo and the extinction coefficient.

To avoid confusion when examining the effects of brine volume on the optical properties, the influences of warming and growth rate must be distinguished. For two ice sheets, grown at different rates and brought to the same temperature, the faster grown saltier ice will have a larger brine volume; but, since it has a greater number of brine inclusions, scattering is greater and the albedo and extinction coefficient larger. Dichotomies regarding the relationship between brine volume and the optical properties are resolved by careful consideration not only of the brine volume, but of the brine distribution.

CHAPTER FIVE

FOUR STREAM MODELING

5.1 INTRODUCTION

To this point the optical properties of sea ice have been examined using a Dunkle and Bevans photometric model. To introduce realistic scattering functions and investigate the physics of the radiative transfer the four stream DOM model was used to examine the influence of $\bar{\omega}_0$, optical depth, and phase function on albedo and transmittance. Experimental results were fitted by one or two layer models. Using suitable values for the optical parameters the effects of wavelength, ice thickness, incident radiation field, and refraction were determined.

Calculations, for the most part, were performed at 650 nm. This particular wavelength was selected since the spectrophotometer had a large signal to noise ratio and reasonably high resolution. In addition, it was possible to use phase functions obtained from preliminary results of scattering experiments conducted with a HeNe laser (Grenfell and Hedrick, personal communication, 1978). In a few cases the results at 650 nm were extended to calculate spectral albedos and transmittances from 400 to 1000 nm. Except for the direct beam cases discussed in Section 5.4, an isotropic incident radiation field was used for all calculations.

5.2 PARAMETER STUDY

5.2.1 Parameters of the Discrete Ordinates Method

The parameters of the discrete ordinates method are five quantities: the single scattering albedo ($\tilde{\omega}_0$), the optical depth (τ_N), the scattering coefficient (σ), the absorption coefficient (k), and the depth (H), which are related by Equations (2.18) and (2.22). The phase function [$p(\theta)$] and the incident radiation field must also be specified to calculate radiances and irradiances as a function of depth.

Although k , σ , and H are the fundamental physical properties of the medium, it is often more convenient to discuss $\tilde{\omega}_0$ and τ_N , which are the explicit parameters appearing in the theory. In practice, the absorption coefficient and thickness are known, an appropriate $\tilde{\omega}_0$ is selected, and τ_N is calculated. Optical thickness and physical thickness are related by

$$\tau_N = \frac{kH}{1-\tilde{\omega}_0} \quad (5.1)$$

This relationship holds true at any depth within the ice. For a particular value of $\tilde{\omega}_0$ physical and optical thickness are linearly related, with the slope increasing for larger $\tilde{\omega}_0$ (Figure 5.1a). For the four values of $\tilde{\omega}_0$ illustrated, .97, .98, .99, and .995, an optical thickness of one corresponds to a physical thickness of 9.38, 6.25, 3.13, and 1.56 cm respectively. Figure 5.1b shows the steepening increase in τ_N with increasing $\tilde{\omega}_0$ at a given physical thickness. Figure 5.1 is useful in relating the perceptual physical thickness of the ice to the conceptual optical thickness of the model.

Sea ice, being a medium dominated by scattering, has large values of $\tilde{\omega}_0$. For the salt ice studied in the tank experiments, $\tilde{\omega}_0$ typically

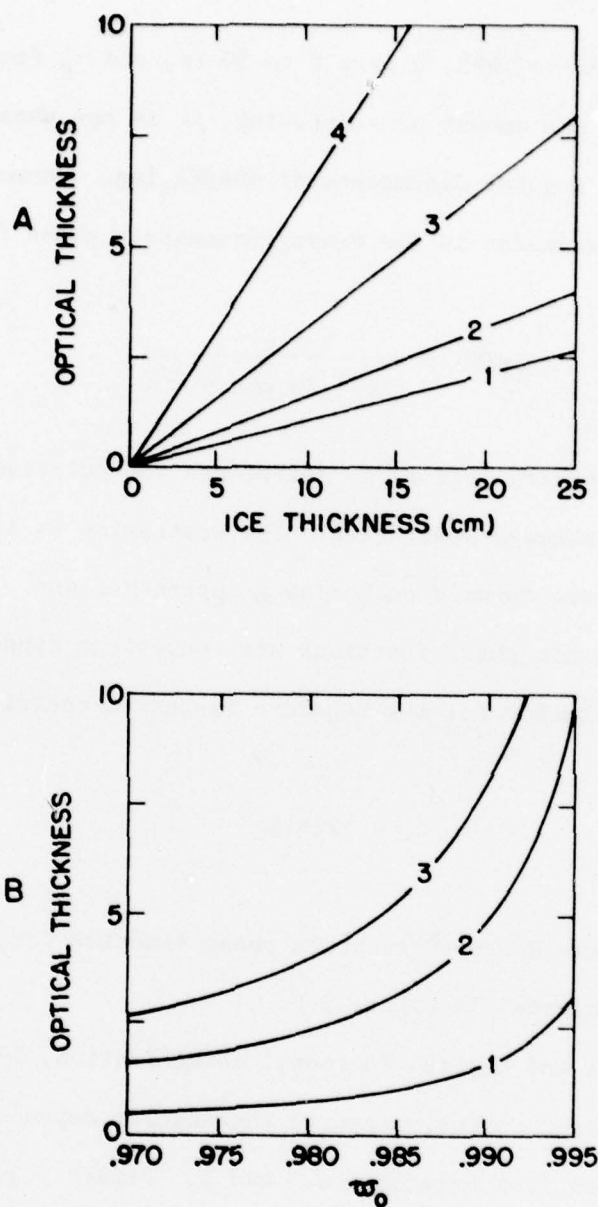


Figure 5.1: Interrelation between single scattering albedo ($\tilde{\omega}_0$), optical thickness (τ_N), and physical (ice) thickness (H) ($k = .0032 \text{ cm}^{-1}$). (A) Physical thickness versus optical thickness for constant values of $\tilde{\omega}_0$: (1) $\tilde{\omega}_0 = .97$; (2) $\tilde{\omega}_0 = .98$; (3) $\tilde{\omega}_0 = .99$; and (4) $\tilde{\omega}_0 = .995$. (B) Optical thickness versus $\tilde{\omega}_0$ for constant values of H : (1) $H = 5$ cm; (2) $H = 15$ cm; and (3) $H = 25$ cm.

ranged from .95 to .995, H from 0 to 30 cm, and τ_N from 0 to 19. While $\bar{\omega}_0$ determines the amount of scattering, it is the phase function which specifies the angular dependence of scattering. Commonly used in studies of radiative transfer is the Henyey-Greenstein phase function

$$p(\theta) = \frac{1 - g^2}{(1 + g^2 - 2g \cos \theta)^{3/2}} \quad (5.2)$$

where the asymmetry factor, g , determines the relative importance of forward and backward scattering. The scattering is isotropic for $g = 0$ and becomes more forward peaked as g approaches one. Mathematically Henyey-Greenstein phase functions are convenient since they yield a simple relationship for the Legendre expansion coefficients

$$\bar{\omega}_\ell = (2\ell + 1)g^\ell \quad (5.3)$$

Examples of the Henyey-Greenstein phase function for g equal to 0, .5, and .75 are plotted in Figure 5.2.

Grenfell and Hedrick (personal communication, 1978), using a HeNe laser as a light source, measured the angular dependence of scattering by ice samples from Experiments 3 and 4. Figure 5.3, Curve 1 is an eyeballed best fit of their preliminary results. The importance of backscattering is indicated by the increase of the phase function for angles larger than 105° . Because of this increase, a one parameter Henyey-Greenstein phase function was insufficient to describe the scattering. Used instead was a three parameter Henyey-Greenstein phase function of the form

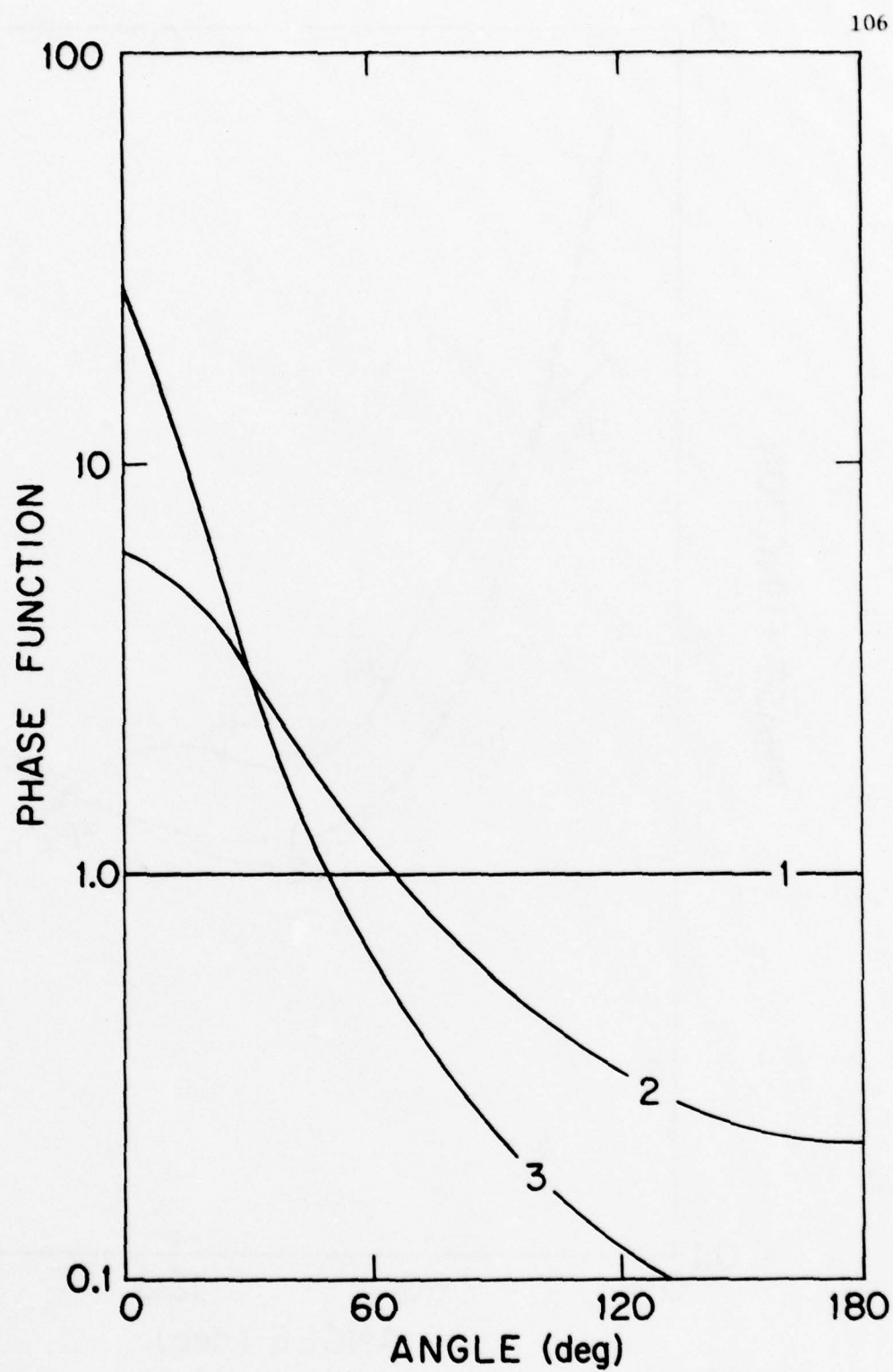


Figure 5.2: Selected phase functions: (1) isotropic; (2) Henyey-Greenstein, $g = .5$; and (3) Henyey-Greenstein, $g = .75$.

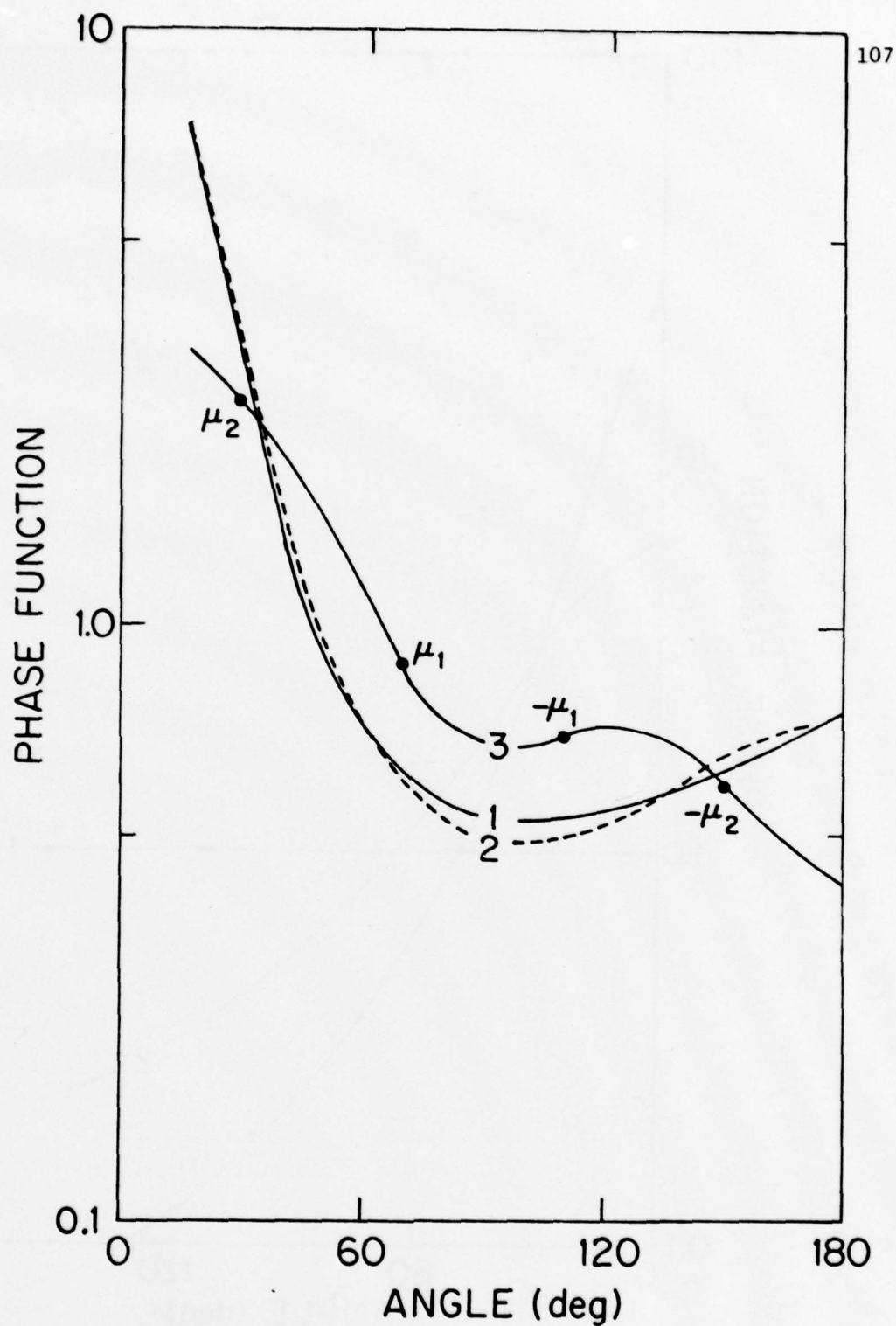


Figure 5.3: Phase function determination for scattering experiment results (Grenfell and Hedrick, personal communication): (1) experimental results; (2) best fit using a three parameter Henyey-Greenstein phase function; and (3) phase function calculated using $\tilde{\omega}_\ell$'s and Equation 2.21.

$$p(\theta) = (1-\gamma) \frac{1-g_1^2}{(1+g_1^2-2g_1 \cos \theta)^{3/2}} + \gamma \frac{1-g_2^2}{(1+g_2^2-2g_2 \cos \theta)^{3/2}}, \quad (5.4)$$

where the second term enhances the backscattering ($g_2 < 0$) and γ is the weighting factor. A nonlinear regression routine using data digitized at fifteen degree intervals was used to determine the three coefficients. Best fit coefficients of $\gamma = .279$, $g_1 = .71$, and $g_2 = -.25$ were substituted into Equation (5.4), which was plotted as Curve 2. Introducing this phase function into Equation (2.23), the associated $\tilde{\omega}_\ell$'s were determined by numerical integration, then substituted into Equation (2.21) to obtain Curve 3. The four term expansion of this phase function is quite good at $\pm\mu_2$ and, though less precise at $\pm\mu_1$, is accurate for calculations of irradiance.

5.2.2 Sensitivity of Albedo and Transmittance to the DOM Parameters

The Phase Function

Using the single parameter Henyey-Greenstein phase function described by Equation (5.2), albedos and transmittances were calculated over a range of g 's. Values at 650 nm for ice 20 cm thick and various $\tilde{\omega}_0$'s are plotted in Figure 5.4. The largest albedos and smallest transmittances are produced by isotropic scattering ($g = 0$). As the asymmetry factor (g) increases, and the scattering becomes more forward peaked, the albedo decreases and the transmittance increases.

Thickness and Single Scattering Albedo

Isopleths of albedo and transmittance for pertinent ranges of $\tilde{\omega}_0$ and H are plotted in Figures 5.5 and 5.6. The calculations were

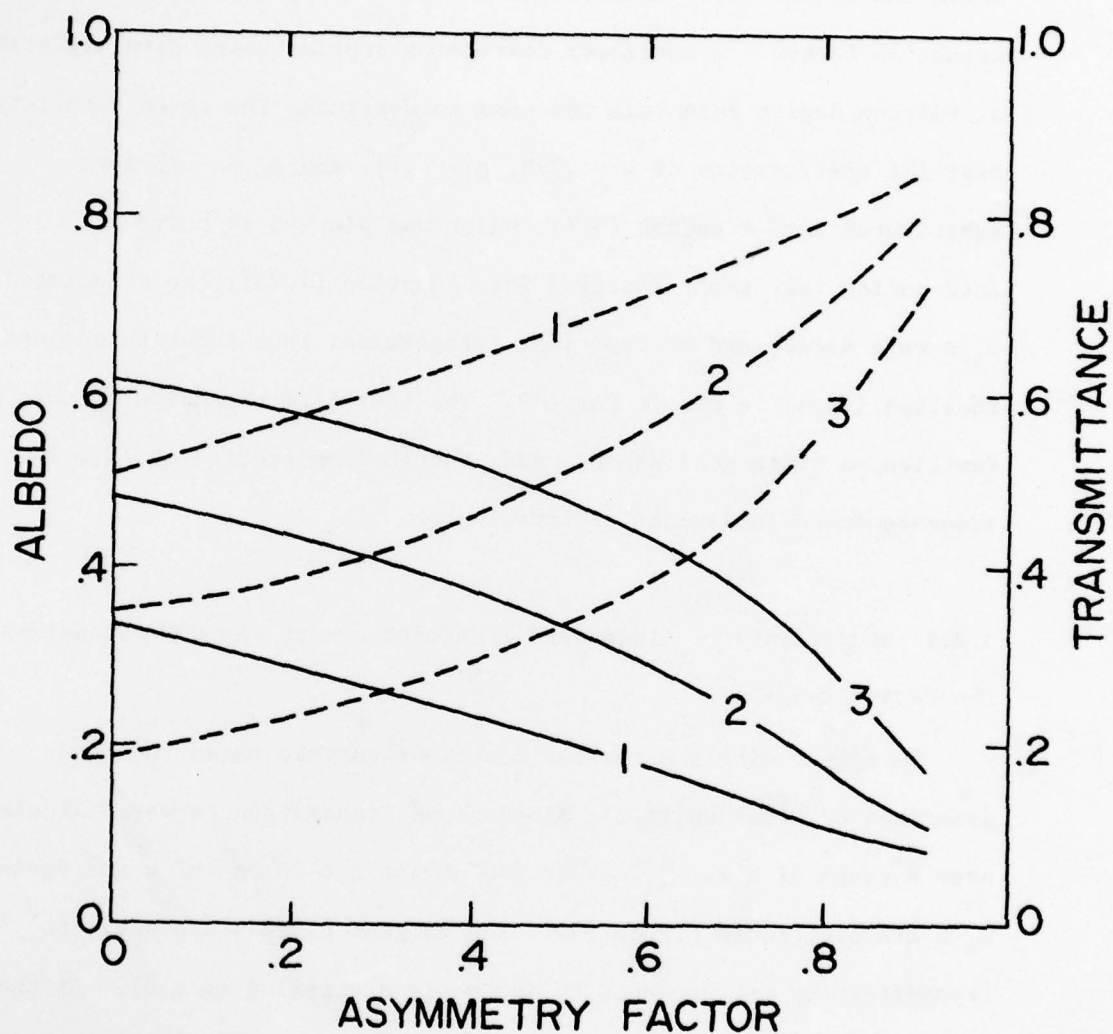


Figure 5.4: Effect of asymmetry parameter g on albedo (—) and transmittance (----). Calculations are for ice 20 cm thick at a wavelength of 650 nm using the three parameter Henyey-Greenstein phase function with diffuse incident radiation: (1) $\bar{\omega}_0 = .96$; (2) $\bar{\omega}_0 = .98$; and (3) $\bar{\omega}_0 = .99$.

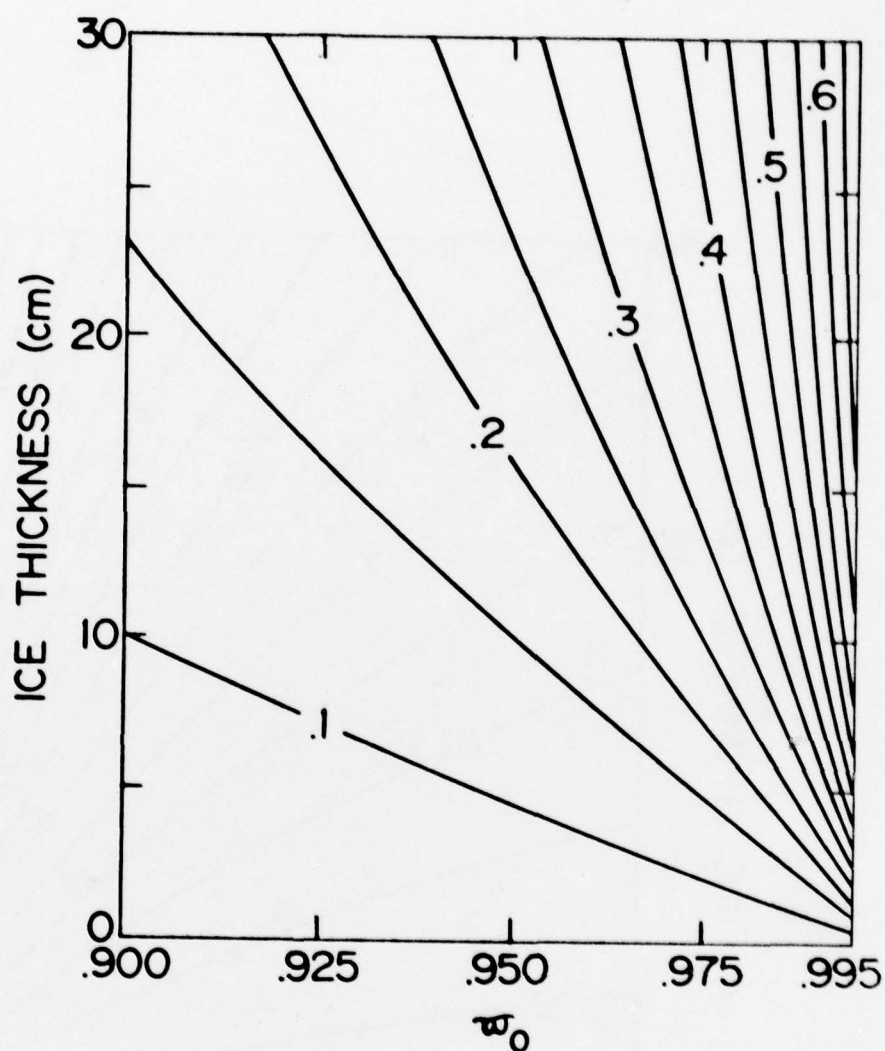


Figure 5.5: Isopleths of albedo as a function of w_0 and ice thickness, calculated at 650 nm using a three parameter Henyey-Greenstein phase function with diffuse incident radiation.

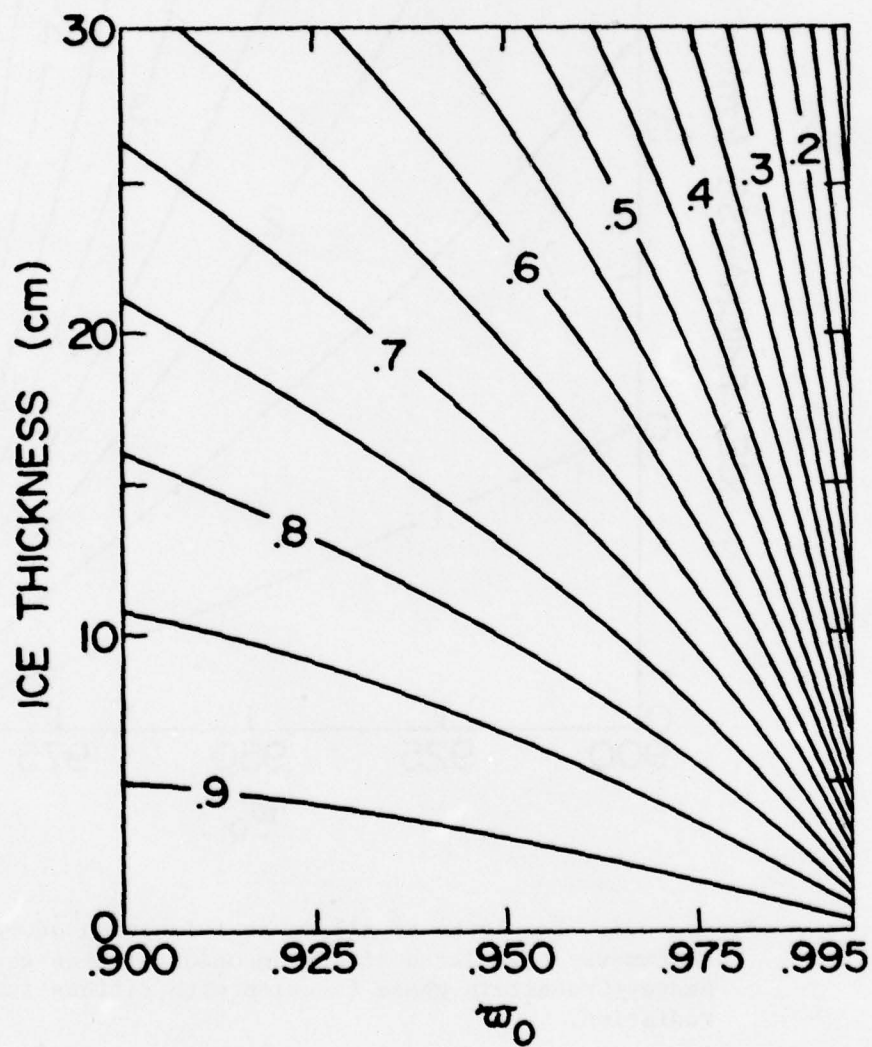


Figure 5.6: Isopleths of transmittance as a function of \tilde{w}_0 and ice thickness, calculated at 650 nm using a three parameter Henyey-Greenstein phase function with diffuse incident radiation.

performed at 650 nm using the three parameter Henyey-Greenstein phase function. For a given $\tilde{\omega}_0$, as the ice thickness increases, the albedo increases and the transmittance decreases. Similarly, holding ice thickness constant while increasing $\tilde{\omega}_0$ effects an increase in albedo and a decrease in transmittance. As $\tilde{\omega}_0$ increases albedo and transmittance become more sensitive to changes in either $\tilde{\omega}_0$ or H .

The Effects of Refraction

Using an appropriate phase function [Equation (5.4)] and reasonable values for $\tilde{\omega}_0$ and depth, albedos and transmittances for both nonrefracting and refracting media were calculated under direct beam and diffuse incident conditions. The angle of the direct beam was representative for arctic summer conditions. As illustrated in Table 5.1, in all cases, refraction caused a decrease in albedo and an increase in transmittance. In the case of refraction a portion of the upwelling light at the interface is totally internally reflected downwards into the medium, thus decreasing the albedo and increasing the transmittance. Refraction converges the incident radiation into a more normal direction also increasing transmission.

5.3 COMPARISON OF THEORETICAL AND EXPERIMENTAL ALBEDOS AND TRANSMITTANCES

AT 650 nm

5.3.1 One Layer Model

The four stream model was tested using results from the tank experiments. While ice thickness data were available for each experimental site, single scattering albedos and phase functions are unknown.

TABLE 5.1
Effects of Refraction on Albedo and Transmittance

z=25 cm	DIFFUSE INCIDENT			DIRECT BEAM $\mu_0 = .423$ ($\theta = 65^\circ$)		
	No Refraction	Refraction	Percent Difference	No Refraction	Refraction	Percent Difference
$\bar{\omega}_0 = .97, \tau_N = 2.67$						
Albedo	.534	.362	-.322	.599	.397	-.337
Transmittance	.330	.449	.361	.264	.409	.549
$\bar{\omega}_0 = .98, \tau_N = 4.0$						
Albedo	.619	.447	-.278	.674	.479	-.289
Transmittance	.247	.347	.405	.199	.317	.593
$\bar{\omega}_0 = .99, \tau_N = 8.0$						
Albedo	.739	.581	-.214	.778	.605	-.222
Transmittance	.133	.197	.481	.108	.181	.676

The three parameter Henyey-Greenstein phase function [Equation (5.4)] discussed in Section 5.2.1 was assumed to describe the angular scattering for all cases. Values of $\bar{\omega}_0$ were determined using an inverse procedure. For a particular experimental site $\bar{\omega}_0$ was selected so that the albedo calculated using the four stream model was equal to the experimental albedo. The analysis was done at a wavelength of 650 nm. In order to compensate for the effects of instrumental bandwidth on the results, an absorption coefficient of $.0042 \text{ cm}^{-1}$ was used rather than the reported value at 650 nm of $.0032 \text{ cm}^{-1}$ (Sauberer, 1950). This value of $.0042 \text{ cm}^{-1}$ was determined by convolving a typical spectral transmission curve with the bandpass of the instrument.

This technique applied to data from eleven experimental sites and the results summarized in Table 5.2. Theoretical and experimental albedos were matched quite well by values of $\bar{\omega}_0$ ranging from .955 to .9997. However, agreement between theoretical and experimental transmittances is not as good. In all cases except two, the theoretical transmittance is larger than the experimental, with differences ranging from 6 to 55%.

There are a number of possible explanations for the lack of agreement between theoretical and experimental transmittances. The assumption of homogeneous ice, implicit in a one layer model, is probably the source of error in the theoretical calculations. Temperature gradients, changes in growth rates, and differences in crystal orientation can all cause vertical variations in the physical state of the ice, which affect the optical properties. In addition, changes in the ice surface strongly influence the albedo and transmittance. Table 5.2 indicates that the

Table 5.2
One Layer, Four Stream Modeling of Experimental Results

CONDITIONS			EXPERIMENTAL		THEORETICAL			Percent Difference in T_{650}	
Experiment	Air Tempera- ture	Ice Thick- ness (cm)	Trans- mitted Probe Depth	α_{650}	T_{650} *	$\bar{\omega}_0$	α_{650}		T_{650} *
6	-35	26.0	19.0	.959	.053	.9997	.866	.000	—
5	-30	23.9	19.4	.587	.147	.989	.583	.326	55
6	-22	28.0	19.0	.564	.229	.987	.566	.429	30
5	-20	29.2	19.4	.440	.336	.973	.439	.562	40
4	-20	21.6	18.5	.456	.260	.979	.454	.444	41
3	-10	27.2	19.3	.391	.375	.968	.397	.577	35
3	-10	21.1	19.3	.394	.434	.9737	.391	.466	7
3	-10	11.7	19.3	.333	.581	.9763	.330	.547	-6
5	0	29.0	19.4	.423	.540	.971	.424	.573	6
6	0	29.0	19.0	.582	.288	.988	.581	.424	32
3	0	28.4	19.3	.336	.497	.955	.334	.648	23

*Transmittance at probe

closest agreement between theoretical and experimental transmittances occurs when the ice is most nearly homogeneous. The difference is smallest for thin ice and warm ice. Conversely, the largest differences are exhibited for the very inhomogeneous, cold, fast grown ice. A one layer model thus appears to be inadequate for describing the transfer of radiation in vertically complex ice.

5.3.2 Two Layer Model

In an effort to obtain better agreement between theoretical and experimental results, a two layer model was formulated. Aside from the boundary conditions the theoretical development of a two layer model was the same as the one layer model. To calculate the constants of integration, L_j 's, in a two layer model, a system of eight equations and eight unknowns must be solved. The four additional boundary conditions are determined by requiring continuity of radiance at the interface between the two layers

$$I_1(-\mu_1, \tau_1) = I_2(-\mu_1, \tau_1) \quad (5.5)$$

$$I_1(-\mu_2, \tau_1) = I_2(-\mu_2, \tau_1) \quad (5.6)$$

$$I_1(\mu_1, \tau_1) = I_2(\mu_1, \tau_1) \quad (5.7)$$

$$I_1(\mu_2, \tau_1) = I_2(\mu_2, \tau_1) \quad (5.8)$$

where τ_1 is the optical depth of layer one and I_1 and I_2 are the radiances in layers one and two.

The two layer model was applied to the results from Experiments 5 and 6. The two cases selected had the largest temperature gradients

and were poorly represented by the one layer model. This is particularly true of Experiment 6, where a few centimeter thick surface layer was below the eutectic point, resulting in a region containing precipitated salts which was very different in appearance from the underlying ice.

Using realistic values of $\bar{\omega}_0$ and layer thickness a range of two layer cases were examined. The two which best represent the experimental results are summarized in Table 5.3. While the agreement between experimental and theoretical results is closer for a two layer model, substantial differences still remain.

Table 5.3

Two Layer, Four Stream Modeling of Cold Ice

Experiment	Air Temp °C	LAYER 1		LAYER 2		THEORETICAL		EXPERIMENTAL	
		$\bar{\omega}_0$	Thickness (cm)	$\bar{\omega}_0$	Thickness (cm)	α	T^*	α	T^*
6	-37	.99993	2.0	.97	24.0	.898	.018	.959	.002
5	-30	.992	11.0	.98	13.0	.599	.282	.587	.147

*Transmitted at 19 cm.

A more detailed four stream analysis of the experimental results is not warranted until better data concerning values of the single scattering albedo and the phase function become available. Experiments explicitly measuring $\bar{\omega}_0$ and the phase function for a variety of ice types and conditions are necessary. Only then can multilayered models, accurately representing ice surface and interior conditions, be implemented.

5.4 FURTHER APPLICATIONS OF THE FOUR STREAM MODEL

Modeling of the experimental results indicates that for the three parameter Henyey Greenstein phase function and [Equation (5.4)], $\bar{\omega}_0$ ranges from .955 for warm slowly grown ice to as high as .99993 for ice below the eutectic point. Using appropriate parameter values the four stream model is now extended to theoretically investigate additional topics.

5.4.1 Depth Dependence of Irradiance

Though the focus of the four stream modeling has been on the calculation of albedos and transmittances, depth dependent upwelling, downwelling, and net irradiances can also be determined. Figures 5.7 and 5.8 illustrate normalized downwelling and net irradiance as a function of depth at 650 nm. The irradiances were calculated for a single layered ice slab, 25 cm thick, under diffuse illumination using a three parameter Henyey-Greenstein phase function and values of single scattering albedo of .97, .98, and .99. Evident from Figure 5.7 is a decrease in downwelling irradiance with depth, a decrease which becomes more pronounced as $\bar{\omega}_0$ increases. In addition, for a given $\bar{\omega}_0$ the slope of $F_{\downarrow}(z)$ becomes steeper with depth ($d^2F_{\downarrow}(z)/dz^2 < 0$). The slope of the net irradiance, the important quantity when considering the energy absorbed in the ice, decreases as depth increases. In general, the extinction coefficient is expressed as

$$\kappa = \frac{1}{F_z} \frac{dF_z}{dz} = \frac{d(\ln F_z)}{dz} \quad , \quad (5.9)$$

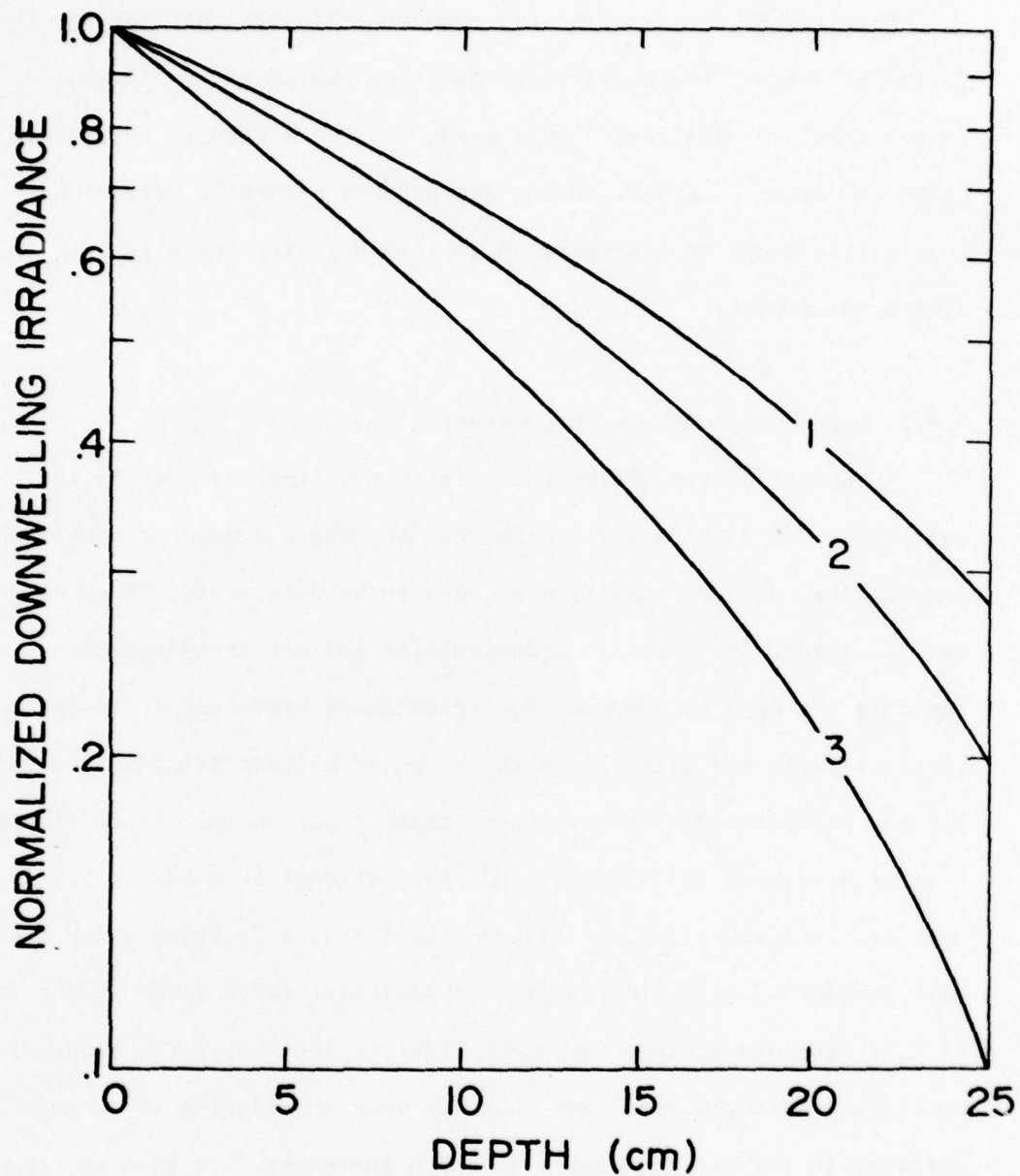


Figure 5.7: Normalized downwelling irradiance at 650 nm as a function of depth for: (1) $\omega_0 = .97$; (2) $\omega_0 = .98$; and (3) $\omega_0 = .99$. Calculations were performed for diffuse incident radiation using the three parameter Henyey-Greenstein phase function.

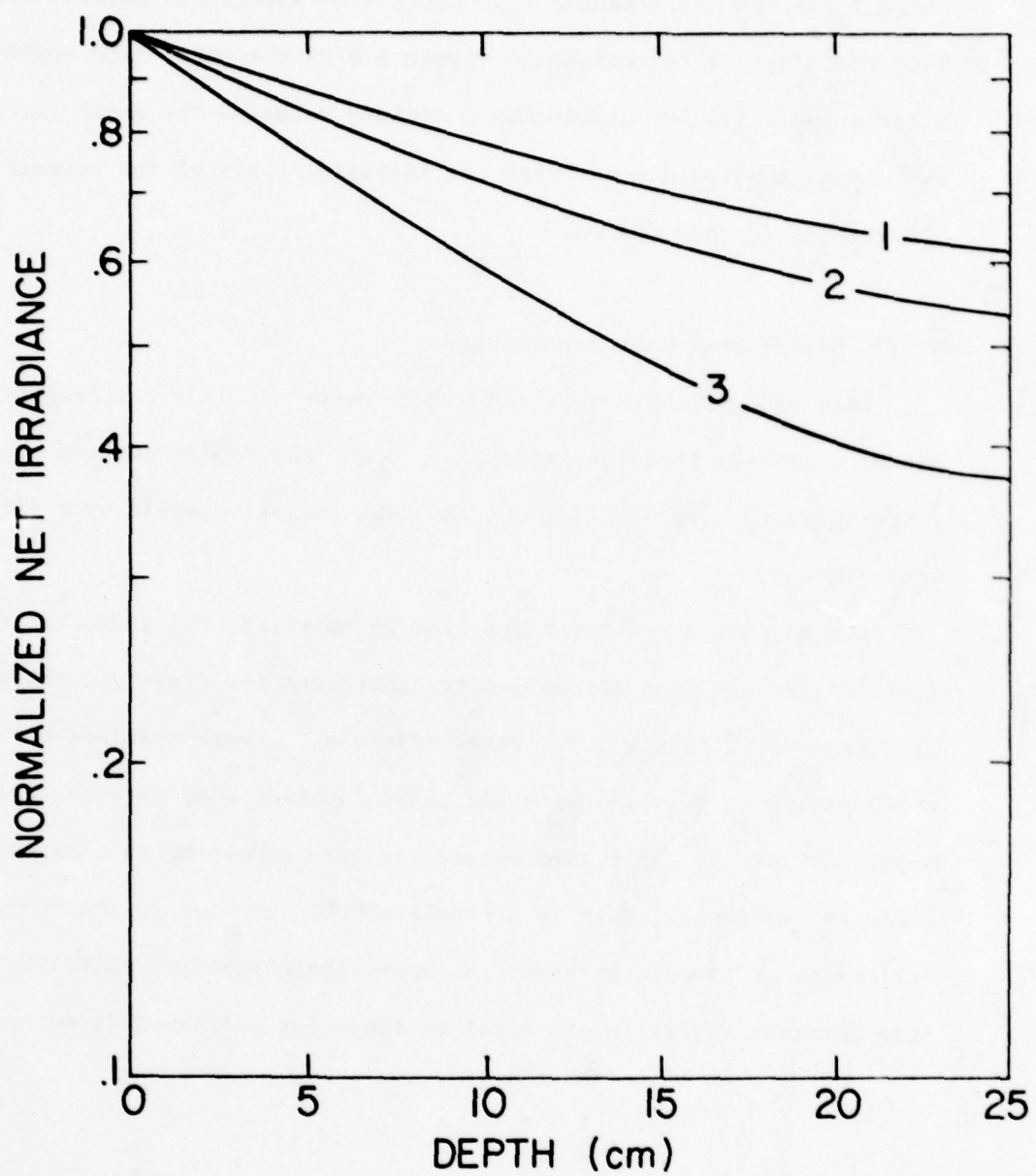


Figure 5.8: Normalized net irradiance at 650 nm as a function of depth for: (1) $\bar{\omega}_0 = .97$; (2) $\bar{\omega}_0 = .98$; and (3) $\bar{\omega}_0 = .99$. The three parameter Henyey-Greenstein phase function was used and the incident radiation field was diffuse.

where F_z is the net irradiance at depth z (Grenfell and Maykut, 1978). Thus the slope of the curves in Figure 5.8 is the extinction coefficient, which asymptotically approaches a minimum value as the depth increases. The changing slope demonstrates the inapplicability of the Bouguer-Lambert law in this region.

5.4.2 Direct Beam Incident Radiation

When using the discrete ordinates method it is not necessary to assume isotropic incident radiation. Clear sky conditions can also be investigated by representing the incident radiation field by a direct beam at $-\mu_0$.

Considering a one layer ice slab 25 cm thick, the effect of the angle of incidence on albedo and transmittance for clear sky conditions is displayed in Figure 5.9. Three values of $\bar{\omega}_0$ were examined with a three parameter Henyey-Greenstein phase function used in each case. Beyond 60° albedo and transmittance are very sensitive to changes in the angle of incidence. This is a result of the increase in the Fresnel reflection of the direct beam. At approximately 54° , results for direct beam incident radiation are equal to those for diffuse incident radiation.

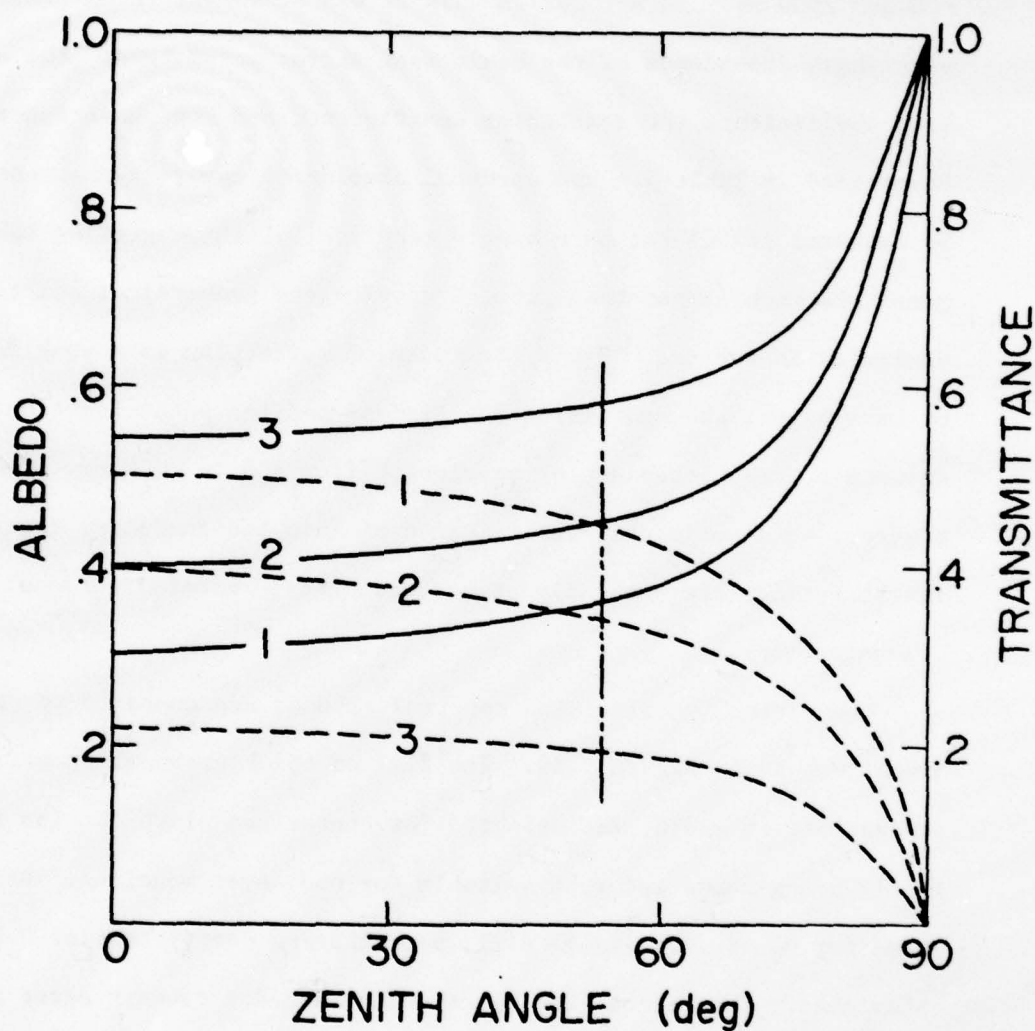


Figure 5.9: Albedo (—) and transmittance (----) as a function of solar angle (angle of direct incident beam) for: (1) $\bar{\omega}_0 = .97$; (2) $\bar{\omega}_0 = .98$; and (3) $\bar{\omega}_0 = .99$ (values for isotropic incident). The three parameter Henyey-Greenstein phase function was used in cloudy sky results.

5.4.3 Spectral Albedos and Transmittances

By using a modified version of the four stream model spectral albedos and transmittances were calculated at 50 nm intervals between 400 and 1000 nm. To accomplish this it was necessary to determine the wavelength dependence of the basic four stream parameters: the absorption coefficient, the scattering coefficient, and the phase function. Summarized in Table 5.4 are spectral absorption coefficients measured by Sauberer (1950) for pure bubble free ice. With scattering inhomogeneities much larger than optical wavelengths geometrical scattering dominates in sea ice. Since the index of refraction is a weak function of wavelength, the scattering coefficient and the phase function are assumed to be independent of wavelength from 400 to 1000 nm. There is, however, no experimental verification of this independence, though investigations are presently being conducted (Grenfell, personal communication).

Theoretically calculated spectral albedos are compared to experimental values in Figure 5.10. Ice 21.1 cm thick grown at an air temperature of -10°C , was selected for comparison since the ice is fairly homogeneous and thus suitable for one layer modeling. Using a value for $\bar{\omega}_0$ of .974 (Table 5.2), a scattering coefficient of 0.119 is calculated. Theoretical and experimental albedos closely agree below 800 nm, but above this experimental values are somewhat higher. The disagreement in this region is probably due to the wide bandpass of the instrument.

The magnitude and spectral dependence of albedo and transmittance are markedly influenced by ice thickness. Using a scattering coefficient of $.157\text{ cm}^{-1}$, which at 650 nm corresponds to a $\bar{\omega}_0$ of .98, spectral

Table 5.4
Absorption Coefficients of Ice
(Sauberer, 1950)

λ (nm)	k (cm ⁻¹)
400	.0003
450	.0005
500	.0008
550	.0013
600	.0020
650	.0032
700	.0060
750	.0110
800	.0200
850	.0330
900	.0590
950	.1050
1000	.2500

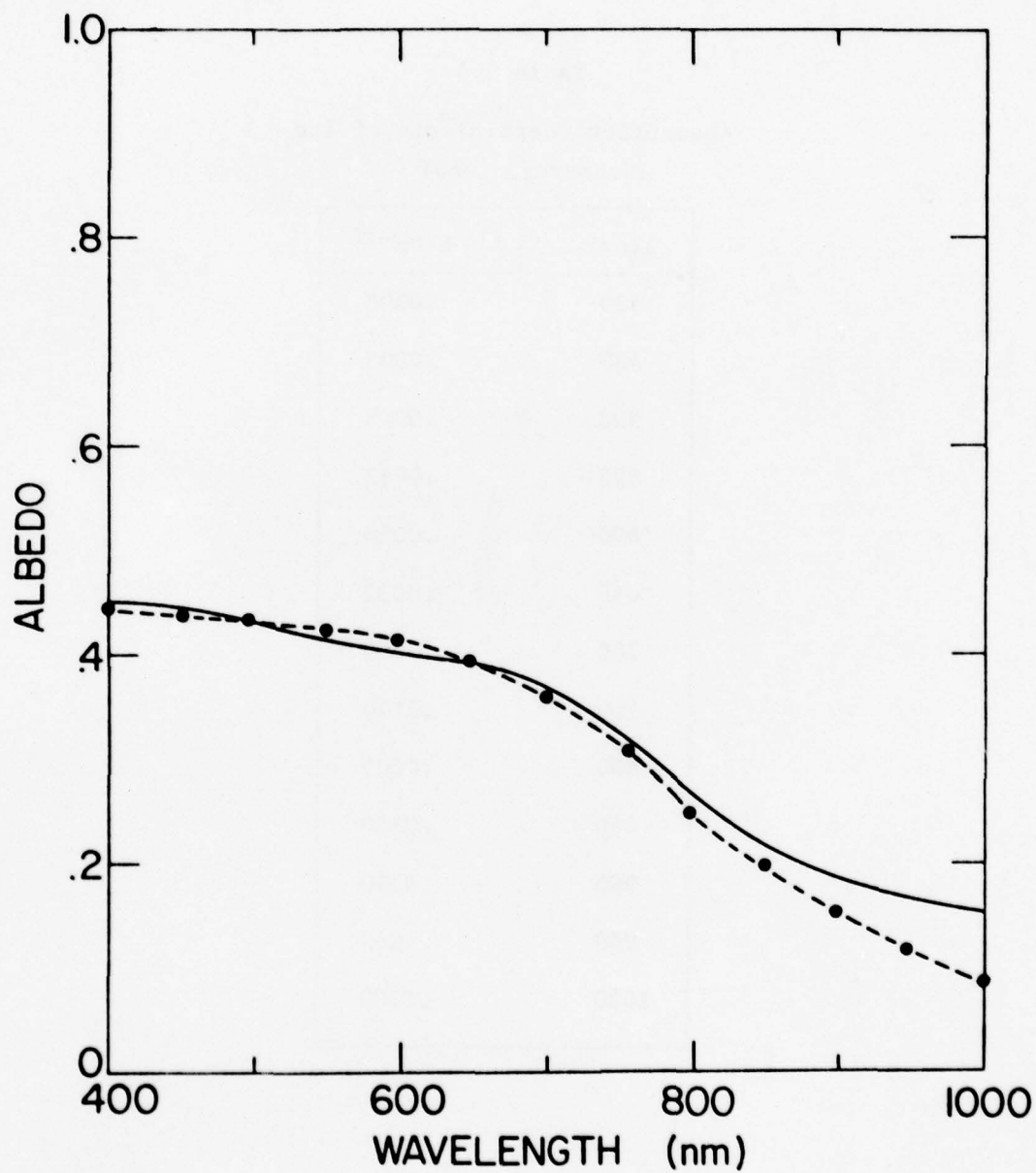


Figure 5.10: Comparison of spectral albedos for ice 21 cm thick at an air temperature of -10°C : (—) experimental and (----) theoretical. Theoretical calculations used the three parameter Henyey-Greenstein phase function and diffuse incident conditions.

albedos (Figure 5.11) and transmittances (Figure 5.12) were calculated for ice ranging in thickness from 5 to 25 cm. As the ice thickens, the increase in albedo is greater at shorter wavelengths where $\bar{\omega}_0$ is larger. This results in a wavelength dependence for albedo which is weak for thin ice and becomes more pronounced as the thickness increases. The transmittance sharply decreases at longer wavelengths and as the ice thickness increases, narrowing the spectrum of transmitted light.

The spectral albedo of an ice cover is affected by the nature of the surface layer. To investigate the extent of this effect spectral albedos for a two layer model are calculated. Five different cases were studied (Figure 5.13). Curve 3 represents 25 cm thick ice with a scattering coefficient of .157. In Curves 1 and 2 the top five and one centimeters of ice were replaced by water of negligible scattering coefficient. It was assumed that the water layer did not change the scattering properties of the underlying ice. This is somewhat idealized since the scattering due to the surface irregularities of the ice is reduced by the presence of water. Curves 4 and 5 demonstrate the effect of highly scattering ($\sigma = 3.997 \text{ cm}^{-1}$), one and five centimeter thick surface layers, representative of ice below the eutectic point.

The presence of a surface water layer decreases the albedo while the albedo is enhanced by a surface scattering layer. The thicker the surface layer the more pronounced the effect. The influence of a surface scattering layer is dependent on wavelength, as is displayed by the change in shape of the spectral albedo curve. As has been indicated earlier (Figures 5.5 and 5.11), the thickness of ice significantly contributing to the albedo decreases with $\bar{\omega}_0$ (for the limiting case of

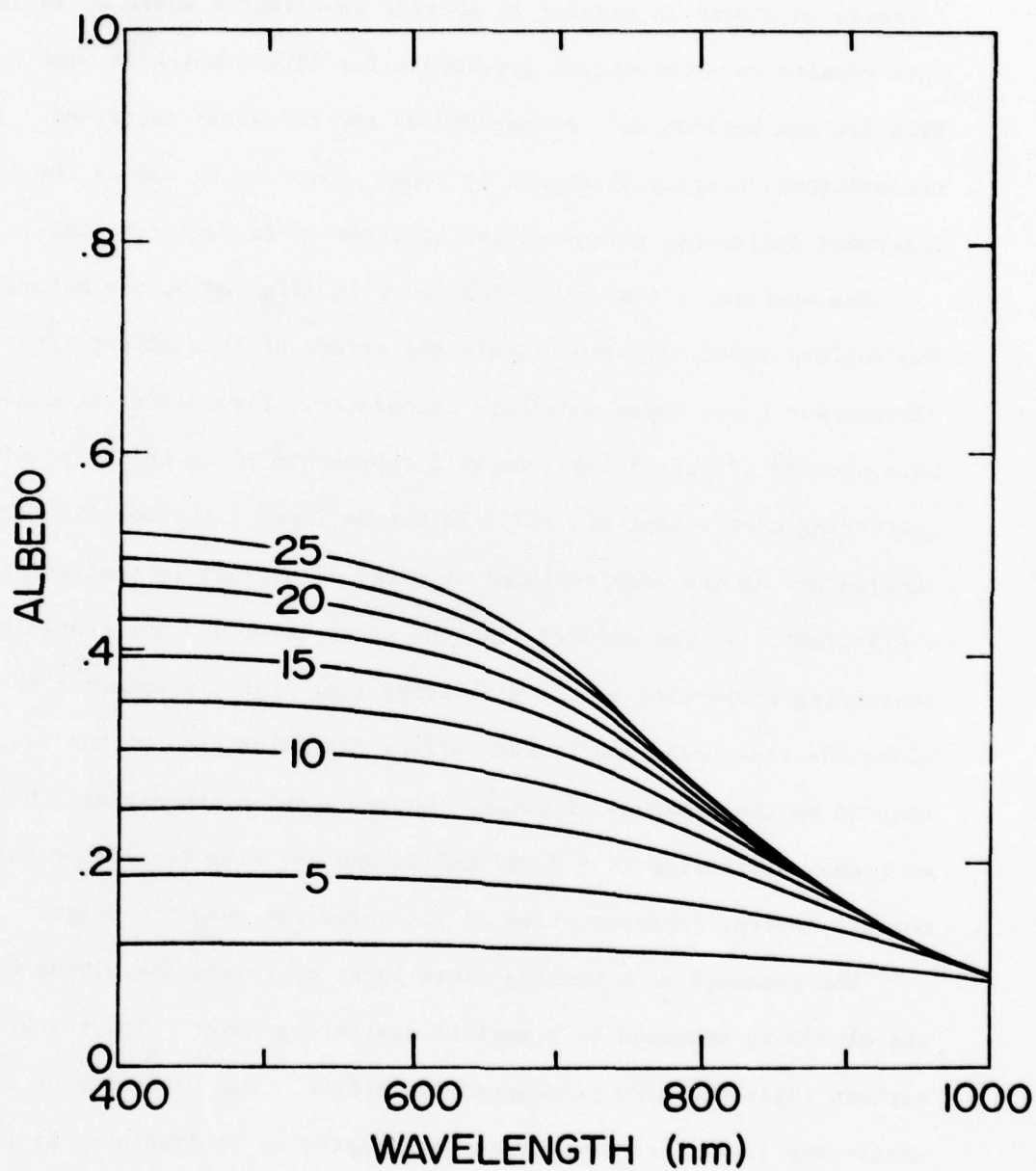


Figure 5.11: Spectral albedos calculated for ice ranging in thickness from 2.5 to 25 cm using a scattering coefficient of .157. The three parameter Henyey-Greenstein phase function and diffuse incident conditions were used.

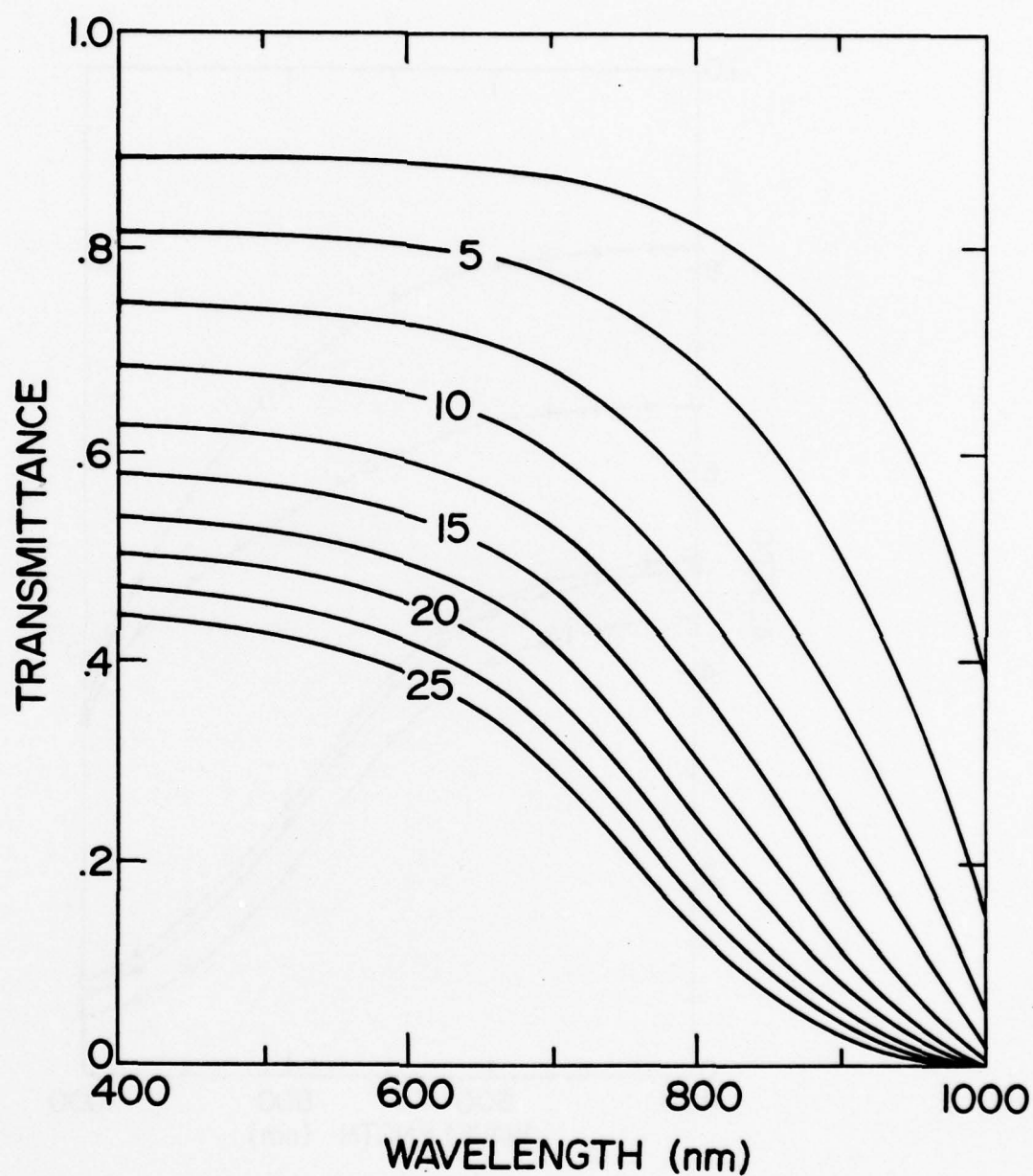


Figure 5.12: Spectral transmittances calculated for ice ranging in thickness from 2.5 to 25 cm using a scattering coefficient of .157. The three parameter Henyey-Greenstein phase function and diffuse incident radiation were used.

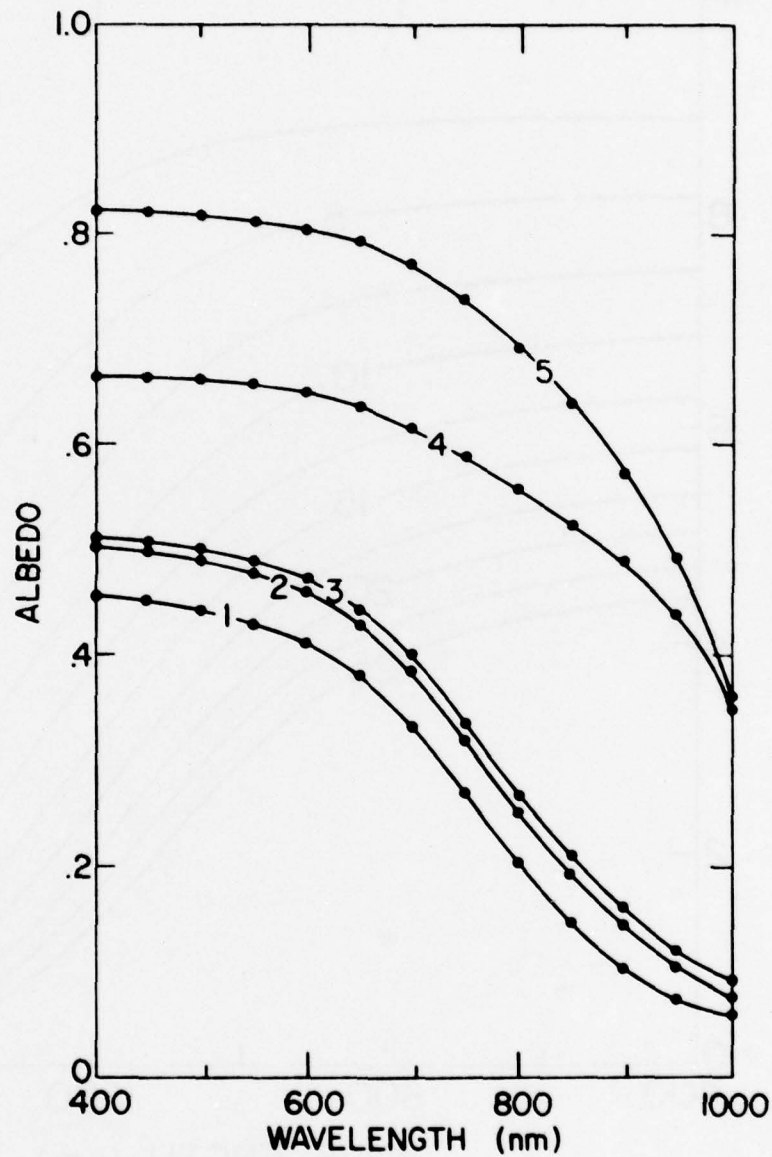


Figure 5.13: Effect of surface layer on albedo. The total thickness is 25 cm and the scattering coefficient for the underlying ice is .157: (1) 5 cm thick surface water layer; (2) 1 cm thick surface water layer; (3) no surface layer; (4) 1 cm thick surface scattering layer ($\sigma = 3.997$); and (5) 5 cm thick surface scattering layer ($\sigma = 3.997$). Diffuse incident conditions and the three parameter Henyey-Greenstein phase function were used.

$\tilde{\omega}_0 = 0$ the albedo is due only to specular reflection). Therefore the albedo at longer wavelengths, with larger absorption coefficients, is more sensitive to surface conditions.

CHAPTER SIX

SUMMARY AND SUGGESTIONS FOR FUTURE RESEARCH

The optical properties of cold, young ice are markedly different from those of melting first-year ice and older multiyear ice. In particular, extinction coefficients can be as much as 15 times larger. Under cold conditions albedos for thin ice (25 cm) are comparable to values for older, thicker ice.

While these experiments do not allow a quantitative statement of relationships between the optical properties and the physical parameters of the ice, some generalizations can be made. For young growing ice the albedo increases as the ice thickens. The albedo is quite sensitive to ice surface conditions, with a crumbly surface causing an increase in albedo, a water skim a decrease, and the presence of solid salts a dramatic increase to values comparable to snow. When comparing ice of similar temperature profiles and thicknesses, but with different growth histories, the faster grown ice has larger albedos and extinction coefficients. Over the range of salinities investigated (4 ‰ to 14 ‰) ice salinity does not discernibly influence the optical properties. As the temperature of the ice decreases, its albedo and extinction coefficient increase. When the ice temperature drops below the eutectic point the increase is discontinuous and dramatic due to the presence of precipitated salts. The brine volume of the ice changes with temperature and thus is related to the optical properties. When comparing brine volumes of ice grown under different conditions, the influence of brine volume is less clear since other parameters such as growth rate are also

significant. It is important to consider the distribution of brine as well as the brine volume when relating it to the optical properties.

Changes in ice structure which enhance scattering result in increased albedos and extinction coefficients. A crumbly surface with many air-ice interfaces is highly scattering, while a water skim with water-ice interfaces is not. With an index of refraction of 1.52 and small dendritic and cubic crystals, solid salts deposited on the ice surface optically act similar to a thin snow layer. Faster grown ice has a complex structure with smaller and more disordered platelets and crystals. As the ice warms and the brine volume increases, edges become smoother, brine pockets expand, and air bubbles coalesce, all of which decrease scattering.

Future laboratory work should focus on this problem of relating the optical properties to the physical state and structure of the ice. Much of the previous work regarding the optical properties of sea ice has been primarily phenomenological. Albedos and extinction coefficients were determined and associated with various categories of ice while the radiative processes occurring in the ice were largely ignored. In this research, by combining observations of changes in the optical properties as the physical state of the ice varied with a more advanced photometric model, some qualitative insight into radiative transfer in sea ice was obtained.

Complex enough to accurately describe the physics involved, yet simple enough to avoid time consuming computing techniques, the four stream model, considering both anisotropic scattering and refraction at the boundaries, provides an effective method to examine the radiative

processes in sea ice. Present modeling efforts are severely limited by a scarcity of data concerning the scattering coefficients and the phase functions.

Most productive would be a series of experiments on small homogeneous ice samples to determine single scattering albedos and phase functions over an extensive range of conditions. Unlike the large heterogeneous ice slabs of the tank experiments, these small samples could be physically uniform, allowing a more precise statement of the relationship between the physical parameters and the single scattering albedo and phase function. The scattering properties of a given sample could be measured as a function of temperature, wavelength, and sample orientation. Measurements of different samples could indicate the effects of salinity, platelet size, growth conditions, air bubble density and size distribution, and depth within the ice. In this fashion the optical influence of specific physical parameters could be isolated. Also necessary are more accurate measurements of the spectral absorption coefficients of pure bubble free ice, particularly at short wavelengths where the absorption is very small.

Calculations, using eight and sixteen stream discrete ordinate models, are needed to investigate the angular distribution of upwelling radiance. At present, when considering refraction at the ice-air interface, the upwelling radiance is defined to be a linear function of μ . Examining a few representative cases, the accuracy of this assumption could be further tested.

This additional information would enable a more accurate and extensive photometric modeling of sea ice. Scattering results from

small homogeneous samples could be assembled using a multilayer model to optically represent a very complex ice cover. Changes in the deposition of radiant energy within an evolving ice cover could be examined. By coupling experimentally determined phase functions and single scattering albedos with four stream photometric models, an enhanced understanding of radiative transfer processes in sea ice could be obtained.

Bibliography

- Abramowitz, M., and Stegun, I. A. (eds.) 1965. *Handbook of Mathematical Functions*. Dover, New York.
- Alkezweeny, A. J., and Hobbs, P. V. 1966. The reflection spectrum of ice in the near infra-red. *Journal of Geophysical Research*, Vol. 71, No. 4, p. 1083-86.
- Aller, L. H. 1963. *Astrophysics: The Atmospheres of the Sun and Stars*. Ronald Press Company, New York.
- Anderson, D. L., and Weeks, W. F. 1958. A theoretical analysis of sea ice strength. *Transactions American Geophysical Union*, Vol. 39, No. 4, p. 632-40.
- Assur, A., and Weeks, W. F. 1964. Growth, structure, and strength of sea ice. *CRREL Research Report* 135.
- Bari, S. A., and Hallet, J. 1974. Nucleation and growth of bubbles at an ice water interface. *Journal of Glaciology*, Vol. 13, No. 69, p. 489-520.
- Barkstrom, B. R. 1972. Some effects of multiple scattering on the distribution of solar radiation in snow and ice. *Journal of Glaciology*, Vol. 11, No. 63, p. 357-68.
- Barkstrom, B. R., and Querfeld, C. A. 1975. Concerning the effect of anisotropic scattering and finite depth on the distribution of solar radiation in snow. *Journal of Glaciology*, Vol. 14, No. 70, p. 107-24.
- Bennington, K. O. 1963. Some crystal growth features of sea ice. *Journal of Glaciology*, Vol. 4, No. 36, p. 669-88.
- Beyer, W. H. 1976. *CRC Standard Mathematical Tables*. The Chemical Rubber Company, Cleveland, Ohio.
- Bohren, C. F., and Barkstrom, B. R. 1974. Theory of the optical properties of snow. *Journal of Geophysical Research*, Vol. 79, No. 30, p. 4527-35.
- Born, M., and Wolf, E. 1965. *Principals of Optics*. Pergamon Press, New York.
- Campbell, W. J. and others. 1975. Geophysical studies of floating ice by remote sensing. By W. J. Campbell, W. F. Weeks, R. O. Ramseier, and P. Gloersen. *Journal of Glaciology*, Vol. 15, No. 73, p. 305-28.
- Carslaw, H. S., and Jaeger, J. C. 1959. *Conduction of Heat in Solids*. Oxford University Press.
- Chandrasekhar, S. 1950. *Radiative Transfer*. Dover, New York.

- Chernigovskii, N. T. 1967. Radiational properties of the ice cover of the central Arctic. [In Vangengeim, G. and Laktionov, A. F. (eds.), *Hydrometeorology of the Polar Regions*. Israel Program for Scientific Translations, Inc., ISPT 1709.]
- Chernigovskii, N. T. 1971. Solar radiation and its penetration into the snow and ice cover and into the upper layers of the northern part of the Arctic Ocean. [In Dolgin, I. M., and Gavrilova, L. A. (eds.), *Meteorological Conditions in the Arctic During IQSY*, Israel Program for Scientific Translations, Inc., Trudy Vol. 274, p. 35-49.]
- Cox, G. F. N., and Weeks, W. F. 1974. Salinity variations in sea ice. *Journal of Glaciology*, Vol. 13, No. 67, p. 109-20.
- Cox, G. F. N., and Weeks, W. F. 1975. Brine drainage and initial salt entrapment in sodium chloride ice. *CRREL Research Report 345*, Hanover, NH.
- Davis, H. T., and Munis, R. H. 1973. Effect of salinity on the optical extinction of sea ice at 6328Å. *CRREL Research Report 308*, Hanover, NH.
- Dorsey, N. E. 1940. *Properties of Ordinary Water Substance*. Reinhold Publishing Corporation, New York.
- Dunkle, R. V., and Bevans, J. T. 1956. An approximate analysis of the solar reflectance and transmittance of a snow cover. *Journal of Meteorology*, Vol. 13, No. 2, p. 212-16.
- Eide, L. I., and Martin, S. 1975. The formation of brine drainage features in young sea ice. *Journal of Glaciology*, Vol. 14, No. 70, p. 137-53.
- Fleagle, R. G., and Businger, J. A. 1963. *An Introduction to Atmospheric Physics*. Academic Press, New York.
- Fletcher, J. O. 1965. The Heat Budget of the Arctic Basin and Its Relation to Climate. R-444-PR, Rand Corporation, Santa Monica, CA.
- Gaitskhoki, B. Y. 1971. A photometric model of the snow ice cover. [In Bogorodskii (ed.), *The Physics of Ice*. Israel Program for Scientific Translations, Inc., Trudy Vol. 295, p. 48-52.]
- Gast, P. R. 1960. Solar radiation. [In Campen, C. F. and others (ed.), *Handbook of Geophysics*. Macmillan, New York, p. 16:14-16:32.]
- Gavriilo, V. P., and Gaitskhoki, B. Y. 1971. The statistics of air inclusions in ice. [In Bogorodskii (ed.), *The Physics of Ice*. Israel Program for Scientific Translations, Inc., Trudy Vol. 295, p. 48-52.]
- Glen, J. W. 1974. The physics of ice. *CRREL Cold Regions Science and Engineering*. Pt. II, Sect. C2A. Hanover, NH.

- Goodrich, L. E. 1970. Review of radiation absorption coefficients for clear ice in the spectral region 0.3 to 3 microns. *National Research Council Canadian Technical Paper* 331.
- Gow, A. J., and Langston, D. 1977. Growth history of lake ice in relation to its stratigraphic, crystalline, and mechanical structure. *CRREL Research Report* 77-1, Hanover, NH.
- Gow, A. J., and Weeks, W. F. 1977. The internal structure of fast ice near Narwhal Island, Beaufort Sea, Alaska. *CRREL Research Report* 77-29, Hanover, NH.
- Grenfell, T. C., and Maykut, G. A. 1977. The optical properties of ice and snow in the Arctic Basin. *Journal of Glaciology*, Vol. No. 18, No. 80, p. 445-63.
- Griggs, M. 1968. Aircraft measurements of albedo and absorption of stratus clouds and surface albedos. *Journal of Applied Meteorology*, Vol. 7, p. 1012.
- Hanson, K. J. 1961. The albedo of sea ice and ice islands in the Arctic Ocean basin. *Arctic*, Vol. 14, No. 3, p. 188-96.
- Hobbs, P. V. 1974. *Ice Physics*. Clarendon Press, Oxford.
- Jenkins, F. A., and White, H. E. 1976. *Fundamentals of Optics*. McGraw-Hill, New York.
- Jerlov, N. G. 1976. *Marine Optics*. Elsevier Scientific Publishing Company, Amsterdam.
- Lane, J. W. 1975. Optical properties of salt ice. *Journal of Glaciology*, Vol. 15, No. 73, p. 363-72.
- Langleben, M. P. 1968. Albedo measurements of an arctic ice cover from high towers. *Journal of Glaciology*, Vol. 7, No. 50, p. 289-97.
- Langleben, M. P. 1969. Albedo and degree of puddling of a melting cover of sea ice. *Journal of Glaciology*, Vol. 8, No. 54, p. 407-12.
- Langleben, M. P. 1971. Albedo of melting sea ice in the southern Beaufort Sea. *Journal of Glaciology*, Vol. 10, No. 58, p. 101-04.
- Liou, K. N. 1973. A numerical experiment on Chandrasekhar's discrete-ordinate method for radiative transfer: Applications to cloudy and hazy atmospheres. *Journal of Atmospheric Sciences*, Vol. 30, No. 7, p. 1303-26.
- Liou, K. N. 1974. Analytic two-stream and four-stream solutions for radiative transfer. *Journal of Atmospheric Sciences*, Vol. 31, No. 5, p. 1473-75.

- Lofgren, G., and Weeks, W. F. 1969. Effect of growth parameters on substructure spacing in NaCl ice crystals. *Journal of Glaciology*, Vol. 8, No. 52, p. 153-64.
- Martin, S. 1974. Ice stalactites: Comparison of a laminar flow theory with experiment. *Journal of Fluid Mechanics*, Vol. 63, Pt. 1, p. 51-79.
- Maykut, G. A. 1977. Estimates of the regional heat and mass balance of the ice cover. *A Symposium on Sea Ice Processes and Models, Volume 1, AIDJEX Research*. Division of Marine Resources, University of Washington, p. 65-74.
- Maykut, G. A. 1978. Energy exchange over young sea ice in the Central Arctic. *Journal of Geophysical Research*, Vol. 83, No. C7, p. 3646-58.
- Maykut, G. A., and Grenfell, T. C. 1975. The spectral distribution of light beneath first-year sea ice in the Arctic Ocean. *Limnology and Oceanography*, Vol. 20, No. 4, p. 554-63.
- Maykut, G. A., and Untersteiner, N. 1969. Numerical prediction of the thermodynamic response of arctic sea ice to environmental changes. *Memorandum RM-6093-PR*, Rand Corporation, Santa Monica, CA.
- Maykut, G. A., and Untersteiner, N. 1971. Some results from a time dependent, thermodynamic model of sea ice. *Journal of Geophysical Research*, Vol. 76, No. 6, p. 1550-75.
- Neumann, G., and Pierson, W. J. 1966. *Principals of Physical Oceanography*. Prentice-Hall, New Jersey.
- Ono, N. 1967. Specific heat and heat of fusion of sea ice. [In Ōura, H., (ed.) *Physics of Snow and Ice: International Conference of Low Temperature Science....1966....Proceedings*, Vol. I, Pt. 1. (Sapporo), Institute of Low Temperature Science, Hokkaido University, p. 599-610.]
- Papoulis, A. 1965. *Probability, Random Variables, and Stochastic Processes*. McGraw-Hill, New York.
- Pounder, E. R. 1965. *The Physics of Ice*. Pergamon Press, Oxford, 151 p.
- Richtmyer, R. D. 1957. *Difference Methods for Initial Value Problems*. Interscience, New York.
- Robinson, N. 1966. *Solar Radiation*. Elsevier Publishing Company, New York.
- Roulet, R. R., and others. 1974. Spectrophotometers for the measurement of light in polar ice and snow. By R. R. Roulet, G. A. Maykut, and T. C. Grenfell. *Applied Optics*, Vol. 13, No. 7, p. 1652-58.

- Sauberer, F. 1950. Die spektrale strahlungsdurchlässigkeit des eises. *Wetter und Leben*, Jahrg. 2, Heft 9/10, p. 143-97.
- Sauberer, F., and Dirmhirn, I. 1958. Das Strahlungsklima. [In Steinhauser, F., and others (eds.), *Klimatographie von Österreich*. Hrsg. und bearbeitet von F. Steinhauser, O. Eckel, F. Lauscher. *Österreichische Akademie der Wissenschaften. Denkschriften der Gesamtakademie*, Bd. 3, I. Lief., p. 13-102.]
- Schwerdtfeger, P. 1963. The thermal properties of sea ice. *Journal of Glaciology*, Vol. 4, No. 36, p. 789-807.
- Sinha, N. K. 1977. Techniques for studying structure of sea ice. *Journal of Glaciology*, Vol. 18, No. 79, p. 315-23.
- Smith, R. C. 1973. Optical properties of the arctic upper water. *Arctic*, Vol. 26, No. 4, p. 303-13.
- Thomas, C. W. 1963. On the transfer of visible radiation through sea ice and snow. *Journal of Glaciology*, Vol. 4, No. 34, p. 481-84.
- Thorndike, A. S., and Maykut, G. A. 1973. On the thickness distribution of sea ice. *AIDJEX Bulletin* 21, p. 31-48.
- Thorndike, A. S., and others. 1975. The thickness distribution of sea ice. By A. S. Thorndike, D. A. Rothrock, G. A. Maykut, and R. Colony. *Journal of Geophysical Research*, Vol. 80, No. 33, p. 4501-13.
- Tricker, R. A. 1970. *Introduction to Meteorological Optics*. Elsevier Publishing Company, New York.
- Untersteiner, N. 1961. On the mass and heat budget of arctic sea ice. *Archiv für Meteorologie, Geophysik und Bioklimatologie*, Ser. A, Bd. 12, Heft 2, p. 151-82.
- Untersteiner, N. 1964. Calculations of temperature regime and heat budget of sea ice in the central Arctic. *Journal of Geophysical Research*, Vol. 69, No. 22, p. 4755-66.
- Untersteiner, N. 1967. Natural desalination and equilibrium salinity profile of old sea ice. [In Ōura, H. (ed.), *Physics of Snow and Ice: International Conference of Low Temperature Science....1966.. Proceedings*, Vol. I, Pt. 1. (Sapporo), Institute of Low Temperature Science, Hokkaido University, p. 569-77.]
- Weast, R. C. (ed.) 1967. *CRC Handbook of Chemistry and Physics*. The Chemical Rubber Company, Cleveland, Ohio.
- Weeks, W. F. 1962. Tensile strength of NaCl ice. *Journal of Glaciology*, Vol. 4, No. 31, p. 25-52.
- Weeks, W. F., and Assur, A. 1967. The mechanical properties of sea ice. *CRREL Research Report II-C3*. Hanover, NH.

- Weeks, W. F., and Gow, A. J. 1978. Preferred crystal orientations in the fast ice along the margins of the Arctic Ocean. *Journal of Geophysical Research*, Vol. 83, No. C10, p. 5105-22.
- Weeks, W. F., and Hamilton, W. L. 1962. Petrographic characteristics of young sea ice, Point Barrow, Alaska. *American Mineralogist*, Vol. 47, p. 945-961.
- Weeks, W. F., and Lofgren, G. 1967. The effective solute distribution coefficient during the freezing of NaCl solutions. [In Oura, H. (ed.), *Physics of Snow and Ice: International Conference of Low Temperature Science....1966....Proceedings*, Vol. I, Pt. 1. (Sapporo), Institute of Low Temperature Science, Hokkaido University, p. 579-99.]
- Weller, G. E. 1969. Radiation diffusion in antarctic ice media. *Nature*, Vol. 221, No. 5178, p. 355-56.
- Weller, G. 1972. Radiation flux investigations. *AIDJEX Bulletin* 14, p. 28-30.
- Weller, G. E., and Schwerdtfeger, P. 1967. Radiation penetration in antarctic plateau and sea ice. [In Polar Meteorology. *World Meteorological Organization Technical Note* No. 87, p. 120-41 (WMO No. 211. TP. 111.)]
- Wendler, G. 1973. Sea ice observations by means of satellite. *Journal of Geophysical Research*, Vol. 78, No. 9, p. 1427-48.
- Yentsch, C. S. 1959. The influence of phytoplankton on the colour of sea water. *Deep Sea Research*, Vol. 7, p. 1-9.

APPENDIX A
ADDITIONAL OPTICAL RESULTS

For reference additional optical results from the tank experiments are now presented. Spectral albedos and extinction coefficients from the growth and warming phases of Experiments 3-6 are shown in Figures A.1 - A.9. In each figure the curves are numbered by site. Data concerning the sites displayed in the figures are summarized in Table A.1.

The results from the warming phase of Experiment 4 are somewhat unusual (Figure A.5). When the air temperature was raised from -20°C to 0°C the albedo increased at short wavelengths (less than 600 nm) and decreased at long wavelengths. This was due to the surface conditions for Site 10. The surface, having undergone draining and flooding, was very crumbly with surface water present. The albedo was enhanced by the crumbly surface, but was depressed at longer wavelengths by the surface water.

Table A.1

Summary of Sites Displayed in Appendix A

Experiment	Site	Thickness (cm)	Time (hr)	Air Temp (°C)	Surface Temp (°C)	Bulk α Cloudy Sky
3	2	4.3	9.0	-10	-5.4	.12
	3	7.6	25.5	-10	-7.1	.21
	4	11.7	50.5	-10	-8.5	.29
	6	21.1	178.0	-10	-9.9	.37
	7	27.2	249.5	-10	-10.0	.42
	8	28.4	336.5	+1	-1.3	.33
	9*	26.7	339.5	+5	-1.3	.31
4	3	4.6	18.5	-20	-12.6	.10
	4	7.6	28.5	-20	-14.0	.21
	5	11.7	42.5	-20	-16.4	.31
	6	17.8	69.5	-20	-16.9	.40
	8	25.7	140.5	-16	-16.0	.53
	10 [#]	27.9	163.5	0	-1.0	.53
5	6	23.9	71.5	-30	-24.2	.63
	7	29.0	154.0	0	-1.5	.42
6	2	3.8	5.7	-31	-13.0	.13
	3	7.6	11.7	-32	-20.0	.31
	5	17.5	33.0	-36	-26.5	.52
	6	23.5	54.0	-36	-28.7	.86
	7	26.0	74.0	-37	-31.9	.90

* .8 cm of surface water, [#] surface very crumbly with water present

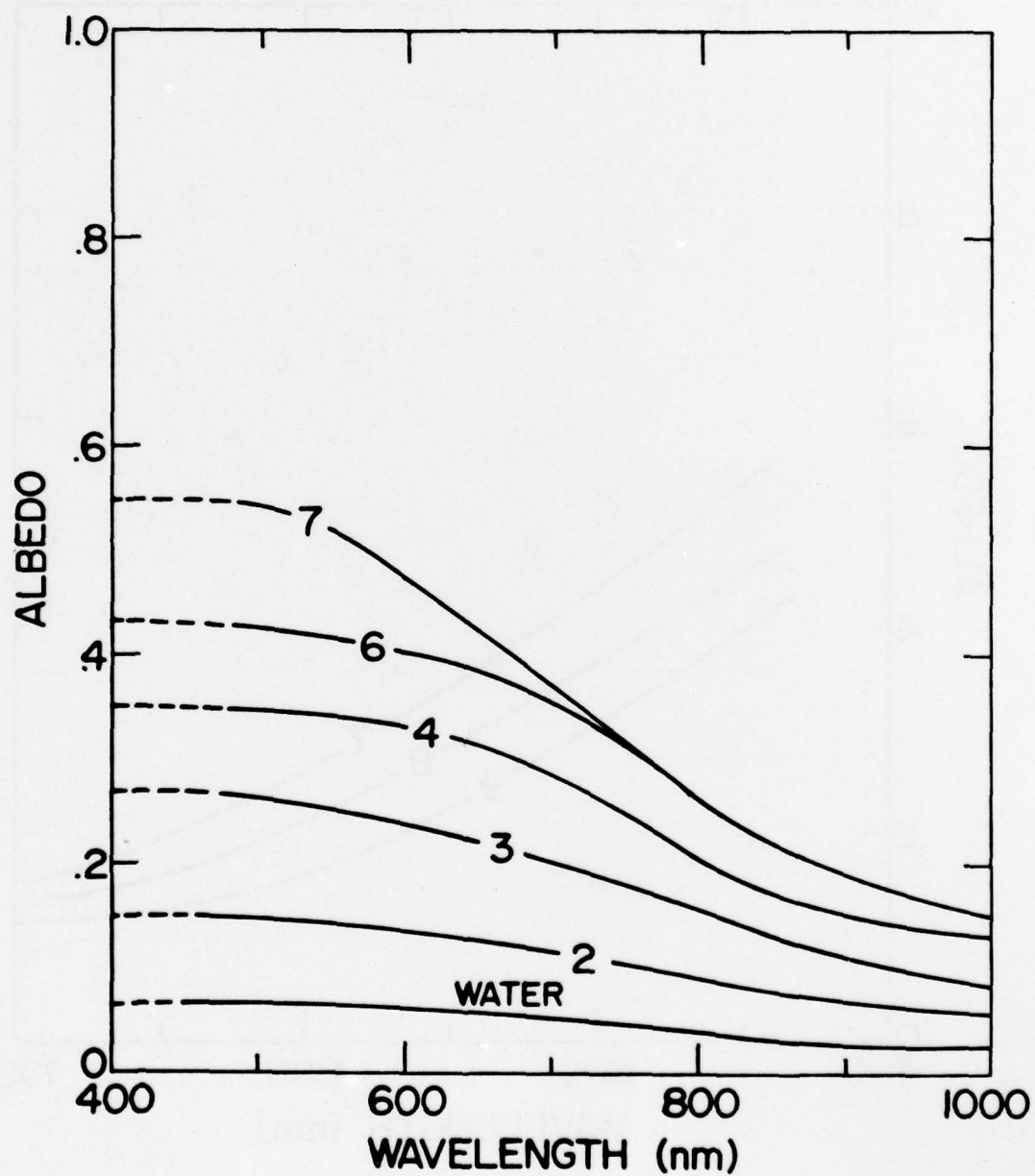


Figure A-1: Spectral albedos for growth phase of Experiment 3.

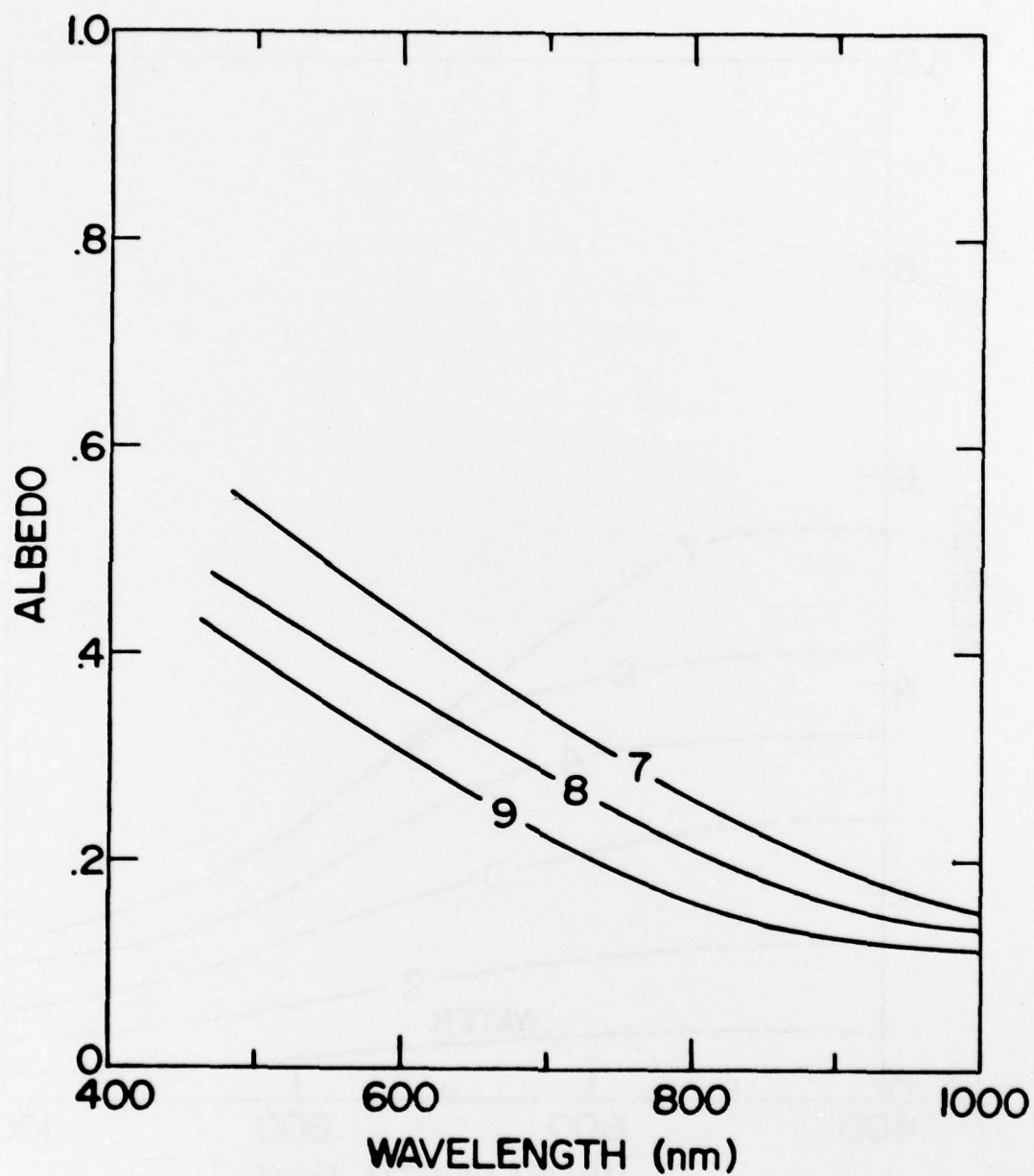


Figure A-2: Spectral albedos for warming phase of Experiment 3.

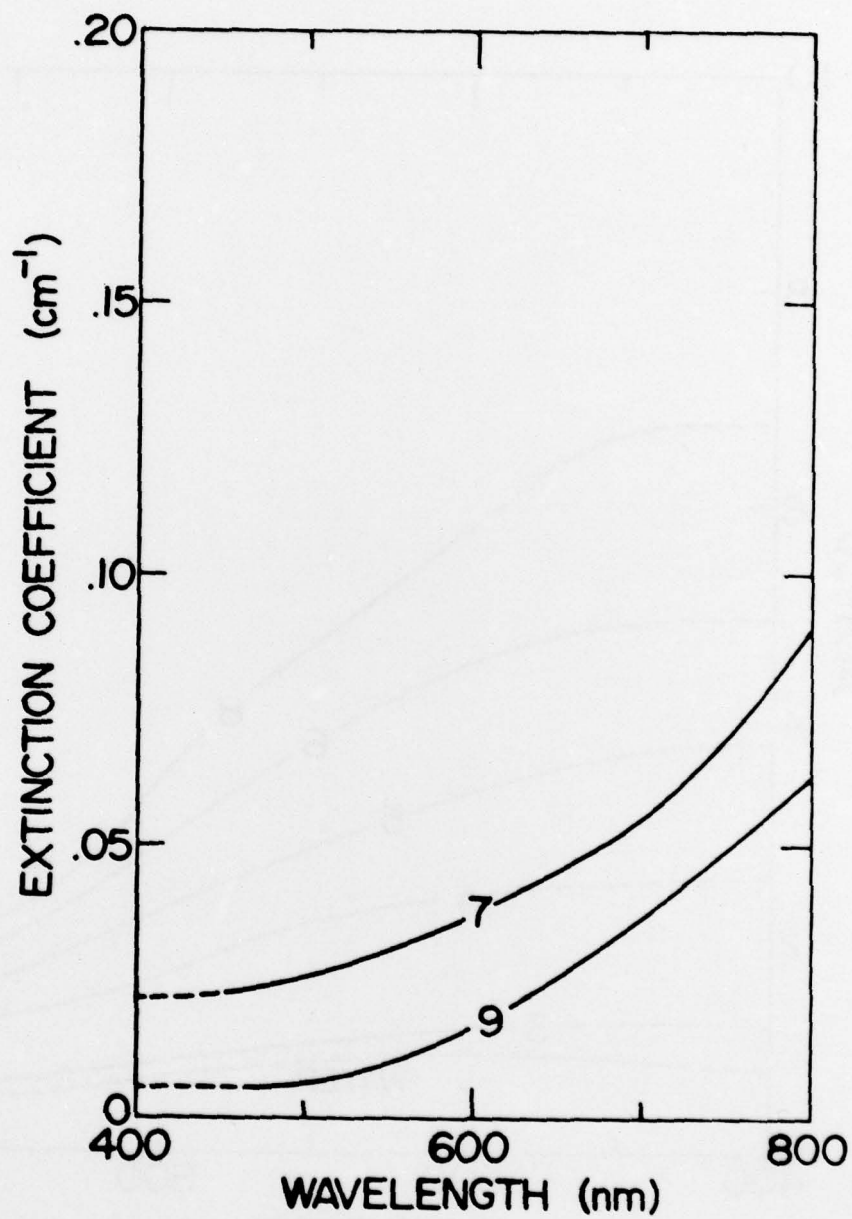


Figure A-3: Spectral extinction coefficients for warming phase of Experiment 3.

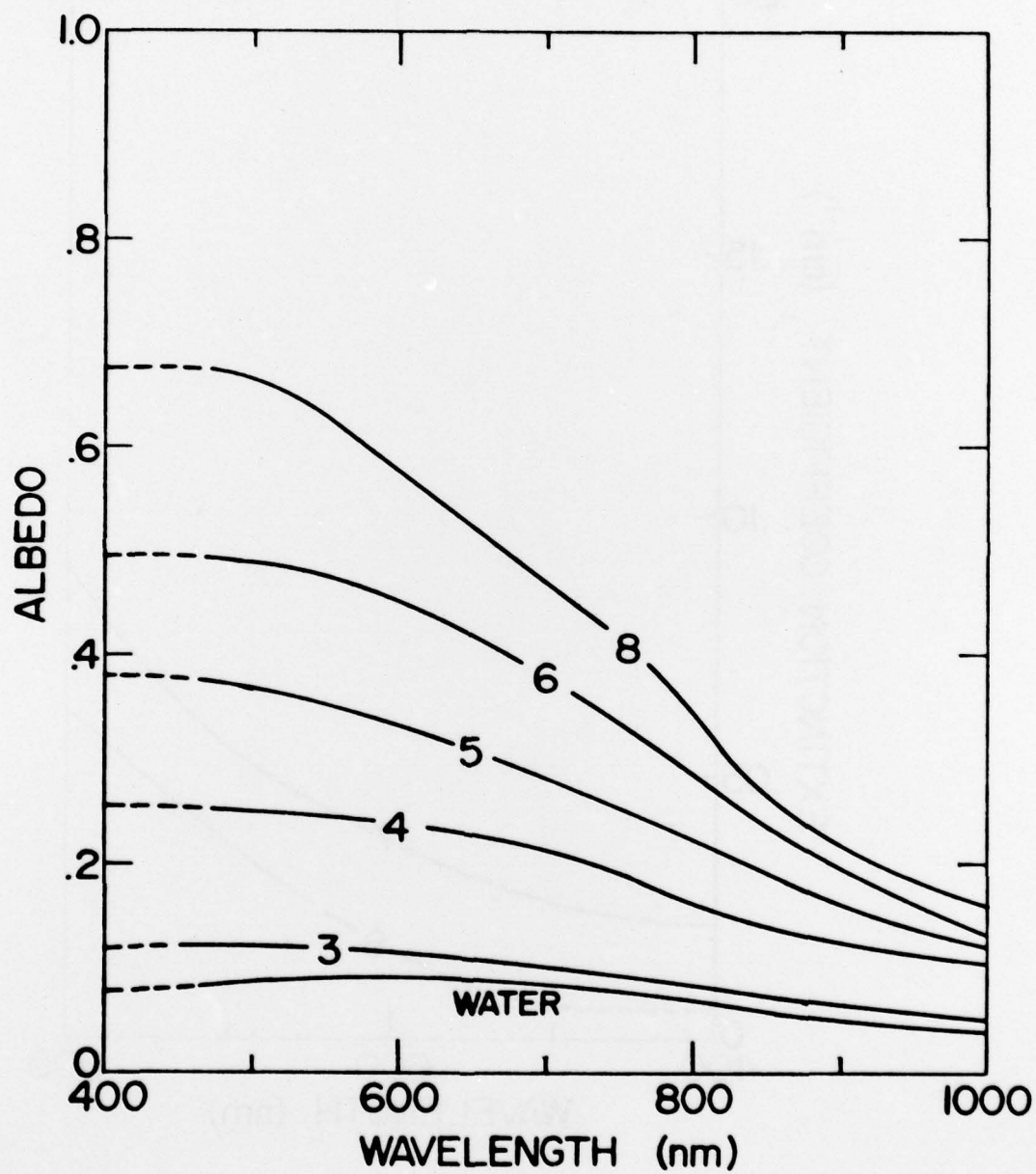


Figure A-4: Spectral albedos for growth phase of Experiment 4.

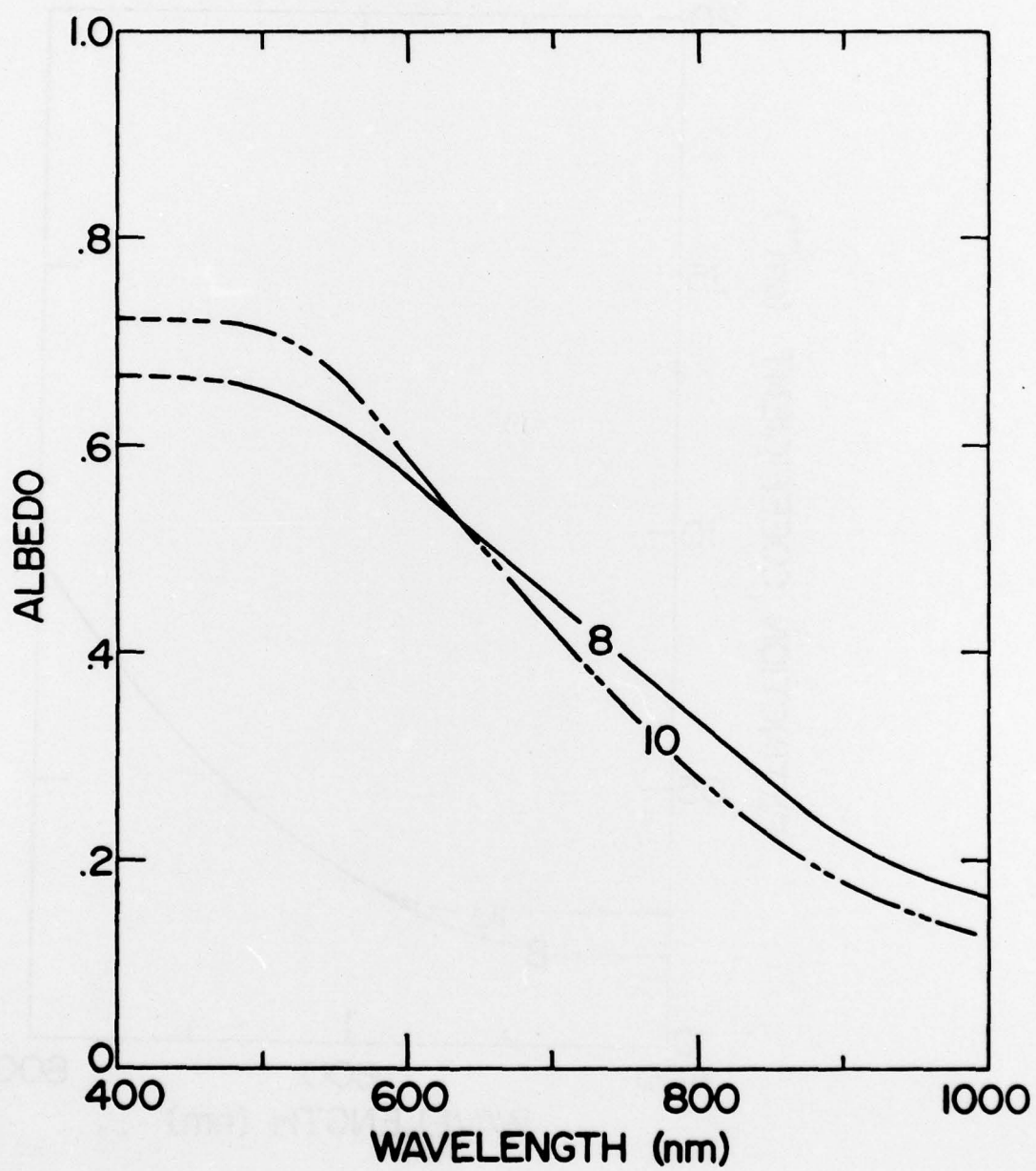


Figure A-5: Spectral albedos for warming phase of Experiment 4.

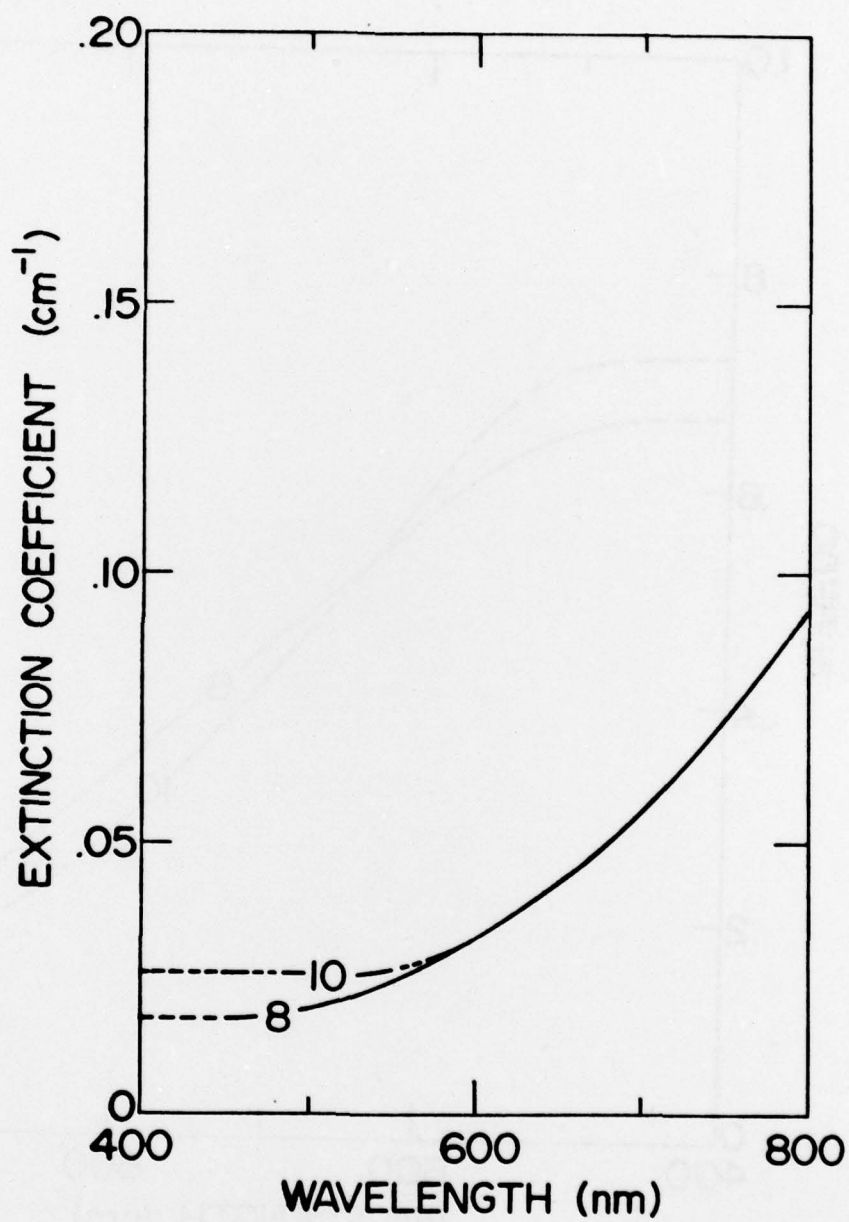


Figure A-6: Spectral extinction coefficients for warming phase of Experiment 4.

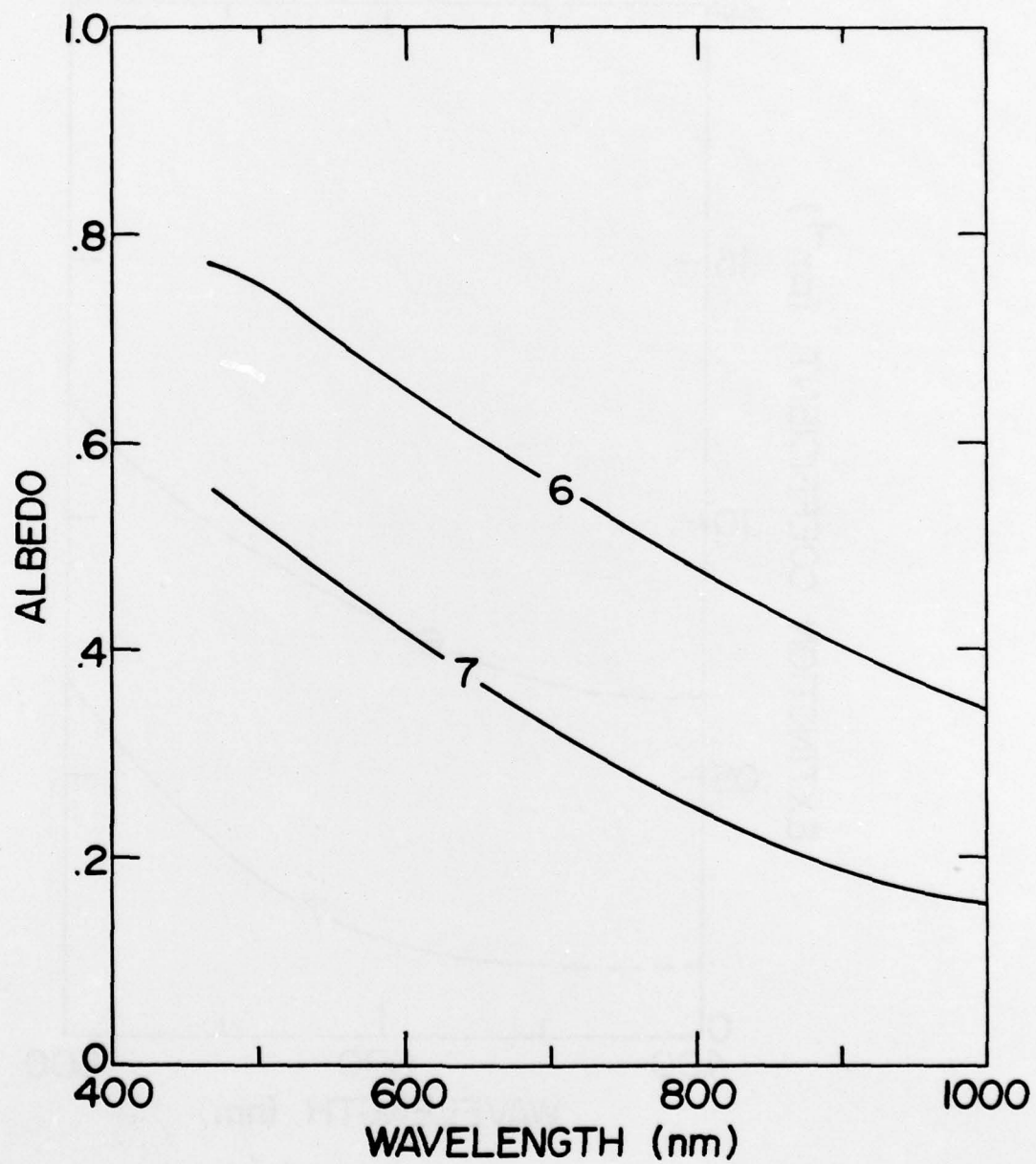


Figure A-7: Spectral albedos for warming phase of Experiment 5.

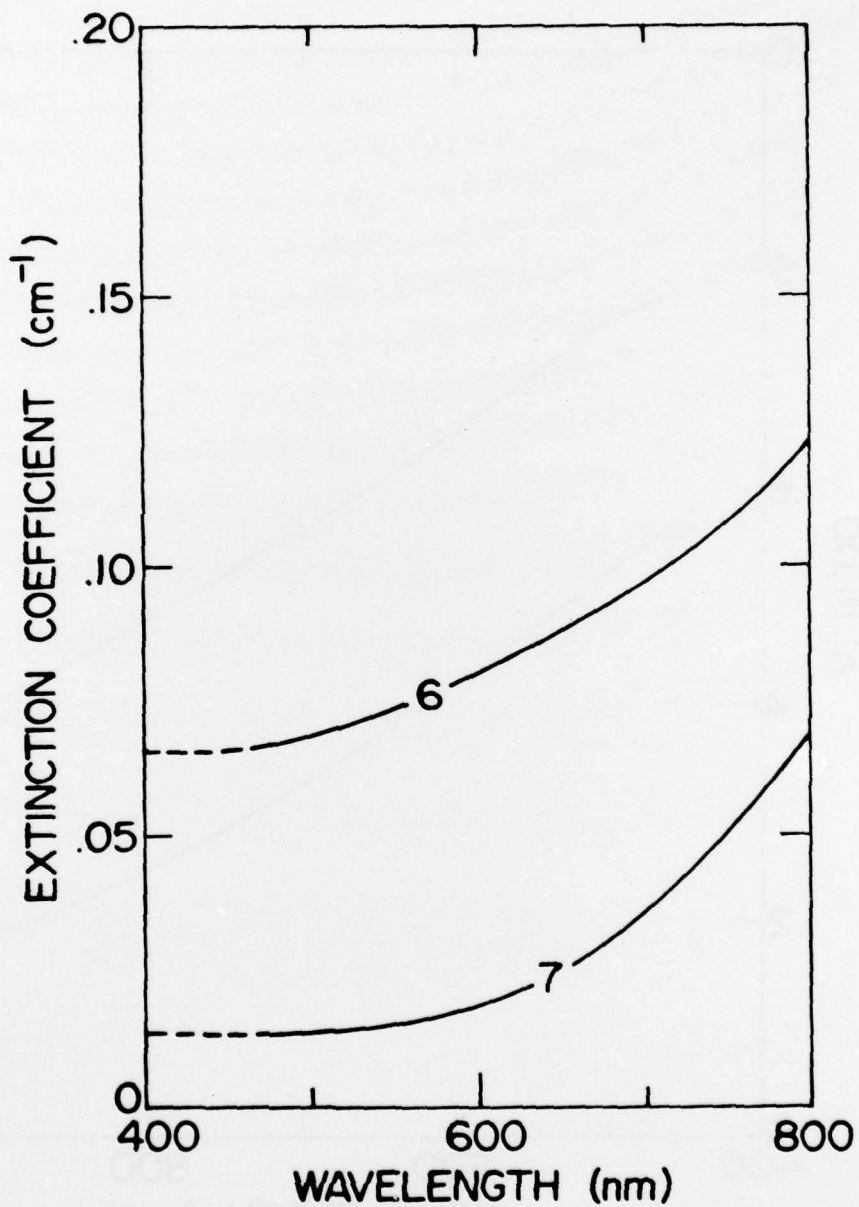


Figure A-8: Spectral extinction coefficients for warming phase of Experiment 5.

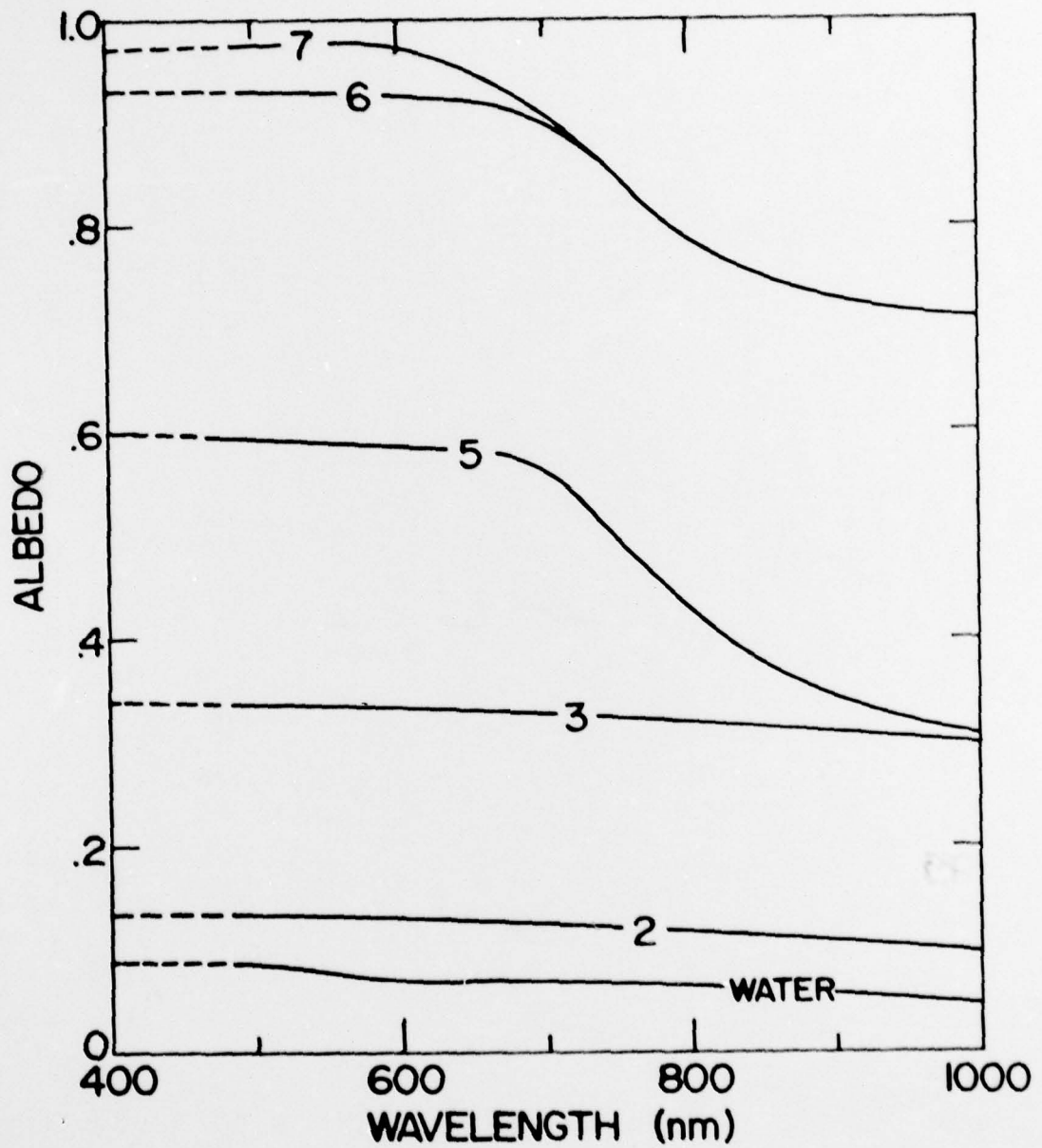


Figure A-9: Spectral albedos for growth phase of Experiment 6.

DISTRIBUTION LIST

CONTRACT N00014-76-C-0234
NR 307-252

DEFENSE DOCUMENTATION CENTER
CAMERON STATION
ALEXANDRIA, VA 22314

US NAVAL RESEARCH LABORATORY
CODE 2627
WASHINGTON, DC 20375

WOODS HOLE OCEANOGRAPHIC INST
DOCUMENT LIBRARY LO-206
WOODS HOLE, MA 02543

COLD REGIONS RES & ENG LAB
PO BOX 282
HANOVER, NH 03755

CAPT D C NUTT, USN (RET)
DEPARTMENT OF GEOGRAPHY
DARTMOUTH COLLEGE
HANOVER, NH 03755

DR JOHN C F TEDROW
DEPT OF SOILS, LIPMAN HALL
RUTGERS UNIVERSITY
NEW BRUNSWICK, NJ 08903

DR KENNETH L HUNKINS
LAMONT-DOHERTY GEOLOGICAL OBSY
TORRY CLIFFE
PALISADES, NY 10964

CHIEF OF ENGINEERS
ATTN DAEN-MCE-D
DEPARTMENT OF THE ARMY
WASHINGTON, DC 20314

DEPARTMENT OF THE ARMY
OFFICE CHIEF OF ENGINEERS
ATTN DAEN-RDM
WASHINGTON, DC 20314

MR M R HERRMAN
NAVAL FACILITIES ENG COMMAND
CODE 032 A, YARDS & DOCKS ANNEX
ROOM 2B1
WASHINGTON, DC 20390

MR ROBERT D KETCHUM JR
BLDG 70, CODE 8050
NAVAL RESEARCH LABORATORY
WASHINGTON, DC 20390

MR LOUIS DEGOES, EXEC SECTY
POLAR RESEARCH BOARD
NATL ACADEMY OF SCIENCES
2101 CONSTITUTION AVENUE, NW
WASHINGTON, DC 20418

POLAR INFORMATION SERVICE
OFFICE OF POLAR PROGRAMS
NATIONAL SCIENCE FOUNDATION
WASHINGTON, DC 20550

DR GEORGE A LLANO
ACTING CHIEF SCIENTIST
OFFICE OF POLAR PROGRAMS
NATIONAL SCIENCE FOUNDATION
WASHINGTON, DC 20550

MR M M KLEINERMAN
PROJECT MANAGER FOR ARCTIC ASW
US NAVAL ORDNANCE LABORATORY
WHITE OAK, MD 20910

MR PAUL P LAUVER, PUBLICATIONS
ARCTIC INST OF NORTH AMERICA
3426 NO WASHINGTON BLVD
ARLINGTON, VA 22201

DR G LEONARD JOHNSON
CODE 461, ARCTIC PROGRAMS
OFFICE OF NAVAL RESEARCH
ARLINGTON, VA 22217

DR NORBERT UNTERSTEINER
SCI ADV FOR ARCTIC & POLAR AFFAIRS
OFFICE OF NAVAL RESEARCH
CODE 400P
ARLINGTON, VA 22217

CHIEF OF NAVAL RESEARCH
OFFICE OF NAVAL RESEARCH
CODE 412
ARLINGTON, VA 22217

CHIEF OF NAVAL RESEARCH
OFFICE OF NAVAL RESEARCH
CODE 414
ARLINGTON, VA 22217

CHIEF OF NAVAL RESEARCH
OFFICE OF NAVAL RESEARCH
CODE 480D
ARLINGTON, VA 22217

DISTRIBUTION LIST, CONTRACT N00014-76-C-0234, NR 307-252, Page 2

US NAVAL OCEANOGRAPHIC OFFICE
LIBRARY (CODE 8160)
NSTL STATION
BAY ST LOUIS, MS 39522

DIRECTOR, INST OF POLAR STUDIES
OHIO STATE UNIVERSITY
125 SOUTH OVAL DRIVE
COLUMBUS, OH 43210

DR ALBERT H JACKMAN
CHAIRMAN, DEPT OF GEOGRAPHY
WESTERN MICHIGAN UNIVERSITY
KALAMAZOO, MI 49001

DR REID A BRYSON
INST FOR ENVIRONMENTAL STUDIES
UNIVERSITY OF WISCONSIN
MADISON, WI 53706

DR DAVID CLARK
DEPARTMENT OF GEOLOGY
UNIVERSITY OF WISCONSIN
MADISON, WI 53706

PROF RICHARD S TANKIN
DEPT OF MECH ENGINEERING
NORTHWESTERN UNIVERSITY
EVANSTON, IL 60201

PROF WILLIAM MCINTIRE
COASTAL STUDIES INSTITUTE
LOUISIANA STATE UNIVERSITY
BATON ROUGE, LA 70803

DR HARLEY J WALKER
DEPARTMENT OF GEOGRAPHY
LOUISIANA STATE UNIVERSITY
BATON ROUGE, LA 70803

DR V P HESSLER
4230 EUTAW STREET
BOULDER, CO 80302

WORLD DATA CENTER: A FOR GLAC
INST OF ARCTIC & ALPINE RESEARCH
UNIVERSITY OF COLORADO
BOULDER, CO 80309

CONTRACT ADMINISTRATOR
OFFICE OF NAVAL RESEARCH BRANCH OFC
1030 EAST GREEN STREET
PASADENA, CA 91106

COMMANDER
NAVAL UNDERSEA CENTER
ATTN TECHNICAL LIBRARY, CODE 1311
SAN DIEGO, CA 92132

RESEARCH LIBRARY
NAVAL ELECTRONICS LAB CENTRE
SAN DIEGO, CA 92152

LIBRARIAN
TECHNICAL LIBRARY DIVISION
NAVAL CIVIL ENGINEERING LABORATORY
PORT HUENEME, CA 93041

COMMANDING OFFICER
CODE L61
NAVAL CIVIL ENGINEERING LABORATORY
PORT HUENEME, CA 93043

MR BEAUMONT BUCK
POLAR RESEARCH LABORATORY ING
123 SANTA BARBARA STREET
SANTA BARBARA, CA 93101

SUPERINTENDENT
NAVAL POSTGRADUATE SCHOOL
LIBRARY CODE 2124
MONTEREY, CA 93940

DR ARTHUR LACHENBRUCH
BRANCH OF GEOPHYSICS
US GEOLOGICAL SURVEY
345 MIDDLEFIELD ROAD
MENLO PARK, CA 94025

DR W M SACKINGER
DEPT OF ELECTRICAL ENGINEERING
UNIVERSITY OF ALASKA
FAIRBANKS, AK 99701

DR KEITH MATHER
705 GRUENING BUILDING
UNIVERSITY OF ALASKA
FAIRBANKS, AK 99701

DR CHARLES E BEHLKE, DIRECTOR
INST OF ARCTIC ENVIRONMENTAL ENG
UNIVERSITY OF ALASKA
COLLEGE, AK 99701

DR DONALD W HOOD
INST FOR MARINE SCIENCE
UNIVERSITY OF ALASKA
FAIRBANKS, AK 99701

DISTRIBUTION LIST, CONTRACT N00014-76-C-0234, NR 307-252, Page 3

DR GUNTER WELLER
GEOPHYSICAL INSTITUTE
UNIVERSITY OF ALASKA
COLLEGE, AK 99701

DEFENCE RESEARCH BOARD
DEPT OF NATIONAL DEFENCE
190 O'CONNOR STREET
OTTAWA, ONTARIO, CANADA K1A 0Z3

MISS MOIRA DUNBAR
DEFENCE RESEARCH ESTABLISHMENT
OTTAWA, NATL DEFENCE HEADQUARTERS
OTTAWA, ONTARIO, CANADA K1A 0Z4

DR ROBERT L RAUSCH
DEPT OF MICROBIOLOGY
W COLLEGE OF VET MEDICINE
UNIVERSITY OF SASKATCHEWAN
SASKATOON, SASK, CANADA S7N 0W0

DR E L LEWIS
FROZEN SEA RESEARCH GROUP
INSTITUTE OF OCEAN SCIENCES
9860 W SAANICH ROAD
SIDNEY, BC, CANADA V8L 3S2

DR A R MILNE
DEFENCE RES ESTABLISHMENT PAC
FLEET MAIL OFFICE
VICTORIA, BC, CANADA

METEOROLOGICAL OFFICE LIBRARY
LONDON ROAD
BRACKNELL, BERKSHIRE, ENGLAND

DR T E ARMSTRONG
SCOTT POLAR RESEARCH INSTITUTE
CAMBRIDGE, CB2 1ER, ENGLAND

THE LIBRARIAN
SCOTT POLAR RESEARCH INSTITUTE
CAMBRIDGE CB2 1ER, ENGLAND

DR MICHAEL KELLY
SCHOOL OF ENVIRONMENTAL SCIENCES
UNIVERSITY OF EAST ANGLIA
NORWICH NR4 7TJ, ENGLAND

NATIONAL INST OF OCEANOGRAPHY
WORMLEY, GODALMING
SURREY, ENGLAND

CENTRE NATL DE LA RECHERCHE SCI
LABORATOIRE DE GLACIOLOGIE
UNIVERSITE DE GRENOBLE 1
SERV DE GEOPHYS, 2, RUE TRES
CLOITRES 38-GRENOBLE, FRANCE

LIBRARIAN
NAVAL ARCTIC RESEARCH LABORATORY
BARROW, AK 99723

MGR INUVIK RESEARCH LABORATORY
BOX 1430
INUVIK, NORTHWEST TERRITORIES
XOE OTO CANADA

DR SVENN ORVIG
MCGILL UNIVERSITY
DEPT OF METEOROLOGY
PO BOX 6070
MONTREAL 101, PQ, CANADA

MARINE SCIENCE CENTRE LIBRARY
MCGILL UNIVERSITY
PO BOX 6070
MONTREAL 101, PQ, CANADA

DR E R POUNDER
RUTHERFORD PHYSICS BUILDING
MCGILL UNIVERSITY
3600 UNIVERSITY STREET
MONTREAL, PQ, CANADA H3A 2T8

MRS GAIL HORWOOD
METEOROLOGY LIBRARY
MCGILL UNIVERSITY
MONTREAL 101, PQ, CANADA

DR WESTON BLAKE JR
GEOLOGICAL SURVEY OF CANADA
DEPT OF ENERGY MINES RESOURCES
601 BOOTH STREET
OTTAWA, ONTARIO, CANADA K1A 0E8

DEPARTMENTAL LIBRARY-SERIALS
DEPT OF THE ENVIRONMENT
OTTAWA, ONTARIO, CANADA K1A 0H3

DISTRIBUTION LIST, CONTRACT N00014-76-C-0234, NR 307-252, Page 4

CENTRE D'ETUDES ARCTIQUES
ECOLE PARTIQUE DES HAUTES ETUDES
VI SECTION (SORBONNE)
6, RUE DE TOURNON, PARIS -6
FRANCE

DR KOU KUSUNOKI
POLAR RESEARCH CENTER
NATIONAL SCIENCE MUSEUM
KAGA 1-9-10, ITABASHI-KU
TOKYO, JAPAN

NORSK POLARINSTITUTT
ROLFSTANGVN 12, POSTBOKS 158
1330 OSLO LUFTHAVN
NORWAY

PROF DR ALEXSANDER KOSIBA
KATEFRA I OBSERWATORIUM
METEOROLOGI I KLIMATOLOGII
UNIWERSYTETN WROCLAWSKIEGO
WROCLAW 9, U CMENTARNA 8
POLAND

STOCKHOLMS UNIVERSITET
NATURGEOGRAFISKA INSTITUTIONEN
BOX 6801
113 86 STOCKHOLM, SWEDEN

DR ING O MAGGIOLO
FACULTAD DE INGENIERIA
HERRERA Y REISSIG 585
MONTEVIDEO, URUGUAY

LIBRARY-CENTRE FOR NORTHERN
STUDIES AND RESEARCH
MCGILL UNIVERSITY
1020 PINE AVENUE WEST
MONTREAL, PQ, CANADA H3A 1A2

UNIVERSITY ARCHIVES
UNIVERSITY RECORDS SECTION
CAMPUS BL-10

RESIDENT REPRESENTATIVE
OFFICE OF NAVAL RESFARCH
Room 422, UNIV DISTRICT BLDG.
CAMPUS JD-27

DR LAWRENCE COACHMAN
OCEANOGRAPHY
WB-10

DR KNUT AAGARD
OCEANOGRAPHY
WB-10

DR T SAUNDERS ENGLISH
OCEANOGRAPHY
WB-10

SECURITY CLASSIFICATION OF THIS PAGE (When Data Entered)

REPORT DOCUMENTATION PAGE		READ INSTRUCTIONS BEFORE COMPLETING FORM
1. REPORT NUMBER SCIENTIFIC REPORT NO. 17	2. GOVT ACCESSION NO.	3. RECIPIENT'S CATALOG NUMBER
4. TITLE (and Subtitle) THE OPTICAL PROPERTIES OF YOUNG SEA ICE		5. TYPE OF REPORT & PERIOD COVERED SCIENTIFIC REPORT NO. 17
		6. PERFORMING ORG. REPORT NUMBER
7. AUTHOR(s) Donald A. Perovich		8. CONTRACT OR GRANT NUMBER(s) NO0014-76-C-0234
9. PERFORMING ORGANIZATION NAME AND ADDRESS Arctic Sea Air Interaction Department of Atmospheric Sciences AK-40 University of Washington, Seattle, WA 98195		10. PROGRAM ELEMENT, PROJECT, TASK AREA & WORK UNIT NUMBERS NR 307-252
11. CONTROLLING OFFICE NAME AND ADDRESS Office of Naval Research Code 461, Arctic Program Arlington, VA 22217		12. REPORT DATE Aug 1979
		13. NUMBER OF PAGES 170
14. MONITORING AGENCY NAME & ADDRESS (if different from Controlling Office)		15. SECURITY CLASS. (of this report) UNCLASSIFIED
		15a. DECLASSIFICATION/DOWNGRADING SCHEDULE
16. DISTRIBUTION STATEMENT (of this Report) THE DISTRIBUTION OF THIS REPORT IS UNLIMITED		
17. DISTRIBUTION STATEMENT (of the abstract entered in Block 20, if different from Report) SCIENTIFIC-17		
18. SUPPLEMENTARY NOTES		
19. KEY WORDS (Continue on reverse side if necessary and identify by block number) YOUNG SEA ICE OPTICAL PROPERTIES RADIATIVE TRANSFER Albedo Extinction coefficient		
20. ABSTRACT (Continue on reverse side if necessary and identify by block number) Eight laboratory experiments were performed to determine the optical properties of young salt ice and to examine correlations between the optical properties and the state of the ice. Ice grown at different temperatures (-10, -20, -30, and -37°C) and from water of different salinities (0, 16, and 31 ‰) was investigated. The experiments were conducted using a tank system which was designed to grow ice similar to that found in nature, allow an accurate determination of the state and structure of the ice, and permit <u>in situ</u> optical		

DD FORM 1 JAN 73 1473

EDITION OF 1 NOV 68 IS OBSOLETE
S/N 0102-014-6601

370 270
SECURITY CLASSIFICATION OF THIS PAGE (When Data Entered)

20. Abstract (cont.)

CONT → measurements to be made. Measurements of incident, reflected, and transmitted irradiances were used in conjunction with a modified Dunkle and Bevens photometric model to determine spectral albedos and extinction coefficients. The thin cold ice of these experiments had albedos which were comparable to the values for the thicker warmer ice examined by previous researchers; however, extinction coefficients were 1.5 to 15 times greater. Qualitative relationships between the optical properties and the physical state of the ice were observed. As the ice temperature decreased (and the brine volume increased) both albedo and extinction coefficient increased; when the ice temperature dropped below the eutectic point the increase was drastic. The dependence of albedo and extinction coefficient on the brine content of the ice was found to be complex with both the brine volume and its vertical distribution being significant. Variations in ice salinity over the range 4 ‰ to 14 ‰ did not influence the optical properties. Increases in albedo and extinction coefficient were primarily a result of changes in the ice structure which enhanced scattering.

→ A four stream discrete ordinates photometric model was developed to treat the case of a floating ice slab. The model included both anisotropic scattering and refraction at the boundaries. The effects on albedo and transmittance of variations in such model parameters as the single scattering albedo and the phase function were investigated. Using one and two layer models, theoretical albedos and transmittances were compared to experimental values. The four stream model was further applied to investigate such topics as the depth dependence of irradiance, cases of direct beam incident radiation, the spectral dependence of albedo and transmittance, and the effects of surface layers. It was suggested that future laboratory research be oriented towards determination of single scattering albedos and phase functions for an extensive range of ice types.